ABSTRACT

GOSALIA, KEYOOR. Novel Compact Antennas for Biomedical Implants and Wireless Applications. (Under the direction of Dr. Gianluca Lazzi.)

Novel design methodologies and implementation techniques for antennas with an extremely small form factor ($kr \ll 1$; k is the wavenumber and r is the radius of enclosing spherical volume) are presented. These size reduction techniques are applied to design antennas for two emerging fields: Short (or long) range wireless connectivity and human body implants (prosthetic devices). The first test bed describes compact microstrip patch antennas employing polarization diversity for optimizing the available channel bandwidth in conventional wireless communications. Extremely small antennas (for implantation in an eye ball) operating at microwave frequencies for a visual prosthesis are designed and implemented for the second test bed.

The visual prosthesis under consideration is an implantable prosthetic device which attempts to restore partial vision in the blind (patients suffering from retinal degeneration) by artificial stimulation of the retinal cells. Mutually exclusive power and data transfer via a wireless link with the implanted device is proposed where inductive coil coupling transfers power at low frequencies while data communication is performed using extraocular and intraocular antennas at microwave frequencies. The microwave data telemetry link is characterized computationally (using Finite Difference Time Domain-FDTD) and experimentally with appropriately sized external and implanted antennas. It is observed that the head and eye tissues act as a form of dielectric lens and improve the coupling performance between the two antennas (with intraocular antenna embedded in the eye ball) as compared to coupling in free space. The data telemetry link is characterized with novel small microstrip patch and planar wire dipole as intraocular antennas.

An electromagnetic and thermal analysis of the operation of such a visual prosthesis is performed. Electromagnetic power deposition in the head is evaluated in terms of Specific Absorption Rate (SAR). Temperature rise in the tissues is characterized by computationally discretizing and implementing the bio-heat equation in three dimensions in an anatomically accurate head model.

Novel Compact Antennas for Biomedical Implants and Wireless Applications

by

Keyoor Gosalia

A dissertation submitted to the Graduate Faculty of
North Carolina State University
in partial fulfillment of the
requirements for the Degree of
Doctor of Philosophy

Electrical Engineering

Raleigh, NC

2004

Approved By:

Dr. Robert J. Trew	Dr. Zhilin Li
Dr. Gianluca Lazzi Chair of Advisory Committee	Dr. Brian Hughes

Biography

Keyoor Chetan Gosalia grew up in the small university town of Vallabh Vidyanagar, Gujarat, India. He received his B.E. degree in Electronics from Sardar Patel University, Gujarat, India in August 1999. He joined North Carolina State University (NCSU) in 2000 and received his M.S. degree in Electrical engineering in 2001. Since 2001, he has been pursuing his doctoral degree as a research assistant working under Dr. Gianluca Lazzi in the Electrical engineering department at NCSU.

His research interests include novel extremely compact and UWB microstrip patch and wire antennas for biomedical implants and wireless communications. Besides, he has worked on numerical electromagnetics, EM field–human body interaction and evaluating thermal elevation in the human body.

Acknowledgements

This dissertation is the culmination of a unique effort at teamwork over the last few years. Several forces and individuals have generously supported and contributed towards my endeavor.

I am very grateful to my advisor Dr. Gianluca Lazzi who has relentlessly encouraged and helped to refine my engineering research skills. His amazing grasp of the intricacies involved in high level research combined with his very amiable nature has been inspiring and immensely helpful. He has been my friend, my guide and my mentor—he has been my true "guru". I am indebted to him for allowing me to be a part of his research group.

To my committee members, I thank Dr. Brian Hughes for always being very accommodating and understanding. I extend my sincere gratitude to Dr. Robert Trew, for being on my committee despite his extremely busy schedule. I profusely thank Dr. Zhilin Li for his ever ready helpful nature and for those many interesting discussions on numerical partial differential equations.

To my colleagues and friends at EGRC, I am thankful for making all these years most enjoyable and unforgettable. I am grateful to Arvind Venugopal and Dr. Mete Ozkar for teaching me all the nifty ways in antenna modelling and Dr. Stephen C. DeMarco for his guidance on thermal modelling. To Stefan Schmidt, who has been supportive in many ways and for his help in numerical electromagnetics. To Anand Konanur, for his unflinching willingness to help whether it is dirty lab work or rigorous math: I will always value our research adventures and close friendship. To Patrick Brown, who diligently developed and assisted me with the human body model. I thank Shruthi Soora and Kevin Taff for their assistance in simulations and Jayesh Nath for never hesitating to help out with the lab equipment. I am appreciative of Dr. Rizwan Bashirullah, Dr. Wael Fathelbab and Steve Lipa for their helpful suggestions. And I will always cherish those discussions and light times with Ajith Kamath, Pallav Sudarshan, Ajit Rajagopalan, Abheek Gupta and Carlos Cela: thanks a lot guys. I have learnt so much from you.

I extend my gratitude to Linda Simerson, Michele Joyner and Michele Healey for

their admirable patience while helping me with all the necessary paperwork.

And, lastly I am eternally grateful to my entire family for their unconditional love and understanding while putting up with my aloof and uncommunicative nature over these years. Especially, to my mother, who inspired me, as a little boy, towards this wonderful world of science and who has been my teacher all my life. And to my father, who has inspired me to strive for excellence and taught me that no matter how complex a problem seems, it always has a practical solution.

Thank you everyone. This dissertation is dedicated to all of you.

This work has been supported in part by the Whitaker Foundation under grant No. RG-00-0298, in part by the NSF Career award No. ECS-0091599, in part by NSF under grant No. EEC-0310723 and in part under NSF award No. ECS-0335537.

Contents

List of Figures

List of Tables

Chapter 1

Introduction

1.1 Motivation

Antennas enable a seamless transition of electromagnetic energy from the guiding device (or cables) to the environment in their transmitting mode. Thus, antennas or radiating structures form the final interface to the communications channel in any wireless system (vice versa in the receiving mode). Proper antenna design methodology and system implementation is critical to ensure the successful operation of any wireless communications system. Focus on antenna design has evolved from relatively simplistic vertical wire structures over a hundred years ago, to the current research on complex 3-dimensional reconfigurable designs (incorporating other passive and active circuit elements) which satisfy system requirements of versatility in frequency of operation, polarization capability, gain and bandwidth while being aesthetically appealing and unobtrusive.

The recent proliferation of mobile and portable electronic devices has made antenna configuration an integral part of design considerations for the entire wireless system. Over the last decade, advances in wireless connectivity have led to power-

ful, low-cost, and flexible wireless system solutions. Mobile devices can now support increasingly sophisticated interactive functionality due to the continued expansion of wireless technologies. Moreover, geared by the development of compact, low power System-in-a-Package (SiPs or SoCs) by the semiconductor industry, leading mobile original equipment manufacturers (OEMs) are striving for small form factor solutions which retain their wide range in wireless functionality. This shift in the design focus of antennas (towards compactness) has led to the development of extremely small radiating configurations that find application not only in conventional long distance wireless communications but also in integrated short range mobile devices (employing Wi-Fi, Zigbee, bluetooth or Near Field Coupling (NFC) wireless applications) and even emerging technologies in biomedical engineering.

In this work, we have focused on exploring and applying novel design methodologies and implementation techniques for antennas with an extremely small form factor(much smaller than the radiansphere $kr \ll 1$). We have applied these techniques in two emerging fields. These two testbeds are short (or long) range wireless connectivity (network nodes in a Wireless Area Network (WAN)) and human body implantable antennas. Small form factor antennas are very suitable for both these applications because of their inherent portable utility.

The first test bed involves wireless connections for mobile devices which are fairly common. They require various scientific means to enhance data communication for increasing their functionality. That is, improvement in channel capacity is of utmost importance for optimum performance of these wireless network nodes. Our work towards this test bed proposes the design of novel compact antennas that employ polarization diversity to make an efficient use of available bandwidth and hence enhance channel capacity.

A completely new and as yet unexplored field of antenna design involves design

methodologies for radiating structures at microwave frequencies (0.3–30 GHz) which can be implanted inside the human body (bio-implantable antennas). Very little work has been reported so far in this arena and it is generally observed that antenna designs which retain their performance characteristics when embedded in the human tissues (which have a very strong inductive influence) are extremely difficult to design and implement. In our work, we have investigated novel compact antenna designs for implanting in the eye. This antenna is part of a potential intraocular unit in a dual unit visual prosthetic device. A significant amount of work relating to the operation of a visual prosthesis and the interaction of electromagnetic fields with the human head has been realized towards this dissertation. Hence, it is imperative that a comprehensive summary of previous work and current progress towards the realization of a visual prosthetic device be outlined as an introduction to this test bed. The following several sections describe the background and motivation behind a visual prosthesis, the currently existing techniques for implementing such a device, potential long term drawbacks of such methods and finally our proposed novel approach to perform wireless data communication in a dual unit prosthesis with implanted antennas.

1.2 Visual Prostheses

Advances in integrated circuit technology and microsurgery techniques have made it possible for researchers to successfully address the challenges involved in employing engineering techniques to aid, enhance and even augment impaired psychophysiological functions of the human body. Over the years, bio-engineering and collaborative research efforts between engineers and medical doctors have yielded numerous successful organ transplants and demonstrated the feasibility of electronic

implants in replacing the physiological functionality of receptive body organs. The receptive sense organs of the body (eye, nose, ear et.al) send information to the brain in the form of electrical impulses via the body's neuronal circuitry. This fundamental fact has motivated several research efforts to determine whether artificial electrical stimulation can assist in restoring lost bodily functions [1]. From these research efforts have emerged electronic implantable prostheses for functional neuromuscular stimulation [2], voluntary control of internal organs [3] and sensory organs such as cochlear prosthesis [4, 5]. The performance benefits of these devices have encouraged researchers to investigate whether artificial electrical stimulation can help to restore partial vision in the visually impaired.

It is well understood that vision involves extremely complex information processing in the eye which is facilitated by the neuroprocessor at the back of the eyeball called the retina which covers 65% of the curved surface area. Light from the external objects is focused by the lens and an inverted image is formed on the approximately 130 million photoreceptor cells of the retina [6]. These photoreceptor cells (differentiated into rods and cones) convert the incident photonic energy into complex electrical and chemical signals. These signals are conveyed through a network of interfacing layers (horizontal, bipolar and amacrine cell layers) and eventually reach the ganglion cell layer. The axons of ganglion cell layer form the optic nerve which transmits the information to the primary visual cortex in the brain.

In retinal degenerative diseases, Retinitis Pigmentosa (RP) and Age-related macular degeneration (AMD) are incurable and cause a profound vision loss due to degeneration of the light sensing photoreceptor cells. These diseases are among the leading causes of blindness affecting more than 10 million people worldwide [7]. It is estimated that the incidence of RP is 1 in every 4000 in the U.S. and 10% of the people over the age of 52 and 33% over the age of 75 years are afflicted with AMD [8].

Loss of photoreceptors in RP leads to a gradual loss of peripheral vision eventually inducing blindness while AMD is caused by retinal atrophy due to undernourishment.

It has been observed that in end-stage RP and AMD patients, though the photoreceptors are almost completely absent, the cell layers interfacing with photoreceptors (horizontal, bipolar, amacrine and ganglion layers) may retain their functionality and survive at higher rates [9, 10]. The physiological location of the healthy ganglion cells facilitates their artificial electrical stimulation directly via an electronic implant.

Clinical trials of electrical stimulation of retinal ganglion cells in human patients has reported to have elicited simple forms of visual perception [11, 12]. The patients were able to distinguish simple shapes and forms (including edges and patterns and sometimes even distinguish letters) when receiving stimulation from a 5×5 electrode array on the inner retinal surface. These results are still very far from true real world object recognition but they do demonstrate the feasibility of generating light patterns using electrode arrays on the retinal surface.

1.2.1 Approaches Being Considered for A Visual Prosthesis

There are several means of eliciting visual perception by electrical stimulation along the human visual pathway in blind patients. Electrical stimulation can be provided by implanted devices and based upon their location they are classified into different categories. Currently, research groups are investigating the placement of implants on the retinal surface, on the optic nerve and at the visual cortex in the brain. Each approach is briefly summarized below.

1.2.1.1 Retinal Implants

There are two kinds of retinal implants under consideration:

1) The Sub-retinal Implant: Several groups are pursuing the sub-retinal ap-

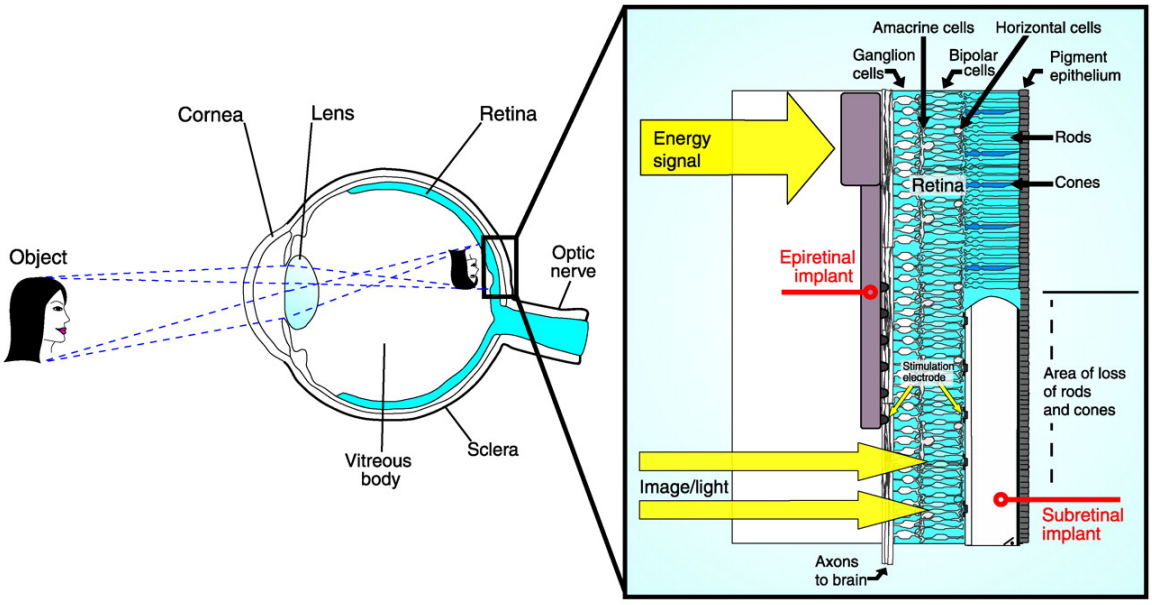

Figure 1.1: The sub-retinal implant replaces the photoreceptors by microphotodiodes and corresponding stimulating microelectrodes. On illumination by incident light, the photodiodes inject currents into the electrodes which stimulate the remaining network of nerual cells; The epi-retinal implant receives signals from the intraocular signal processing and directly stimulate the axons of the ganglion cells. (Figure adapted with permission from [6]).

proach [13, 14, 15], where the implanted device is located between the pigment epithelial layer and the outer layer of the retina, which contains the photoreceptor cells. Figure 1.1 depicts the physical implanted location of the sub-retinal implant. In this location, incident light (from the lens) will illuminate the implanted device. The implant consists of thousands of micro-photodiodes equipped with microelectrodes assembled on a very thin plate. These micro-photodiodes and microelectrodes combine to directly replace the photoreceptor functionality. When the photodiodes get illuminated by incident light with sufficient intensity, they generate currents to activate the microelectrodes. These microelectrodes attempt to stimulate the surviving retinal sensory network. Once stimulated, the network of retinal cells will perform the complex information processing part of vision just as they do in a healthy eye.

In this manner, the stimulation sequence conforms to the natural biological sequence which results in a retinotopically correct pattern transmitted to the further sensory pathways. The main advantages of this approach are the ease in orienting and fixing the implant in the subretinal space, no power sources required, and the absence of any extraocular devices for image capture and intraocular devices for signal processing. However, the total lack of communication with any external equipment makes it impossible to implement any feedback mechanism or perform real time intelligent modifications to stimulation parameters. Moreover, naturally incident light may not provide enough current generation to be able to stimulate the retinal cells adequately and this approach still needs to be proved with preliminary results.

2) The Epi-retinal Implant: The epi-retinal device is implanted onto the innermost layer of the retina containing the ganglion cells and their axons [16, 17, 18, 19, 20, 21, 22] as shown in Figure 1.1. The implanted microelectrode array acts on received visual information and injects electrical impulses directly onto the ganglion cell axons which carry the signals over the optic nerve to the brain. This form of stimulation bypasses the natural information processing network of surviving retinal cells. Hence, additional visual information translation is required to ensure that the spatiotemporal patterns of electrical impulses injected by the array are understood by the brain. Moreover, this form of implant has no light sensing elements and hence it requires an external (or implanted) mechanism for image capture as well as a source for powering the electrode array. Generally, image acquisition is performed by an extra-ocular camera and power and data communication between the external and implanted units achieved via a wireless telemetry link. This wireless link can be based on optical power and data telemetry employing a laser diode [23] or it may be established inductively between a pair of external and implanted coils at low frequency [24]. The merits of the epi-retinal approach are that most of

the image acquisition and data processing can be accomplished in the extraocular unit. The intraocular unit can include only the receiver coil/element, circuits for power and data recovery and the retinal stimulator besides the ultra thin microelectrode array. This results in a low power unit which retains the flexibility of providing feedback and upgrading the image processing algorithms without re-surgery. A potential drawback of this approach is ensuring the chronic bio-compatibility and mechanical stability of the implant at the electrode array-retinal interface.

Despite their potential drawbacks, in both sub-retinal and epi-retinal approaches, the placement of the implant is in the patient's visual field which facilitates the perception of the stimulated light patterns. The stimulator arrays cover a limited area of the eye's curvature resulting in a restricted field of view known as the 'tunnel vision'. Efforts are underway to fabricate ultra thin, flexible bio-compatible materials which can house microelectrodes and fit neatly into the curvature of the eyeball thus improving the resolution of the excitation.

1.2.1.2 Optical Nerve and Visual Cortex Implants

The other approaches of eliciting visual perception deal with a more direct technique of stimulating the higher regions of the human visual pathway. In the optical nerve approach [25], a cylindrical cuff electrode array is placed around the optic nerve near its connection with the eye [26]. The results have been encouraging and this method has the advantage of not having to consider the complex and delicate issues involved with interfacing the fragile retinal membranes. However selecting the excitation locations to achieve a spatial mapping with the direct visual field of view is generally a greater obstacle in the proper functioning of such implants.

The visual cortex is the final region in the visual pathway which can be stimulated to evoke light perceptions [27, 28]. While the epi-retinal and sub-retinal approaches

seek to alleviate patients suffering from retinal diseases like RP and AMD, this approach can benefit any number of visual disorders. However, currently, knowledge of a direct mapping from the eye's field of vision to the complex spatio-temporal regions of the brain's visual cortex does not exist. Hence, analyzing and mapping the spatial correspondence between the visual field and brain's information processing regions remains to be overcome for any degree of success in this approach. Further, this approach carries considerable more surgery related and post-operative risks for the patient.

1.2.2 The NCSU/USC approach and Prototype System

Since the late 1980s, engineers at NC State University and medical doctors and personnel at the Doheny Eye Institute of University of Southern California (formerly at Johns Hopkins University) have been investigating the possibility of restoring partial vision to the blind using an epi-retinal implanted prosthesis. Experiments on blind patients [11, 12] have already confirmed the elicitation of light perceptions on discrete stimulation of the inner retinal membrane. Figure 1.2 depicts the proposed epi-retinal implant system.

The feasibility of such an approach of chronically implanting an ultra-thin electrode array at the vitreo-retinal interface (inner retinal membranes) has been demonstrated in clinical studies conducted in the eyes of dogs [29]. As reported in [29], after several months of implantation, no retinal infections or bleeding were observed. Medical experiments have also estimated that the equivalent impedance for the retina tissue of RP and AMD patients is about $10k\Omega$ and, the current threshold value is about $600\mu A$ [11] leading to a voltage drop of approximately $6V$ across the retinal tissue. They have also determined that the stimulus waveform should be a bi-phasic pulse with a leading cathodic pulse. These preliminary experiments have assisted the

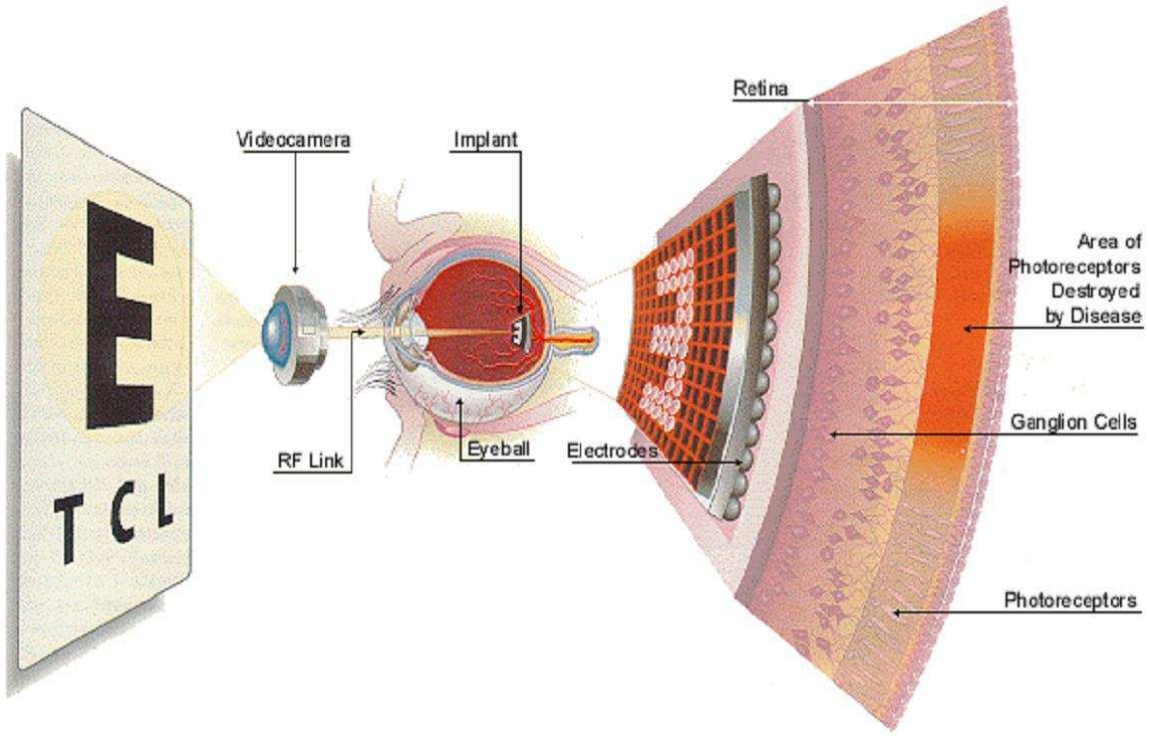

Figure 1.2: The NCSU/USC System approach for the development of an epi-retinal visual prosthesis.

researchers to derive the requisite electrical parameters for stimulation and gather information about the mechanical issues involved for the long term stability of the implant. This has encouraged further efforts to develop a complete prototype system for an epi-retinal implant.

Mechanical and experimental considerations over the years have evolved the design of the implant into two distinct units. The unit external to the eye (referred to as the extra-ocular unit henceforth) is designed to perform the image acquisition and will include the video processing board, a telemetry protocol encoder chip, an amplifier, and primary side telemetry functions for wireless communication with the intraocular unit. The implanted intraocular unit consists of the power recovery, a rectifier and regulator, a retinal stimulator with a telemetry protocol decoder and stimulus signal generator which drives the electrode array on the retinal membrane with the requisite

charge pulses.

The intraocular unit of the epi-retinal device requires power to drive the electronic circuits (ICs) which perform the RF and data recovery and the current stimulator which drives the electrode array. An implanted power source is an impractical alternative due to mainly two reasons: (i) unlike in a heart pacemaker, the implanted electronics in a retinal prosthesis need a substantial amount of power for data processing, for monitoring bio-functions or device status, performing back telemetry (feedback mechanism) and to enforce neuronal stimulation. This imparts to the power source a bulky and heavy composition which makes it difficult to be made bio-compatible and secondly, (ii) implanted batteries need to be frequently replaced which, in this case, will necessitate a delicate and often painful and inconvenient re-surgery procedure involving the eye. Hence generally, for ocular prosthetic devices, it is advisable that power gets transmitted from external sources to the implant. Moreover, unlike the sub-retinal implant, an epi-retinal implant will need visual information (data) transmission from external image capture mechanisms. Both power transfer and data communication (which can be bi-directional) is accomplished using transcutaneous links with the implant.

1.2.3 Wireless Power and Data Telemetry

Percutaneous connectors (physically wired links between the implant and external components) have been reported previously in long term bio-compatibility studies [30]. However, percutaneous connections are unsuitable since very often they lead to the following complications:

- Risk of Infection: Due to chronic breakage of skin at the tethering location, such connections are unhealthy and raise the risk of infections.

- Reaction to excessive movement: The constant presence of mechanical tethering restricts the movement of the implant to only specific tissues. The voluntary movement of these tissues/muscle tendons can cause internal damage and lead to complications.

- Device dislodging: Due to movement of wires and the eyeball across the skin, mechanical stress on the electrode array can dislodge if from its carefully established location on the retinal membrane and damage the prosthetic system.

Hence, due to these factors, wireless telemetry of data and power is preferred for ocular implants. The most commonly employed wireless power and data telemetry technique is via inductive coupling in a pair of coils which will be described below.

1.2.3.1 Inductive Telemetry

Power transfer and data communication via an inductive link has been extensively reported and is the conventional means of coupling the external and internal (implanted) portions of neuro-prosthetic devices [33, 34, 35, 36, 37, 38]. It is accomplished by mutual magnetic flux linkages between two coplanar, coaxial and proximal coils at low frequencies (1–10 MHz). The primary coil resides on some mechanical support external to the body/organ while the secondary coil is implanted in the tissue/body location housing the prosthetic electronics. Power transfer is achieved at the low coupling frequencies and data communication is carried out by modulating the power carrier with the information signal. The coils are air-coupled for biomedical applications since the use of magnetic material as cores for the coils may lead to undesirable physiological effects due to Electromagnetic Interference (EMI) from extraneous magnetic fields and also may cause problems in case of the patient is subjected to MRI scans. There are 3 main criteria which are used to optimize the inductive link for a bio-implant:

(a) Power transfer efficiency: This is a measure of how well the energy supplied to the primary coil gets coupled (or transferred) to the secondary coil. Strong coupling is of prime importance for biomedical implants due to their focus on power as well as data transfer via the inductive link. Coupling strength is dependent on several coil parameters like coil loading, excitation frequency [39], coil separation [40], coil geometry [41, 42] and angular alignment. Typical values for coil coupling are between 0.01 and 0.1 [43].

(b) Driving efficiency: This design parameter is a measure of how much power from the supply is dissipated in the driving circuit compared with exciting the coil itself. If the power consumption in the amplifier driving circuit is reduced, a low coupling coefficient between the coils can be compensated by driving the primary coil at higher magnetic field strength.

(c) Carrier modulation bandwidth: For a data intensive prosthetic device such as a visual prosthesis, the available bandwidth for data transmission is of critical importance. Several current designs for neurostimulators, employ digital communication protocols and modulation techniques for data transmission [43]. A most general scheme is accomplished by modulating the power carrier by a conventional ASK (Amplitude shift keying) or PSK (Phase shift keying), OOSK (On-Off shift Keying) or the improvement in ASK known as the Suspended Carrier Modulation [43].

In the first generation prototype system, a single inductive link was designed for both power and data communication for a 10 x 10 electrode array [43] (it has not been implemented yet). The video camera received visual information and the extra ocular unit provided additional image processing to encode the data with a specific transmission protocol. This data is further processed by a pulse width modulation circuit (PWM) and subsequently modulated onto an RF power carrier using amplitude shift keying (ASK). The modulated carrier is transmitted inductively via coil

coupling to the intraocular unit. At the receiver, the configuration/image data is extracted from the digital PWM signal through the reverse process of encoding. This data is used as a specification for the generation of the current pulses which drive the electrode array on the retinal membrane. In such a scheme, a data rate of 25-250 kb/s can be achieved with a 1–10 MHz carrier frequency [24].

1.3 Potential Drawbacks of Inductive Data Telemetry for a Visual Prosthesis

An essential aspect of the retinal prosthesis is the design of an efficient telemetry link for transferring both power and data. The primary goal of the Visual prosthesis is to transfer high quality visual data in the form of high resolution images to the implant in real time so as to ensure an accurate and sharp visual perception. Thus, a visual prosthesis is potentially a data intensive device requiring a large bandwidth. Towards this end, research efforts to assemble a large number of electrodes in a densely compact form on an ultra thin and flexible membrane which fits neatly into the curvature of the eyeball–to make it implantable on the retina, are also underway. This research will yield ultra-compact and dense and thin electrode arrays made of implantable bio-compatible material which will increase the resolution thus requiring a greater data bandwidth. Using inductive coupling, a retinal prosthetic scheme can be implemented for both power and data transfer at carrier frequencies of not higher than a few tens of MHz [45]. A data bandwidth of up to 3-4 Mbps [44] may be achieved by modulating the power carrier with the complex modulation schemes. Recent work [45] shows that a for a simplified visual implant with a reasonable resolution of only 32 x 32 pixels for an image requires 10 bits for addressing, 8 bits for 256 gray levels, and 2 bits for polarity and parity checking. Considering the human eye's natural bandwidth to be

60 frames/sec, 1.23 Mbps of just data signal would be required. It is further shown that a low frequency inductive link with novel Frequency Shift Keying (FSK) can have sufficient bandwidth for a 2–3 Mbps data signal.

However, this may not be sufficient to transmit real time visual information with the desired resolution to the implanted electronics. Also, with the advancement in array miniaturization technology, far denser arrays will become a reality and necessitate a much higher bandwidth. Transferring both data and power via the same inductive link has a performance drawback in that the data bandwidth is dependent upon the carrier frequency and hence a low frequency inductive link alone may prove to be insufficient in designing an optimum telemetry link. An obvious means to increase bandwidth of the inductive link is to operate with a higher carrier frequency of a few hundred MHz. A higher data bandwidth can be achieved since the visual information in the form of telemetry encoded data, now modulates the higher carrier frequency. However, there are a few inherent limitations of using coils for inductive coupling at high frequencies as outlined below:

- At high frequencies, the coils tend to self resonate due to parasitic capacitance– an undesirable feature in the power circuit.

- The power transfer efficiency of the coils
  $\eta_{powertransfer} \propto Q_{unloaded}$
  and hence a tradeoff exists between the desired power transfer efficiency and the maximum bandwidth achievable.

- In the intraocular unit, the carrier frequency is rectified and converted into regulated DC power for the signal processing chips. At higher frequencies the efficiency of rectification may reduce due to the finite switching times of the semiconductor devices involved.

These issues have to be resolved before inductive coupling can be employed at high frequencies and hence significant research work needs to be done to determine the feasibility of high frequency inductive telemetric links.

1.4 Proposed Novel Approach

We propose an alternative method of *mutually exclusive* power and data transfer [46]. In this approach, power transfer is still carried out through coils via an inductive link at low frequencies of 1–10 MHz. However, we propose to isolate the data transfer from the power carrier and set up a microwave link at high frequencies to transmit data using a pair of external and internal (implanted) antennas. Hence, while the power transfer continues at low frequencies by coupling two coils inductively, data transfer is carried out, entirely independently of the power link, at microwave frequencies (1–3 GHz) by coupling a pair of antennas. This eliminates the data bandwidth dependency on the power carrier. Thus, the available information bandwidth has a potential to increase significantly if data transfer is carried out by modulating a much higher frequency carrier. Also, since design methodologies for both the power and data links are different, they can be developed exclusively of each other leading to an overall optimum design of the telemetry link. In this work, we investigate this novel approach and have employed microstrip patch antennas as coupling elements for data transfer. Microstrip patch antennas and meander line wire antennas were investigated for the external (extra ocular) and implanted units owing to their light weight durable structure.

It must be mentioned that, at microwave frequencies the data signal incurs a path loss due to propagation through space as well as in the anterior eye and head tissue. Hence, this will necessitate very sensitive receiver architecture in the implanted unit.

Also, the received signal will have to be amplified significantly before further signal processing can be carried out and this will consume the already scarce real estate and add to the complexity in the implanted unit electronics. Nevertheless, as the next generation of biocompatible electrode arrays are realized and receiver architectures get further refined, an alternative means for establishing power and data links will become a necessity in order to optimize the overall link efficiency. This research work attempts to investigate novel approaches towards achieving this objective and demonstrates the feasibility of mutually exclusive power and data links for biomedical prosthetic implants (in this case a visual prosthesis).

1.5 Dissertation Overview

In this work, we investigate novel designs of extremely compact antennas for wireless applications and outline the means by which such size reduction concepts may be utilized to design antennas for human body implantation (specifically, inside the eye for a retinal prosthesis). We also study the feasibility of establishing microwave data telemetry links using external and implanted antennas for a retinal prosthesis. Comprehensive computational (using Finite Difference Time Domain) and experimental evaluation of the microwave data telemetry link employing antennas at two frequency bands of 1.45 GHz and 2.45 GHz is reported. Besides, we also study the interaction of the electromagnetic fields associated with the operation of the inductive link (for power transfer) and microwave link (data communication) with the human head and characterize the thermal elevation due to the implanted electronics' power dissipation. Since, this was an innovative undertaking, several challenges had to be overcome relating to the design and fabrication of ultra-compact antennas which withstand the extreme inductive loading influence of the vitreous humor of the eyeball, in the devel-

opment of a high resolution (0.25 mm) human body model to facilitate the accurate characterization of the fine eye and head tissue details, and in discretizing and implementing the bio-heat equation in 3-dimensions. A brief outline of all the chapters is provided below.

A significant portion of the work for developing the telemetry link involved novel compact antenna design techniques using numerical methods and its experimental verification. Chapter 2 describes briefly the salient features of microstrip patch antennas and the Finite Difference Time Domain Method (FDTD) which was employed extensively in designing the antennas and in characterizing the data telemetry link.

Chapter 3 describes the application of such size reduction techniques to conventional wireless applications. It demonstrates the implementation of a novel compact dual polarized microstrip patch antenna for mobile network nodes utilizing polarization diversity to improve channel capacity.

Chapter 4 describes the design of the compact extra ocular and intraocular antennas for a retinal prosthesis and the numerical and experimental investigation of the data telemetry link at 1.45 GHz and 2.45 GHz. Also, the electromagnetic power deposited in the head and eye tissues is characterized in the form of Specific Absorption Rate (SAR) and determined to be within the IEEE/ANSI stipulated guidelines as mentioned in [47].

In the eventual prototype system, intraocular antenna and the implanted electronic circuitry are expected to share the same substrate (due to space constraints). Microstrip patch antennas require a ground plane and with current fabrication technology, it is rather cumbersome to bond a metal layer like aluminum (ground plane) to silicon wafer. Also, in the implanted unit, the secondary coil (for power coupling) encloses the antenna and a metal surface occupying the area within the coil reduces the flux linkages required for inductive coupling. Hence, in Chapter 5 we investigate

the possibility of using extremely small novel wire antennas (dipoles) as receiving elements in the data telemetry link.

The inductive link (coils) and microwave data link (antennas) lead to EM power deposition in the eye and head tissues which indirectly causes heating. Moreover, the implanted IC chips dissipate a substantial amount of power which causes direct temperature rise of the eye tissues. In Chapter 6, the bio-heat equation is discretized in three dimensions and implemented using FDTD to numerically determine the extent of thermal elevation in the eye and head tissues. This information aids in establishing specific performance constraints which are necessary for the safe operation of the entire prosthetic system.

Chapter 2

Finite Difference Time Domain (FDTD) method and Antenna Design Issues

2.1 Introduction

Computational electromagnetics plays a vital role in assisting engineers and researchers investigate the behavior of complex 3-dimensional structures and the interaction of fields with dielectric media (which can possess material inhomogeneities). The existing numerical techniques solve Maxwell's coupled curl partial differential equations involving electric and magnetic fields. Amongst the numerous techniques available for numerically solving partial differential equations, three have been used widely for solving Maxwell's equations at high frequencies where the dimensions of the structure are comparable to the wavelength of the incident or radiated electromagnetic waves: the *Method of Moments (MoM)* [48], the *Finite-Element Method (FEM)* [49] and the *Finite Difference Time Domain Method (FDTD)* [50].

The Finite Difference Time Domain (FDTD) method has been used extensively in the research work contributing to this dissertation. Both MoM and FEM are frequency domain methods and were used widely until about 1985, but lately, because of their implicit computational technique, the memory limitations in modelling 3-dimensional structures have restricted their use to mainly antenna and microstrip problems. In contrast, the FDTD is an explicit scheme and there is no intrinsic upper bound to the number of unknowns it can solve. Also, it being a time domain technique, treats impulsive and non-linear behavior naturally. FDTD allows accurate modelling of antenna near and far fields for arbitrary configurations of inhomogeneous media. Hence, FDTD is essential in bio-electromagnetics and characterizing the interaction of EM fields with the tissues of the human body. We have also used FDTD in the design of novel micro-antennas and dual polarized antennas. Moreover, FDTD enabled us to perform a comprehensive numerical characterization of the data telemetry link comprising of the intraocular and extraocular antennas for the retinal prosthesis in the presence of the human head model.

The next section presents the basic theory about the FDTD method and discusses the salient features of the absorbing conditions.

2.2 Finite Difference Time Domain Method

Mathematically, Finite Difference Time Domain (FDTD) is just a direct discretization and implementation of Maxwell's curl equations in time and space and hence unlike other numerical techniques, analytical preprocessing and modeling are almost completely absent in FDTD. It is capable of predicting broadband response since it is in the time domain and can also analyze lossy and anisotropic materials, ferrites and plasmas. FDTD simulation of any problem includes dividing the region under

consideration into different material properties (by modeling the proper structure to be analyzed) and finally the unbounded region is terminated by absorbing boundary conditions to prevent the wave (or EM fields) from reflecting. Next, the physical space of the problem is discretized in the form of cubes (or cuboids) with dimensions $\Delta x \Delta y \Delta z$ and the time of simulation is also divided into Δt interval steps. The source of EM energy is then introduced into the physical domain in the form of pulse or a plane wave and allowed to interact with the structure and finally the time domain information is processed to determine the electromagnetic behavior of the structure.

Maxwell's curl equations involving $\vec{E}$ and $\vec{H}$ for any linear isotropic media with material constants ϵ, μ, and σ are given as :

$$\nabla \times \vec{\mathbf{H}} = \sigma \vec{\mathbf{E}} + \epsilon \frac{\partial \vec{\mathbf{E}}}{\partial t} \tag{2.2.1}$$

$$\nabla \times \vec{\mathbf{E}} = -\mu \frac{\partial \vec{\mathbf{H}}}{\partial t} \tag{2.2.2}$$

These equations can have unique solutions when the following conditions are specified: (i) The value of fields at $t = 0$ must be specified on the whole domain. (ii) The tangential components of $\vec{\mathbf{E}}$ and $\vec{\mathbf{H}}$ on the boundary of the domain must be given for all $t > 0$.

Finite difference approximations are used to solve the above mentioned partial differential equations and for higher accuracy, a central difference scheme is utilized :

$$\left.\frac{\partial F}{\partial u}\right|_{u_0} = \left.\frac{F\left(u_0 + \frac{\Delta u}{2}\right) - F\left(u_0 - \frac{\Delta u}{2}\right)}{\Delta u}\right|_{\Delta u \to 0} + O(\Delta u)^2 \tag{2.2.3}$$

FDTD is implemented in 3-dimensions by discretizing the space into number of cells known as the Yee cells. Discretization means that both $\vec{\mathbf{E}}$ and $\vec{\mathbf{H}}$ should be determined only at discrete spatial locations (x_i, y_i, z_i) where i is the ith cell in the spatial lattice. As shown in the Yee cell, both $\vec{\mathbf{E}}$ and $\vec{\mathbf{H}}$ are off in space such that

their component's positions satisfy the differential form of Maxwell's equations. Also, both the $\vec{\mathbf{E}}$ and $\vec{\mathbf{H}}$ field components are off by half a time step leading to a leap-frog scheme with the components of $\vec{\mathbf{E}}$ being calculated at $n\Delta t$ time step and those of $\vec{\mathbf{H}}$ being computed at $(n+1/2)\Delta t$ time step.

Equations and are discretized in time and space leading to six equations for all the components as outlined below [51] :

$$\begin{aligned} E^{n+1}_{x\left(i+\frac{1}{2},j,k\right)} &= \left(\frac{\epsilon-\sigma\Delta t/2}{\epsilon+\sigma\Delta t/2}\right) E^{n}_{x\left(i+\frac{1}{2},j,k\right)} \\ &+\frac{\Delta t/\Delta y}{\epsilon+\sigma\Delta t/2}\left(H^{n+1/2}_{z\left(i+\frac{1}{2},j+\frac{1}{2},k\right)} - H^{n+1/2}_{z\left(i+\frac{1}{2},j-\frac{1}{2},k\right)}\right) \\ &-\frac{\Delta t/\Delta z}{\epsilon+\sigma\Delta t/2}\left(H^{n+1/2}_{y\left(i+\frac{1}{2},j,k+\frac{1}{2}\right)} - H^{n+1/2}_{y\left(i+\frac{1}{2},j,k-\frac{1}{2}\right)}\right) \end{aligned} \tag{2.2.4}$$

$$\begin{aligned} E^{n+1}_{y\left(i,j+\frac{1}{2},k\right)} &= \left(\frac{\epsilon-\sigma\Delta t/2}{\epsilon+\sigma\Delta t/2}\right) E^{n}_{y\left(i,j+\frac{1}{2},k\right)} \\ &+\frac{\Delta t/\Delta z}{\epsilon+\sigma\Delta t/2}\left(H^{n+1/2}_{x\left(i,j+\frac{1}{2},k+\frac{1}{2}\right)} - H^{n+1/2}_{x\left(i,j+\frac{1}{2},k-\frac{1}{2}\right)}\right) \\ &-\frac{\Delta t/\Delta x}{\epsilon+\sigma\Delta t/2}\left(H^{n+1/2}_{z\left(i+\frac{1}{2},j+\frac{1}{2},k\right)} - H^{n+1/2}_{z\left(i-\frac{1}{2},j+\frac{1}{2},k\right)}\right) \end{aligned} \tag{2.2.5}$$

$$\begin{aligned} E^{n+1}_{z\left(i,j,k+\frac{1}{2}\right)} &= \left(\frac{\epsilon-\sigma\Delta t/2}{\epsilon+\sigma\Delta t/2}\right) E^{n}_{z\left(i,j,k+\frac{1}{2}\right)} \\ &+\frac{\Delta t/\Delta x}{\epsilon+\sigma\Delta t/2}\left(H^{n+1/2}_{y\left(i+\frac{1}{2},j,k+\frac{1}{2}\right)} - H^{n+1/2}_{y\left(i-\frac{1}{2},j,k+\frac{1}{2}\right)}\right) \\ &-\frac{\Delta t/\Delta y}{\epsilon+\sigma\Delta t/2}\left(H^{n+1/2}_{x\left(i,j+\frac{1}{2},k+\frac{1}{2}\right)} - H^{n+1/2}_{x\left(i,j-\frac{1}{2},k+\frac{1}{2}\right)}\right) \end{aligned} \tag{2.2.6}$$

$$
\begin{aligned}
H^{n+1/2}_{x\left(i,j+\frac{1}{2},k+\frac{1}{2}\right)} &= H^{n-1/2}_{x\left(i,j+\frac{1}{2},k+\frac{1}{2}\right)} \\
&\quad -\frac{\Delta t}{\mu\Delta y}\left(E^{n}_{z\left(i,j,k+\frac{1}{2}\right)} - E^{n}_{z\left(i,j-1,k+\frac{1}{2}\right)}\right) \\
&\quad +\frac{\Delta t}{\mu\Delta z}\left(E^{n}_{y\left(i,j+\frac{1}{2},k\right)} - E^{n}_{y\left(i,j+\frac{1}{2},k-1\right)}\right)
\end{aligned} \tag{2.2.7}
$$

$$
\begin{aligned}
H^{n+1/2}_{y\left(i+\frac{1}{2},j,k+\frac{1}{2}\right)} &= H^{n-1/2}_{y\left(i+\frac{1}{2},j,k+\frac{1}{2}\right)} \\
&\quad -\frac{\Delta t}{\mu\Delta z}\left(E^{n}_{x\left(i+\frac{1}{2},j,k\right)} - E^{n}_{x\left(i+\frac{1}{2},j,k-1\right)}\right) \\
&\quad +\frac{\Delta t}{\mu\Delta x}\left(E^{n}_{z\left(i,j,k+\frac{1}{2}\right)} - E^{n}_{z\left(i-1,j,k+\frac{1}{2}\right)}\right)
\end{aligned} \tag{2.2.8}
$$

$$
\begin{aligned}
H^{n+1/2}_{z\left(i+\frac{1}{2},j+\frac{1}{2},k\right)} &= H^{n-1/2}_{z\left(i+\frac{1}{2},j+\frac{1}{2},k\right)} \\
&\quad -\frac{\Delta t}{\mu\Delta x}\left(E^{n}_{y\left(i,j+\frac{1}{2},k\right)} - E^{n}_{y\left(i-1,j+\frac{1}{2},k\right)}\right) \\
&\quad +\frac{\Delta t}{\mu\Delta y}\left(E^{n}_{x\left(i+\frac{1}{2},j,k\right)} - E^{n}_{x\left(i+\frac{1}{2},j-1,k\right)}\right)
\end{aligned} \tag{2.2.9}
$$

The indices define the positions of the field nodes such that $x = i\Delta x$, $y = j\Delta y$ and $z = k\Delta z$. In all the simulations performed towards this research work, an explicit D-H algorithm was employed which simplifies the application of absorbing boundary conditions and is explained in detail in [52].

2.2.1 Stability Criterion

The numerical algorithm is second order accurate in both space and time and being an explicit method, it requires an upper bound on the time step Δt for stability. If Δt exceeds this bound, the algorithm tends to compute results which are non-physical

and increase without limit. The stability analysis is discussed thoroughly in [53] and leads to a final upper bound for Δt given as:

$$v_{max} \cdot \Delta t \leq \frac{1}{\sqrt{\frac{1}{\Delta x^2} + \frac{1}{\Delta y^2} + \frac{1}{\Delta z^2}}} \tag{2.2.10}$$

where v_{max} is the maximum phase velocity of the wave in the problem under consideration.

2.2.2 Absorbing Boundary Conditions

It is necessary to terminate the computational domain to conform to the available computational resources. Most electromagnetic problems entail a structure whose behavior is to be studied in an unbounded domain. Since, it is impossible to simulate infinite physical domains, the computational space is terminated by absorbing boundary conditions which effectively simulate an unbounded region (by preventing reflections from the edges). This is accomplished in the computational domain by an exterior region (which incorporates the absorbing boundary conditions (ABCs)) and an interior region (wherein the structure to be investigated is modelled). An ABC can be achieved in several ways and are classified into either analytical ABC or material ABC. Analytical ABCs are simulated by approximating the wave equation at the boundary while the material ABCs incorporate a lossy medium to physically absorb the incident wave. In this research work, we have employed material ABC known as the Perfectly Matched Layer (PML) which is briefly summarized below.

2.2.2.1 Perfectly Matched Layer (PML) ABC

The perfectly matched layer (PML) absorbing boundary condition was proposed in 1994 [54]. To understand the PML technique, we consider the simple TE case in

two dimensions, with relevant field components given by E_x, E_y and H_z. In this case, the Maxwell's equations become

$$\epsilon\frac{\partial E_x}{\partial t} + \sigma E_x = \frac{\partial H_z}{\partial y} \tag{2.2.11}$$

$$\epsilon\frac{\partial E_y}{\partial t} + \sigma E_y = -\frac{\partial H_z}{\partial x} \tag{2.2.12}$$

$$\mu\frac{\partial H_z}{\partial t} + \sigma^* H_z = \frac{\partial E_x}{\partial y} - \frac{\partial E_y}{\partial x} \tag{2.2.13}$$

where ϵ and μ are the permittivity and permeability respectively and σ and σ^* are the electric and magnetic conductivities.

Now, if the medium has intrinsic impedance equal to

$$\eta = \sqrt{\frac{\mu}{\epsilon}} \tag{2.2.14}$$

and if the condition

$$\frac{\sigma}{\epsilon} = \frac{\sigma^*}{\mu} \tag{2.2.15}$$

holds, then mathematically no reflection occurs when a plane wave propagates normally across an interface between the medium with the dielectric properties of ϵ and μ and a medium with identical dielectric properties and electric and magnetic conductivities of σ and σ^* respectively. In case of oblique incidence, there would be reflections and to make it reflectionless for any angle of incidence, it is necessary to introduce a new degree of freedom by splitting H_z into two subcomponents indicated as H_{zx} and H_{zy}. Hence, we obtain a system of four coupled equations instead of three:

$$\epsilon\frac{\partial E_x}{\partial t} + \sigma_y E_x = \frac{\partial(H_{zx} + H_{zy})}{\partial y} \tag{2.2.16}$$

$$\epsilon\frac{\partial E_y}{\partial t} + \sigma_x E_y = -\frac{\partial(H_{zx} + H_{zy})}{\partial x} \tag{2.2.17}$$

$$\mu\frac{\partial H_{zx}}{\partial t} + \sigma_x^* H_{zx} = -\frac{\partial E_y}{\partial x} \tag{2.2.18}$$

$$\mu\frac{\partial H_{zy}}{\partial t} + \sigma_y^* H_{zy} = \frac{\partial E_x}{\partial y} \tag{2.2.19}$$

where σ_x, σ_y represent the electric conductivities and σ_x^*, σ_y^*, the magnetic conductivities. It is possible to show that if $\sigma_y = \sigma_y^* = 0$ the PML medium can absorb a plane wave propagating in the x direction with field components (E_x, H_{zx}), but it cannot absorb a plane wave with field components (E_x, H_{zy}) propagating in the y direction. The situation would be reverse if $\sigma_x = \sigma_x^* = 0$.

An extension to three dimensions is a simple generalization of the theory presented for the two dimensional case and for brevity would not be outlined here.

However, it should be noted that for the FDTD computational work in this dissertation, a different formulation of the algorithm and absorbing boundary conditions than what is described above is used. This formulation is a derivation of the basic algorithm as described above and is called the D-H method and is comprehensively explained in [52].

The next section and subsections present a brief outline of the antenna designs considered and summarizes the salient features of microstrip patch antennas and means to make them electrically compact.

2.3 Antenna Design Issues

Several types of antennas were considered for their use as extraocular and embedded intraocular elements for the applications in this dissertation. Antennas in very

common use include Wire antennas, Aperture antennas, Microstrip antennas, Array antennas, Reflector antennas and Lens antennas [55, 56, 57, 58]. Aperture antennas are generally used at higher frequencies and find use in aircraft and spacecraft applications. Array antennas are a combination of several antennas of one type and are used to get highly directive radiation characteristics which may not be available with a single element. Dish antennas are also known as reflector antennas and are mainly used for radio astronomy and space applications owing to the very high gain they can achieve whereas lens antennas are mainly used to collimate divergent energy into plane waves. While these antenna types can be used in a variety of applications, they may not be particularly suitable for biomedical devices due to the difficulty in miniaturizing them. Another class of antennas is the Wire antennas which are used almost everywhere from spaceborne aircrafts to commercial applications in the form of dipoles, loops and helix.

Our work here has been directed towards designing antennas for such diverse applications as Biomedical Engineering and Wireless Communications. Wire antennas can be utilized for embedded bio-medical applications due to the ease with which size reduction techniques can be applied to them. Also, microstrip antennas are attractive for their low weight and conformal nature and are very versatile in terms of operating frequency, radiation characteristics and impedance. Microstrip patch antennas and wire dipoles were therefore considered for the retinal prosthesis' data telemetry link and for the wireless application considered here.

2.3.1 Microstrip Patch Antennas

Microstrip patch antennas consist of a patch of metallization on a grounded substrate [51]. They are low profile and light weight antennas and find enormous applications not only in spacecrafts, satellite, missiles and other defense and aerospace

applications but also in commercial devices such as mobile radio and wireless communications due to their small size conformal and robust structure and ease of installation. They have a low-power handling capability and are an extension of microstrip circuits. This feature is employed in microstrip integrated antennas (MMICs) in which circuit functions are integrated with the antenna function giving rise to compact transceivers and spatial power combiners. Microstrip antennas are very agile in terms of its electromagnetic behavior (its impedance, radiation, polarization and resonant frequency characteristics) and have been analyzed theoretically in [59]—[65] and more recently in a compact, comprehensive treatment [51]. The thin metallic patch is placed a small fraction of a wavelength above a ground plane. The patch and ground plane may be separated by a thin layer of dielectric material (with dielectric constants usually in the range of $2.2 \leq \epsilon_r \leq 14$) known as the substrate. The length of the patch L is usually $\lambda_0/3 < L < \lambda_0/2$. The patch is fed and shaped in such a way so as to obtain the pattern maximum in the normal direction to the patch which is known as the broadside direction. The feed mechanism for patch antennas is discussed in 2.3.1.1, followed by a brief summary of its analysis for a cavity model approximation in 2.3.1.2. Finally, 2.3.1.3 presents the commonly used techniques for size reduction of antennas and their application to microstrip patch antennas with general examples.

2.3.1.1 Feed Mechanisms for Microstrip Patch Antennas

Selection of the feeding technique is governed by several factors the most important of which is the consideration of efficient power transfer from the feed structure to the radiating structure. Properly designed feed structures (for impedance matching) can maintain very low (acceptable) levels of spurious radiation and minimize the cross-polar component of the radiation pattern.

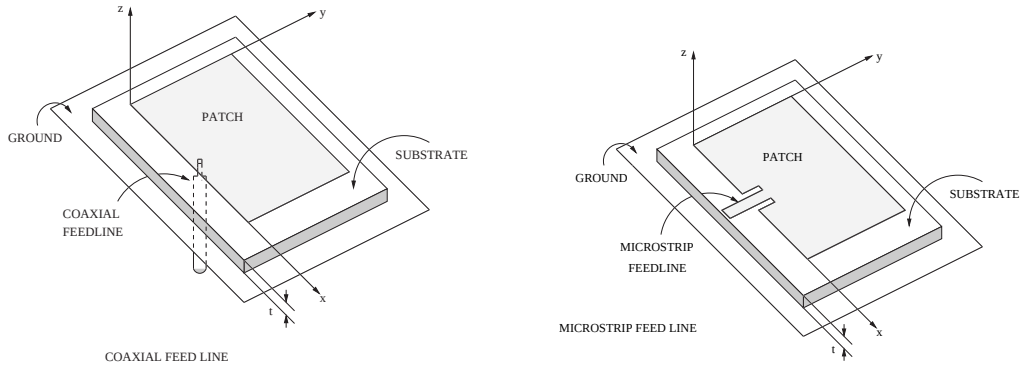

(a) (b)

Figure 2.1: Direct connection feeding methods: (a) Coaxial (probe) feed; and (b) Microstrip feed.

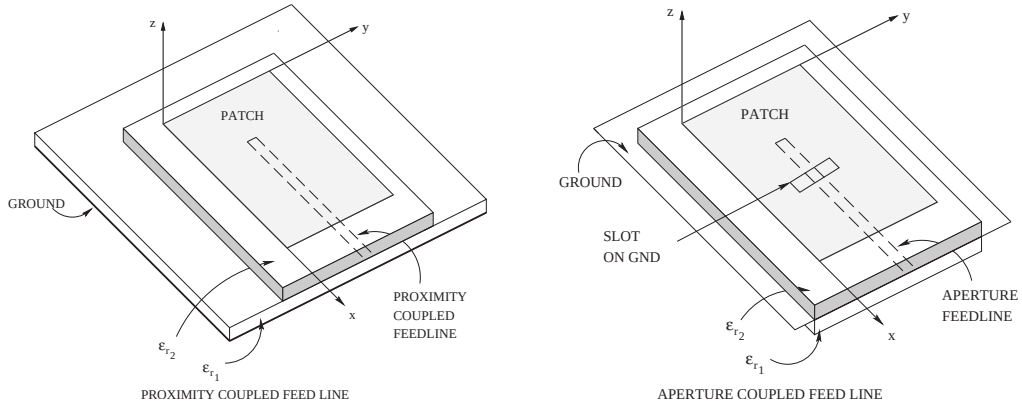

(a) (b)

Figure 2.2: Electromagnetically coupled feeding methods: (a) Proximity coupled feed; and (b) Aperture coupled feed.

There are mainly four configurations that are used to feed the microstrip patch antennas [51] as shown in the Figures 2.1(a), 2.1(b) and Figures 2.2(a), 2.2(b). The probe feed as shown in Figure 2.1(a) essentially consists of the inner conductor of a coaxial line and is one of the basic mechanisms for transfer of microwave power. The connector is attached to the ground plane of the antenna and the center conductor is soldered to the patch (after passing through the substrate). The location of the feed

point is dependent on the impedance matching required and the desired mode to be excited. A microstrip line can be utilized to feed a patch antenna extended on the same substrate as shown in Figure 2.1(b). This technique introduces a discontinuity between the line and the antenna. Coplanar microstrip feeds are easy to design and fabricate and lend reliability to array structure designs. However, the feed structure contributes to spurious radiation. Electromagnetically coupled feeds (non contacting) are shown in Figure 2.2(a). This requires a two layer substrate design with the patch metallization on the top layer and the feed structure on the bottom layer. Capacitive coupling between the feed and patch leads to energy transfer. The double layer design gives a larger bandwidth and several parameters of the substrate (the dielectric constant, thickness) can be adjusted to increase the bandwidth. For the aperture coupled feeds, as shown in Figure 2.2(b), a common ground plane separated the two substrate layers containing the patch and the feed line. The feed line is electromagnetically coupled to the patch through a slot aperture in the common ground plane. The slot and the substrate design parameters can be selected to optimize the feed and radiation functions independently. Notable features of this configuration are wider bandwidth and shielding of the patch from the radiation of the feed structure.

2.3.1.2 Radiation Mechanism and Cavity Model Analysis

Microstrip antennas can be modelled as dielectric loaded cavities. Leakage of energy from these cavities leads to radiation from the antenna and therefore thick substrates and low permittivity are employed for patch antennas. Radiation from a microstrip antenna can be determined from the field distribution between the patch metallization and ground plane. Also, radiation can be characterized in terms of the current distribution on the patch surface. The latter approach is a far more complex one and here, a simple model and crude approximations are used to develop a

workable model for a microstrip antenna. The fields within the dielectric substrate are determined by treating the substrate as a cavity surrounded by perfect electric conducing walls on top and bottom and perfect magnetic walls around the periphery along the edges [55, 60]. These four sidewalls represent the narrow apertures through which radiation takes place. If the walls of the cavity and the dielectric within it are considered as lossless, the cavity would not radiate and the input impedance would be purely reactive. Hence, loss mechanism in the form of radiation resistance R_r and loss resistance R_L is introduced which would account for radiation. These would allow the input impedance to be complex and an effective loss tangent (as reciprocal of the quality factor Q) is chosen to represent the loss mechanism of the cavity, which will now behave as an antenna. The field radiated by these slots can be determined analytically for the simplest patch antenna using the Field Equivalence principle. The four slots can be represented by surface electric and magnetic current densities

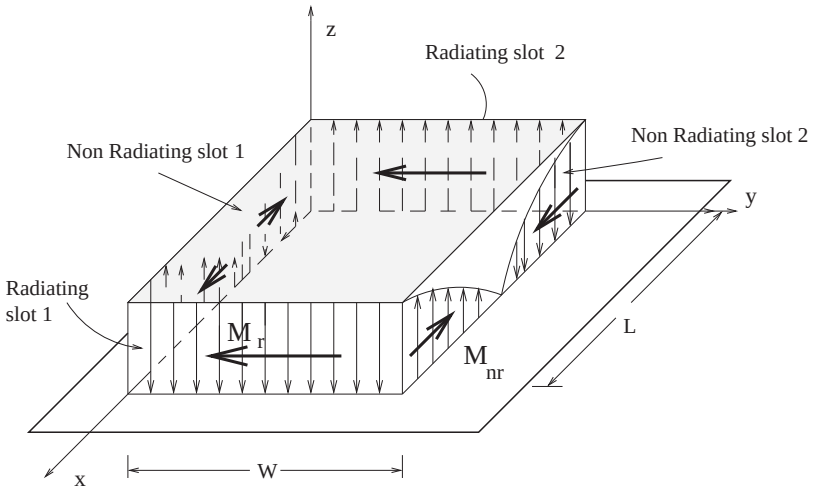

Figure 2.3: Radiating slots with the equivalent current densities for a rectangular patch

$$\vec{\mathbf{J}}_s = \hat{\mathbf{n}} \times \vec{\mathbf{H}}_a \tag{2.3.1}$$

and

$$\vec{\mathbf{M}}_s = -\hat{\mathbf{n}} \times \vec{\mathbf{E}}_a \tag{2.3.2}$$

where $\vec{\mathbf{J}}_s$ is the surface electric current density, $\vec{\mathbf{M}}_s$ is the surface magnetic current density, $\vec{\mathbf{E}}_a$ is the electric field distribution and $\vec{\mathbf{H}}_a$ is the magnetic field distribution on the apertures (slots) of the microstrip patch antenna.

Using aperture theory, the total field radiated by the antenna oriented as shown in Figure 2.3 can be expressed by

$$E_\phi^t = -j\frac{khWE_0e^{jkr}}{\pi r}\sin\phi\cos\theta\left\{\frac{\sin(Y)}{Y}\frac{\sin(Z)}{Z}\right\}\cos\left(\frac{kL_e}{2}\sin\theta\cos\phi\right) \tag{2.3.3}$$

and

$$E_\theta^t = j\frac{khWE_0e^{jkr}}{\pi r}\cos\phi\left\{\frac{\sin(Y)}{Y}\frac{\sin(Z)}{Z}\right\}\cos\left(\frac{kL_e}{2}\sin\theta\cos\phi\right) \tag{2.3.4}$$

where

$$Y = \frac{kW}{2}\sin\theta\sin\phi,\ Z = \frac{kh}{2}\cos\theta \tag{2.3.5}$$

Salient design characteristics for the microstrip patch antennas can be summarized as follows [61]:

- $L \propto 1/(f_0\epsilon_r)$

  Lower the operating frequency, the larger the antenna. High dielectric constant reduces the size.

- BW $\propto t/\epsilon_r$

  Thicker, lower dielectric constant substrate gives higher bandwidth.

- Gain $\propto 1/\epsilon_r$

  High dielectric constant reduces efficiency.

- $R_r = R_0 \cos^2\theta$, where θ is the electrical length from the edge.

  Resonant resistance decreases as we move away from the edge.

These design characteristics can be successfully employed to design simple microstrip patch antennas.

2.3.1.3 Size Reduction Techniques for Microstrip Antennas

Miniaturization in microstrip patch antennas has increasingly received attention since patch antennas can be easily integrated in MMICs and printed board designs. The size of patch antennas is inversely proportional to the resonant frequency and hence methods to miniaturize the antennas are employed to make them operate as electrically small antennas. An antenna is said to be compact when it can operate effectively at a frequency at which its size is a fraction of the free space wavelength. Obviously, a trade off exists in that reducing the size leads to a deterioration in the gain and available bandwidth. The free space radiated wavelength imposes certain basic limits on the size reduction of any antenna which cannot be violated [66, 67, 68, 69, 70]. This subsection discusses the various methods which can be employed to achieve compactness for a microstrip antenna.

For a given physical size of the antenna, if the electrical length of the radiating element is increased, then the coupling free space wavelength is increased and hence the resonant frequency decreases–thus achieving compactness for a given size. This concept is most frequently employed to obtain size reduction [71]. Inductive reactive loading in the form of etching out slots from the surface can lead to increase in the surface current path (and thereby the electrical length of the radiating element) for

a given physical size of the antenna. Reactive loading is also employed in the form of notches or insets at the edges of the patch. In [72] this concept is utilized to introduce reactive loading by placing alternate notches from the non radiating edges to obtain significant size reduction. Several instances of reactive loading have been employed for compactness and summarized in [73].

Another reactive technique often used for size reduction consists in using shorting pins or capacitors between the patch and ground plane. In [74]—[77] extensive investigation on the performance characteristics of patch antennas with shorting pins can be found. A single shorting pin will significantly deteriorate the polarization purity of the patch. Polarization agile patch antennas have been developed and investigated by [78, 79] using more than one shorting pin at strategic locations. There are several explanations put forward to explain the size reduction afforded using shorting pins. According to [80], a shorting pin placed very near to the feed point will introduce a capacitive loading on the feed impedance and will push the impedance circle down on the smith chart thus reducing the resonant frequency. In [74] the effect of different shapes of patch antennas loaded with shorting pins (to obtain compactness) is discussed.

Both the reactive loading techniques were employed in the intraocular microstrip patch antenna designed for the retinal prosthesis application. Inductive loading was introduced in the form of a series of symmetrical slots etched out from the surface and shorting posts were utilized at strategic locations close to the feed point to achieve the desired lowering of operating frequency. Further details of the design procedure are discussed in the chapter 4. Inductive loading techniques are employed to design a novel dual polarized patch antenna as described in the following chapter.

Chapter 3

Novel Size Reduced Dual Polarized Microstrip Patch Antenna for Wireless Applications

3.1 Introduction

A novel, compact, probe fed microstrip patch antenna for operation in dual polarization mode is presented. The novel design is achieved by etching out a symmetric pattern of crossed slots from the surface of a square probe fed patch. Reduction in patch size of up to 51% with respect to a traditional dual-polarized square patch operating at the same frequency is obtained and the potential for further size reduc-

tion is demonstrated. Radiation results show that linear polarizations are obtained in the +45 and −45 degrees with a high isolation of 38 dB between the two ports. Moreover, the salient feature of such a configuration is that the 50Ω feed position can be achieved by moving the feed point along the diagonal of the square patch leading to ease in fabrication.

3.2 Motivation

The explosive growth in broadband wireless communications systems, with rapid advances in the variety and sophistication of the data intensive wireless services being offered, has increased the demands to enhance information accessibility and created a need for more bandwidth-efficient communication techniques. One way to address the capacity increase is by employing polarization diversity [81, 82]. Recent results in communication theory [83] have demonstrated that deploying dual-polarized antennas at the transmitter and/or receiver can dramatically increase both the capacity and diversity of wireless communication links. For example, in the richly scattering environments considered in [83] , a dual-polarized antenna at the transmitter can increase capacity by more than 50% over a single transmit antenna; employing dual-polarized transmit and receive antennas can increase capacity three-fold over a comparable system with single antennas at the transmitter and receiver. The proliferation of portable communications technology has also created a necessity for compactness in the system implementation.

Compactness in the antenna design can help reduce precious real estate on the board design. Here, a novel microstrip patch antenna characterized by polarization diversity is presented. The objective was to explore strategic antenna designs for dual polarization coverage and determine the feasibility of seamlessly integrating such

antenna systems on mobile nodes (portable laptop platforms, PDAs etc.) in a wireless system.

3.3 Concept of Dual Polarization

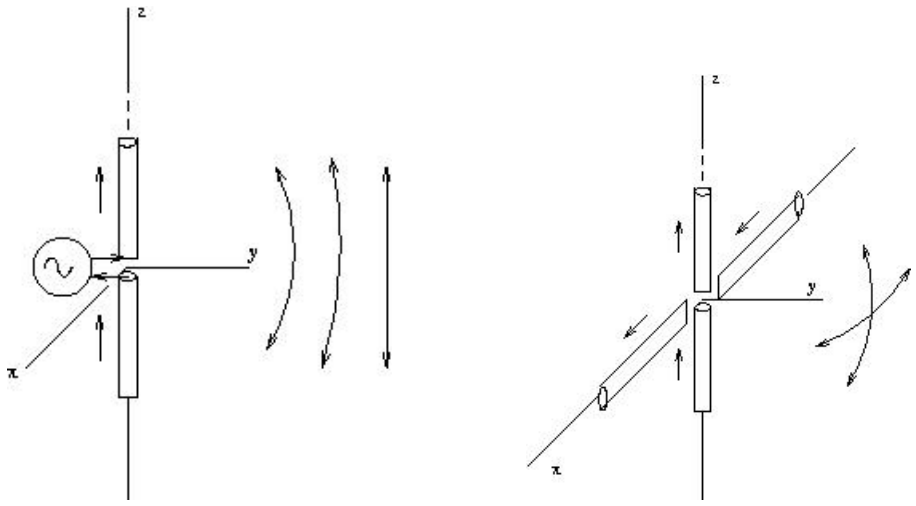

(a) (b)

Figure 3.1: Excitation of linearly polarized antennas: (a) Single polarization; and (b) Dual (orthogonal) polarization.

Dual polarization can be accomplished by exciting modes in two orthogonal directions [84, 85, 86, 87] as shown in Figure 3.1. Size reduction can be achieved by means of reactive loading in the form of notches or slots on the surface of the patch or by employing shorting posts at strategic locations as explained in 2.3.1.3. Even though shorting posts can contribute significantly to the size reduction, in this case they are not employed. Capacitive effects of the shorting posts were found to deteriorate the polarization state of the radiation so significantly that achieving two independent linear states of polarization was not possible. Thus, to realize dual polarization, only inductive loading in the form of slots was employed. Symmetric slot loading causes the meandering of the surface current, thus effectively increasing the surface current

path and the electrical length of the element that leads to reduction of the patch size for a given resonant frequency. Simultaneous etching out of a symmetrical array of slots and the excitation of two orthogonal modes can lead to an antenna with reduced size operating in dual polarization mode.

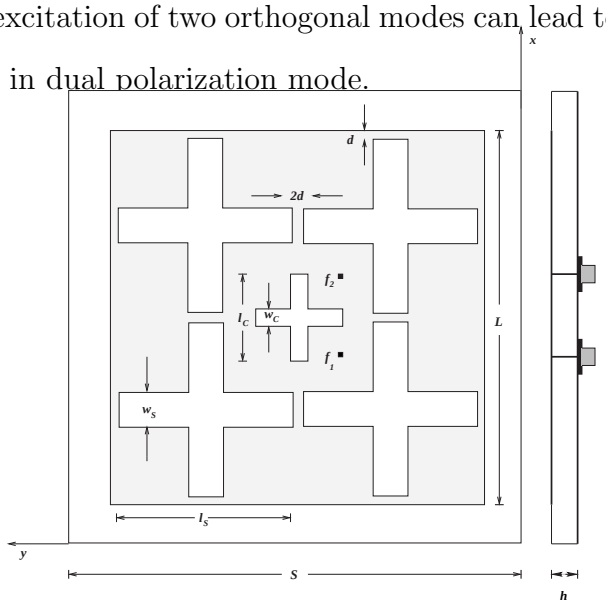

Figure 3.2: Design parameters for the proposed configuration.

3.4 Antenna Design

Even though size reduced dual polarized patch antennas have been reported before [88, 89], the role of the slots in achieving size reduction has not been fully explained. The novel configuration of slots presented here shows an intuitive way of understanding the obtained increase in current path (and hence size reduction). Figure 3.2 shows the proposed, probe fed, dual polarized microstrip patch antenna. Four pairs of crossed slots are etched out—one from each quadrant of the surface and a smaller pair from the center of the patch. The square microstrip patch has a side length L and is printed on a substrate of thickness h and relative permittivity ε_r.

Laminates with a relative permittivity ε_r=3.2 were utilized. The quadrant slot pairs have their sides parallel to the edges of the patch and have a length $l_s$and a width of w_s. The slot pair in the center has a length l_c and a width of w_c. Due to the specific locations of the feed points, the polarizations at the two ports will be along the orthogonal diagonals of the square patch.

The Finite Difference Time Domain (FDTD) algorithm is employed to design and analyze the antenna. For least cross polarization, it is critical that the slots be etched out in a symmetrical pattern such that the surface currents in both the orthogonal directions have to traverse identical paths. To achieve good isolation between the two ports, each feed point is positioned along the 'null-line' of the other port, which comprises of all the locations on the patch where the normal electric field to the patch obtained by feeding the other port is minimum. Figures 3.3(a) and 3.3(b) show the position of the 'null-line' for a conventional dual polarized antenna and the proposed compact dual polarized antenna respectively, as obtained by FDTD simulations. FDTD was used during the design phase of the antenna to locate the position of the null line and, therefore, the location of the feed-points. A resolution of 0.762 mm was used to model the antenna, leading to a total computational space of 160 x 160 x 60 cells. Fifteen PML layers have been used to absorb the outgoing waves with PML parameters chosen as specified in [52, 90].

Several configurations of slots were studied to understand the formation of the 'null-line' and its impedance behavior. The insight gained from these simulations assisted in arriving at the design as shown in Figure 3.2. The FDTD method was also used to obtain the directivity in dBi of the final antenna designs. Confidence in the accuracy of the result was based on an extensive comparison of radiation patterns and directivity obtained for conventional antenna geometries as well as results reported in the literature. Excellent agreement between the numerical results and data reported

Table 3.1: A specification of the parameters defined as shown in Figure 3.2 for the proposed design and for the Reference Antenna. f_r is the operating frequency for each design.

	L (mm)	l_s *(mm)*	w_s*(mm)*	l_c *(mm)*	w_c *(mm)*	f_r *(MHz)*	*Directivity (dBi)*
Antenna-1	67.056	30.480	6.096	18.288	3.048	855.9	0.9
Antenna-2	67.056	25.908	6.096	15.240	3.048	979.7	2.5
Antenna-3	67.056	30.480	3.048	18.288	3.048	880.7	1.3
Reference Antenna	96.770	–	–	–	–	853.6	4.8

in the literature was found for all the considered test cases.

3.5 Results and Discussion

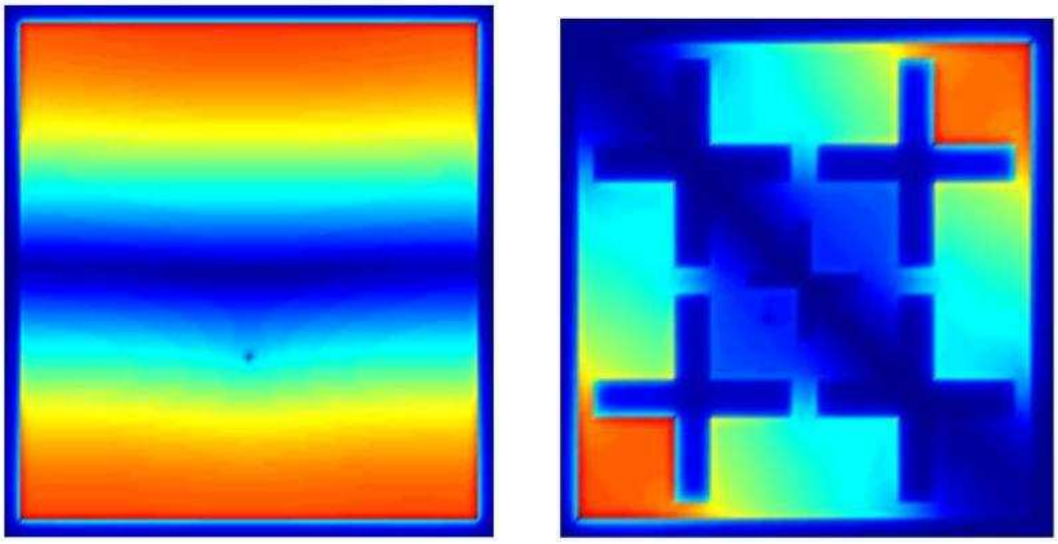

(a) (b)

Figure 3.3: The 'null-line' obtained by exciting one port and terminating the other in its resonant impedance: (a) conventional microstrip antenna; and (b) proposed compact microstrip antenna.

Several antennas with the geometrical configuration proposed in Figure 3.2 were implemented and studied both numerically and experimentally. The effect of the

slot lengths and widths on the size reduction factor, impedance, and radiation characteristics of the antennas has been investigated. Table 3.1 summarizes the results (resonant frequency and directivity) obtained for the three antennas representative of the possible design parameter variations. Specifically, first we consider the effect of reducing the corner slot lengths l_s (Antenna-2) as shown in Figure 3.4 and then the effect of reducing the corner slot widths w_s (Antenna-3) as shown in Figure 3.5 with respect to that of 'Antenna-1', which is used as the benchmark antenna and found to be the antenna with the largest size reduction ratio. For comparison purposes, a reference antenna (a conventional unslotted patch) operating at the same frequency as Antenna-1 was also implemented and its characteristics measured. An HP 8510-B Network Analyzer was utilized for all the measurements.

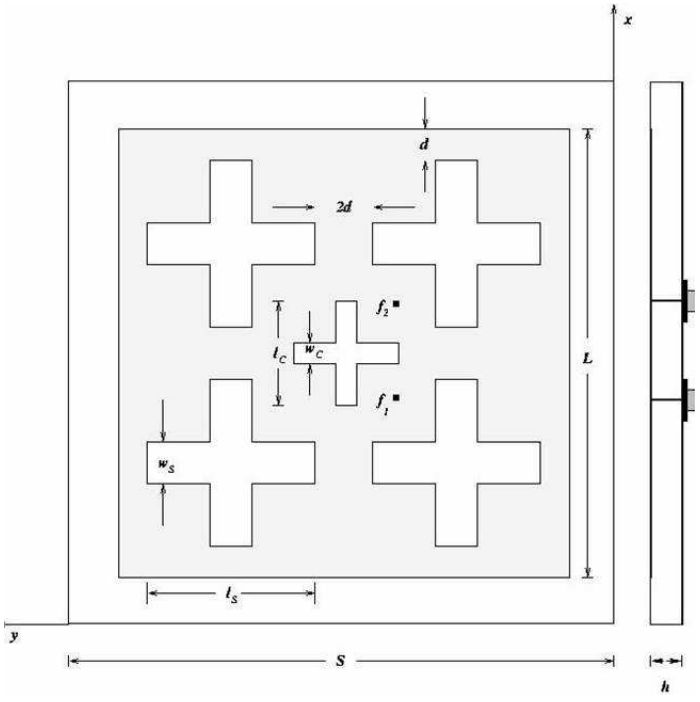

Figure 3.4: Variation in slot parameters : Antenna-2.

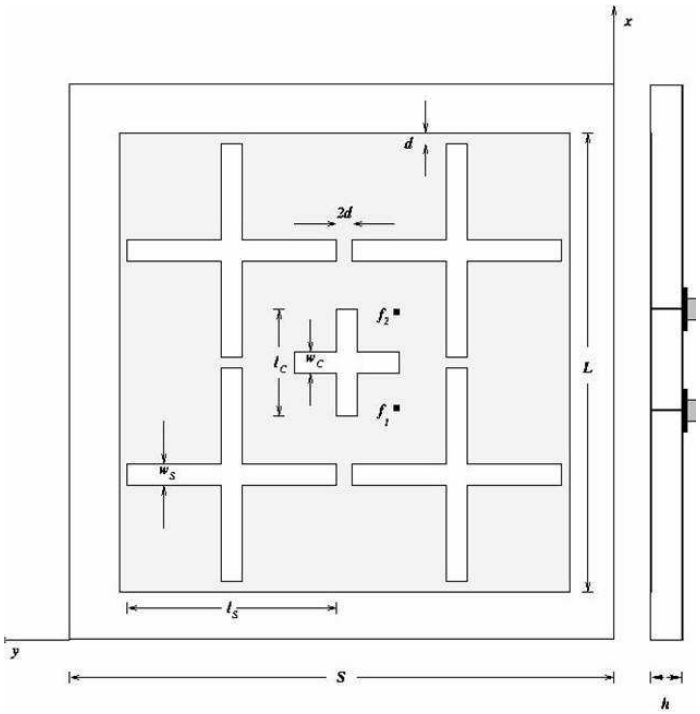

Figure 3.5: Variation in slot parameters : Antenna-3.

3.5.1 Impedance and Isolation Characteristics

Figure 3.6(a) shows the simulated and measured return loss and isolation of Antenna-1. It can be observed that the antenna exhibits excellent impedance matching to 50Ω. Also, isolation greater than 36 dB throughout the operating impedance bandwidth (1:2 VSWR) is observed. The slight discrepancy between numerical and measured return losses (including a 20 MHz resonant frequency shift, which is, however, less than 2.5% shift with respect to the resonant frequency) can be attributed to both fabrication tolerances and FDTD tolerances in the precise modeling of slots and edges as well as the absence of losses in the computer model. For the reference antenna the measured and simulated impedance and isolation characteristics are plotted in Figure 3.6(b). The agreement between measurements and simulation is good. Note that in this case, due to the relatively simple structure, the shift in frequency

between the simulated and measured is less than 3 MHz(less than .5% with respect to the resonant frequency). For the same resonant frequency, the proposed slotted design–Antenna-1 had side dimensions of $L = 67.056$ mm whereas the unslotted patch had the dimensions of $L = 96.770$ mm. Hence, a size reduction of $\sim$51% is achieved with Antenna-1. A comparison of the relative sizes of Antenna-1 and the reference antenna is given in Figure 3.7.

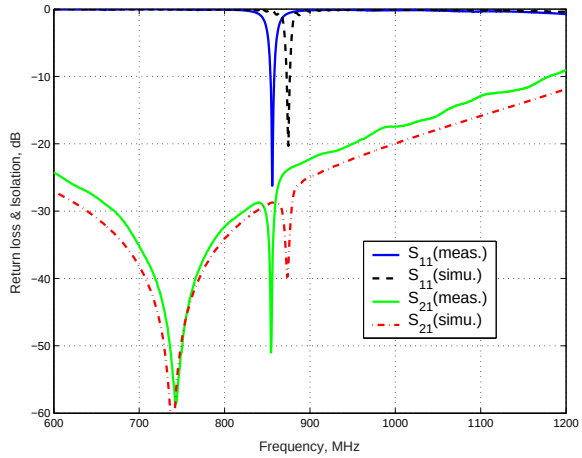

(a)

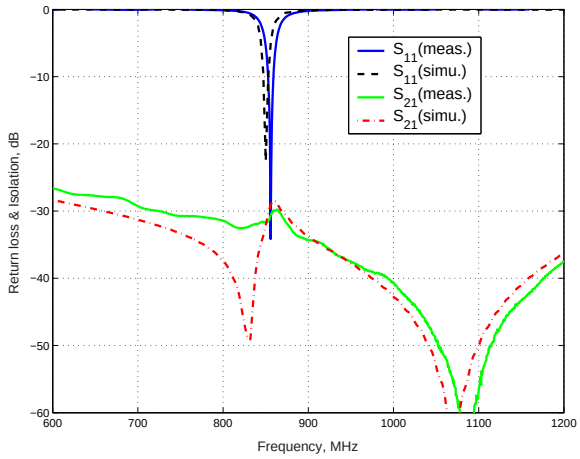

(b)

Figure 3.6: Impedance and Isolation characteristics:(a) Antenna-1; (b) Reference Antenna.

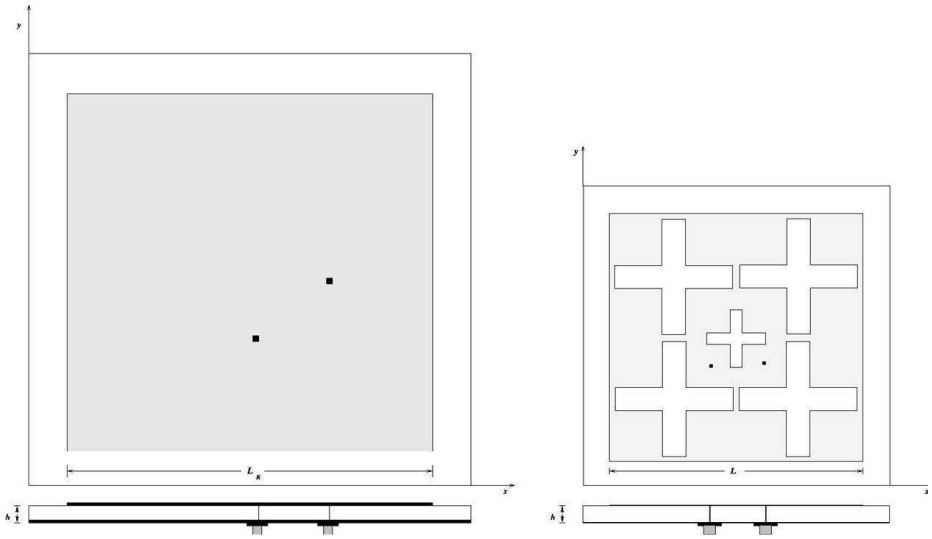

Figure 3.7: Relative sizes of the Reference antenna and the size reduced dual polarized antenna operating at the same frequency.

In Antenna-2, the side dimension was kept the same as Antenna-1 (i.e. $L = 67.056$ mm),while the corner slot lengths l_s were reduced to 25.9 mm. As shown in Table 3.1, this has the effect of increasing the resonant frequency of the patch by approximately 124 MHz. Hence, the size reduction decreased to ∼35% with respect to the reference conventional square patch antenna. To obtain a proper impedance match to 50Ω, the center slot length was reduced to 15.24 mm. In fact, we have observed that a combination of altering the center slot parameters and shifting the feed points along the diagonal can be successfully employed to achieve an excellent 50Ω matching.

In the case of Antenna-3 ($L = 67.056$ mm), the corner slot widths w_s were reduced while keeping their lengths the same as Antenna-1. In this case, too, the resonant frequency of the patch increased as shown in Table 3.1. Thus, the size reduction achieved with Antenna-3 is approximately ∼47%. Figure 3.8 shows the measured and computed return loss for the considered antenna configurations (Antenna-1, Antenna-2, Antenna-3). The largest discrepancy in the simulated and measured resonant frequency for all the three configurations is limited to ∼20 MHz, or less than 2.5% of

the resonant frequency. As expected, from the above results we can conclude that the longer the slots the greater the reduction in size offered. Interestingly, the isolation characteristics do not appear to be significantly affected by the variations in slot parameters.

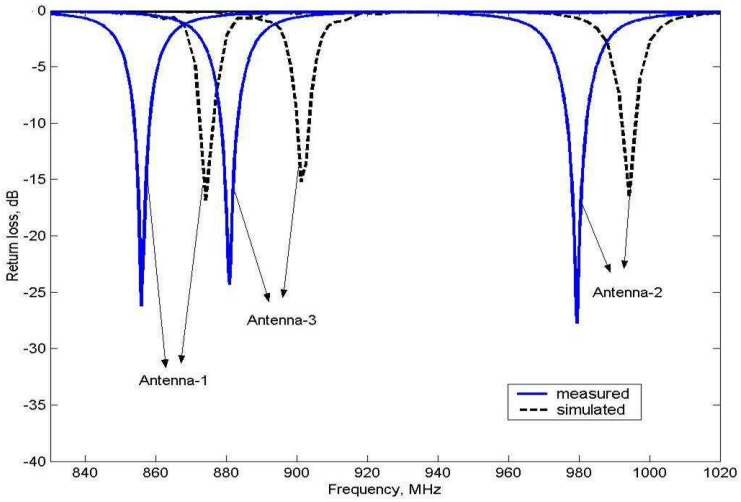

Figure 3.8: Measured and Simulated return losses of Antenna-1,2 and 3.

3.5.2 Radiation Characteristics

The E and the H planes for the proposed antennas (Antenna-1, Antenna-2, Antenna-3) are obtained along the $\pm 45^{\circ}$ planes—along the diagonals of the square patch instead of the conventional x-z and y-z planes as obtained for the reference antenna [91, 92]. While obtaining the radiation patterns in the E and the H planes due to port 1, port 2 was terminated in its resonant impedance and vice versa. Computed radiation patterns in the E and H planes for Antenna-1 and the Reference antenna are plotted in Figures 3.9 and 3.10 respectively. The cross polarization level for Antenna-1 remains below -34 dB in the E plane but in the H plane it deteriorates as we move away from the broadside direction. As expected, a reduction in patch area

results in reduction in directivity of approximately 3.9 dBi. The directivity calculated for Antenna-1 is 0.9 dBi which is 3.9 dBi less than that of the reference antenna.

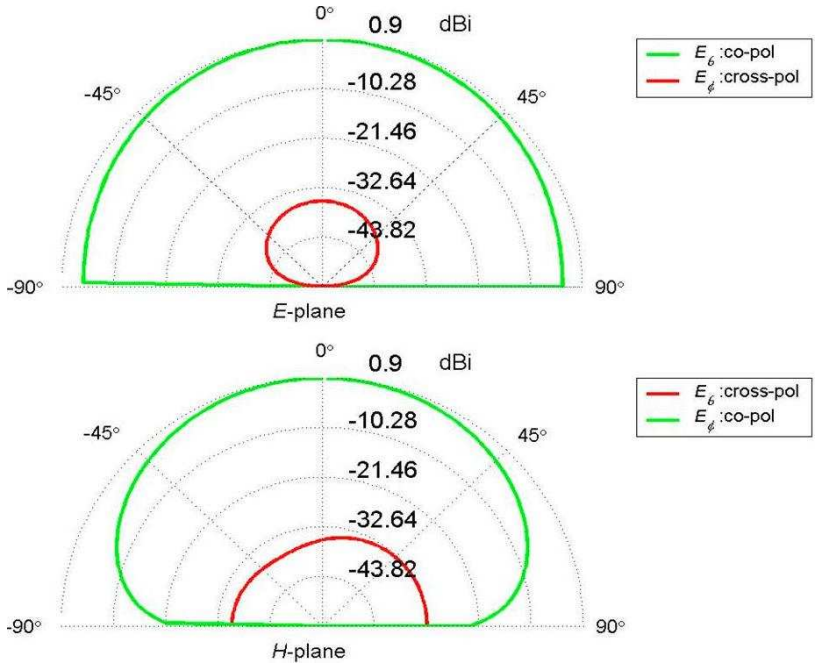

Figure 3.9: Radiation characteristics of Antenna-1.

For Antenna-2 and Antenna-3, the E and H plane radiation patterns are plotted in Figure 3.11 and Figure 3.12. Cross polarization levels less than -32 dB are observed for both of these antennas similar to Antenna-1. Also, due to the fact that lesser patch area is removed in the form of slots from Antenna-2 and Antenna-3 as compared to Antenna-1, a slightly higher directivity is obtained for both of these antennas as seen from Figure 3.11 and Figure 3.12.

3.6 Summary

A novel, compact, dual polarized microstrip patch antenna has been designed and implemented. In the proposed design a size reduction of 51% with a high isolation

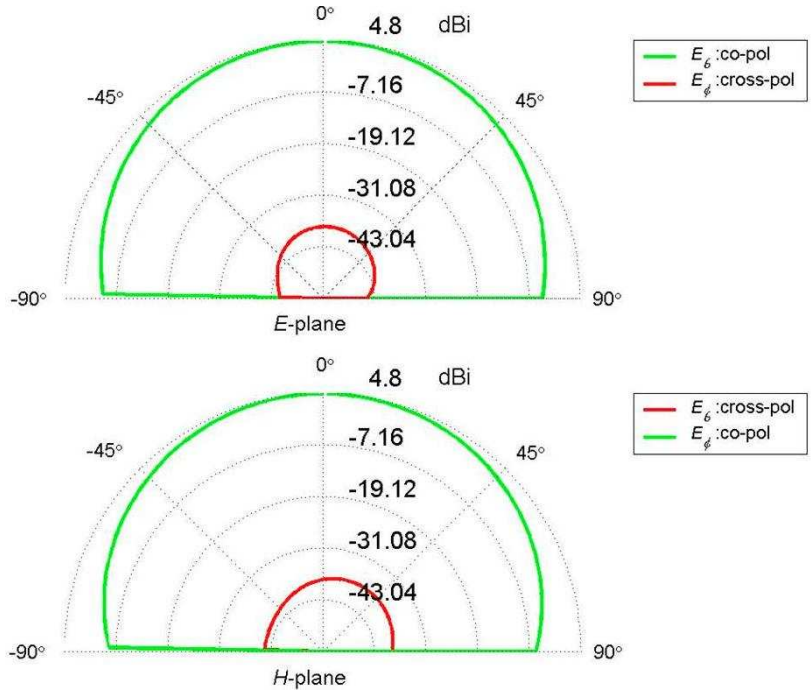

Figure 3.10: Radiation characteristics of the Reference Patch Antenna.

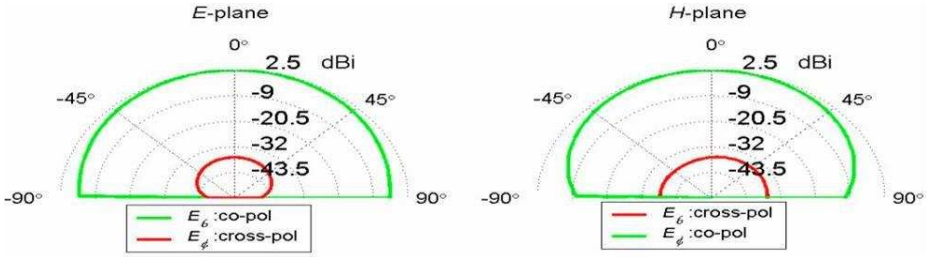

Figure 3.11: Radiation Characteristics of Antenna-2.

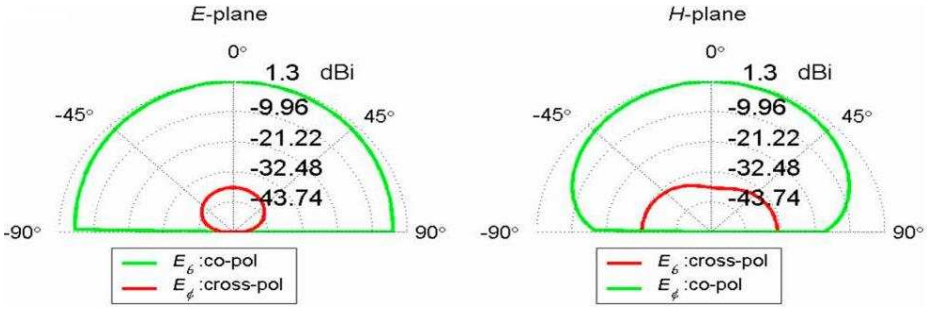

Figure 3.12: Radiation Characteristics of Antenna-3.

(38 dB) and low cross polarization level is demonstrated, albeit, with a reduction in the broadside directivity (by 3.9 dBi). Increasing the size of the slots or incorporating branches to each individual slot so that the symmetry is retained will enable further compactness and matching can be achieved by altering the center slot parameters or the location of the feed point. The influence of the slot parameters was investigated, and a trade-off between slot dimensions, directivity and size reduction factor is shown. Due to their compactness the proposed antennas are suitable for application on mobile wireless nodes operating in dual polarization mode. Four of these antennas were fabricated (identical) and were used in a novel polarization diversity scheme for indoor wireless communication as a part of a research project and the results of the experiments are awaited.

Chapter 4

Investigation of Microwave Data Telemetry links for a Retinal Prosthesis Employing Microstrip Patch Antennas

4.1 Introduction

The motivation and current progress towards a visual prosthesis was outlined comprehensively in 1.2. As is described in chapter 1, an implantable epi-retinal prosthesis can be designed to replace the functionality of the missing photoreceptors

by directly providing electrical stimulation to the next surviving layer of retina (the bipolar and/or ganglion cell layer) thus restoring partial vision.

It must be mentioned that recent work [93] has shown that, in retinas of patients suffering from RP and AMD, along with the loss of photoreceptors there could be a considerable degeneration and reorganization of the retinal structure itself which might impact the artificial stimulation.

The retinal prosthesis system considered here is a dual unit epiretinal device with an extraocular and an implanted intraocular unit as mentioned in 1.2.2. The extraocular unit comprises of the image capturing and processing chips, an amplifier, and the primary coil. The intraocular unit contains the secondary coil, rectifier and signal processing chips, and an electrode array. Conventionally, power and data communication between the external and internal units of such prosthetic devices has been accomplished by a single low frequency (2–10 MHz) inductive link between a pair of coils. In such an approach, the data signal modulates the low frequency power carrier.

However, as was outlined in 1.3, with the advancements in electrode array technology, the bandwidth requirements of future visual prostheses may not be adequately satisfied via inductive coil coupling. In such cases, mutually exclusive power and data transfer can prove useful in providing a solution to transfer power at low frequencies while establishing a high bandwidth data link at microwave frequencies. Data communication at microwave frequencies (1–3 GHz) using a pair of external and internal microstrip patch antennas can provide higher bandwidth and is a viable alternative as computationally demonstrated in [94].

We investigate here this novel approach of establishing the data telemetry link for a dual unit retinal prosthesis at microwave frequencies (1.45 GHz and 2.45 GHz) using a pair of microstrip patch antennas. Appropriately sized extraocular (25×25 mm)

and intraocular (6×6 mm) antennas are designed to operate at both the frequencies using the Finite Difference Time Domain (FDTD) method, and the coupling between them is examined computationally in the presence of a 0.25 mm resolution human head model. The numerically designed antennas are then implemented and it is observed that numerical and experimental coupling results agree well. The influence of the head and eye on the coupling between the antennas is characterized and it is observed that the eye and head tissues act as a dielectric lens and improve the coupling performance.

Computationally, the data link is characterized for a maximum transmitted power of 50 mW. Considering the worse case coupling efficiency between the antennas (-45 dB at 1.45 GHz), and the extremely sensitive RF front end receivers available (-50 dBm and higher), the extraocular antenna is not expected to transmit more than 50 mW. Hence, the Specific Absorption Rate (SAR) computations are performed for a radiated power of 50 mW in both the frequency bands. The evaluated SAR values are within the safety limits specified in the IEEE/ANSI standard [47].

This chapter is organized in the following manner: Section 4.2 describes the antenna design and implementation issues in both frequency bands. A brief description of the head model used and the computational method and domain employed is provided in section 4.3. The set up for experimental measurements is described in section 4.4. The influence of the eye model on the antenna characteristics and the corrective measures employed are discussed in section 4.5. Section 4.6 characterizes the data telemetry link at both the frequency bands and 4.7 presents SAR computations at both frequency bands.

4.2 Antenna Design

Owing to the nature of the application, the transmitting and receiving antennas must be very compact, robust and lightweight. Thus as discussed in 2.3, microstrip patch antennas were selected. The extraocular antenna was designed to have dimensions within 25 × 25 mm to fit on a pair of glasses to be worn by the patient. It is anticipated that the extraocular unit comprising of the camera, primary coil and data processing circuitry will be mounted on this custom designed pair of glasses.

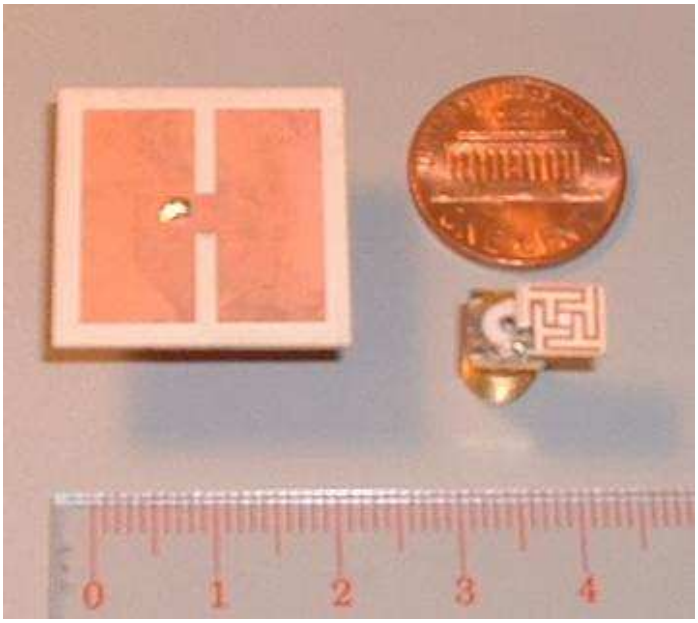

Figure 4.1: Implemented Extraocular and Intraocular patch antennas designed to operate at 1.45 GHz.

The intraocular antenna was to be designed with dimensions less than 6 × 6 mm to accommodate it within the ciliary muscles of the eye (held by the zonules in place of the lens)—about 6–7 mm posterior to the cornea (the lens is removed from the eyeballs of these patients and in the current design, it is proposed that the intraocular unit gets positioned in place of the lens). At both the frequency bands, a pair of extraocular and intraocular antennas were designed within the above stated dimensions using

an in house FDTD code. For this work, all the antennas are designed with a high dielectric constant of $\varepsilon_r = 9.2$ and the thickness of $h = 0.5$ mm.

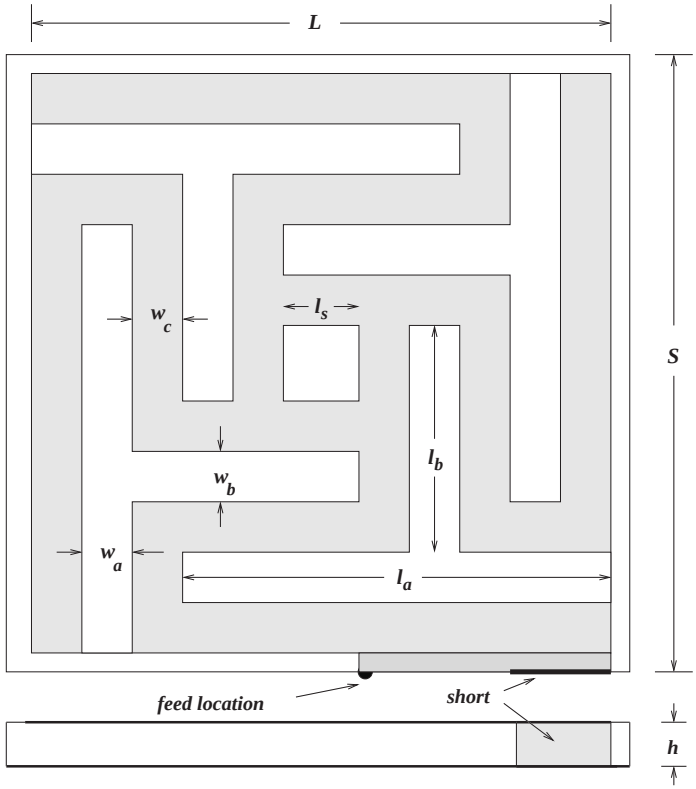

Figure 4.2: Intraocular antenna configuration and design parameters designed to operate at 1.45 GHz.

4.2.1 Frequency band at 1.45 GHz

Several size reduction techniques – as outlined comprehensively in 2.3.1.3 were employed to design the compact extraocular and intraocular antennas. The extraocular antenna was designed by incorporating a pair of vertical slots along the non radiating edges of the antenna. By varying the length of the slots, the desired compactness was achieved and the antenna dimensions were restricted to $25 \times 25 \times 0.5$ mm. For the intraocular antenna, to facilitate its embedding in the eye ball, it was essential to

restrict its size approximately to within $6 \times 6 \times 0.5$ mm. A symmetric array of slots were etched out from the surface and a single shorting post was used near the feed point to resonate and match the extremely compact intraocular antenna. The implemented extraocular and intraocular antennas are shown in Figure 4.1 while Figure 4.2 details the design parameters for the intraocular antenna.

4.2.2 Frequency band at 2.45 GHz

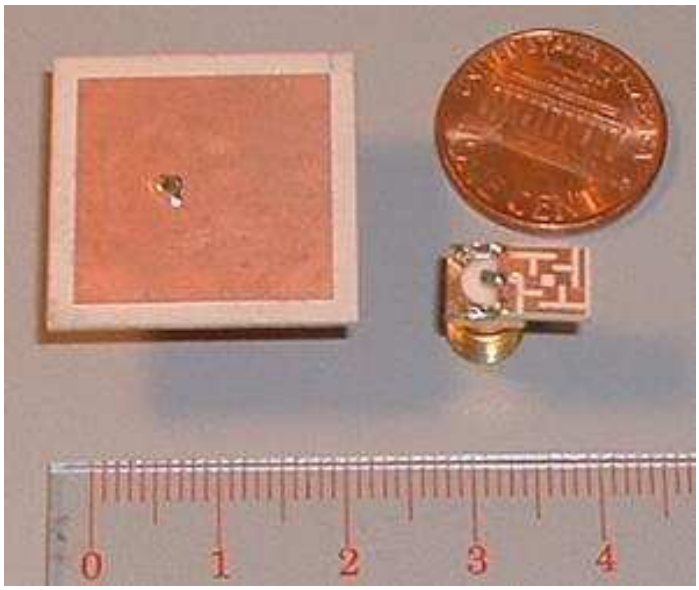

Figure 4.3: Implemented Extraocular and Intraocular patch antennas designed to operate at 2.45 GHz.

For the same dimensions of the extraocular and intraocular antennas, the degree of compactness required at 2.45 GHz is less than that required at 1.45 GHz. Thus, with dimensions of $25 \times 25 \times 0.5$ mm, a simple patch antenna was designed to operate as the extraocular antenna at 2.45 GHz. The array of slots used on the 2.45 GHz intraocular antenna was identical to that of the 1.45 GHz intraocular antenna but since the required compactness was lower, the length of the slots was reduced for the 2.45 GHz intraocular antenna. Also, two shorting posts were introduced symmetrically

with respect to the feed location to achieve matching for the 2.45 GHz intraocular antenna. Figure 4.3 shows the picture of implemented extraocular and intraocular antennas in this frequency band. Figure 4.4 shows the design parameters for the intraocular antenna.

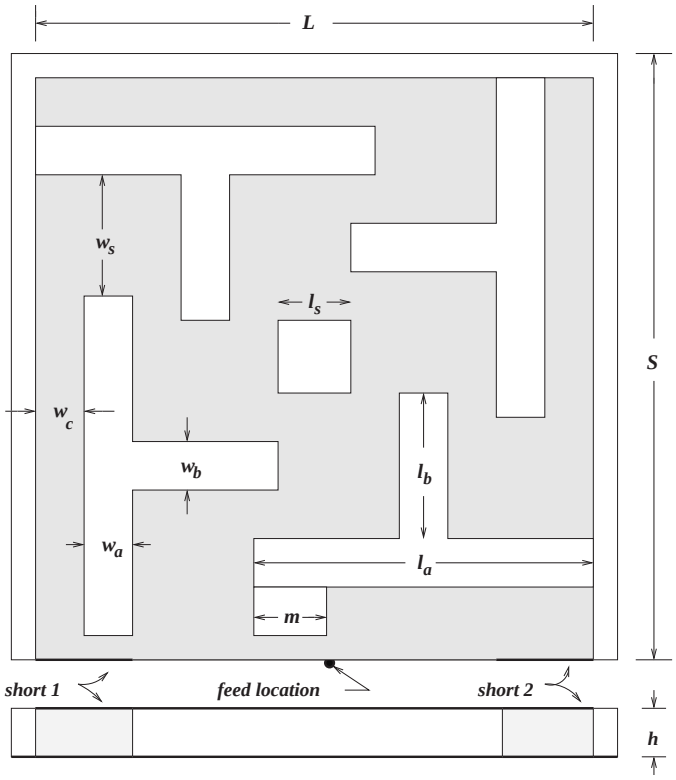

Figure 4.4: Intraocular antenna configuration and design parameters designed to operate at 2.45 GHz.

The parameter specifics for Figures 4.2 and 4.4 are listed in Table 4.1. As seen from Figures 4.2 and 4.4, the proposed designs facilitated slight variations in the width of the shorting post/s and in the length of slots.

Such modifications had to be incorporated at both frequency bands (both in FDTD simulations as well as after implementation) to match the intraocular antenna's resonance frequency to that of the extraocular antenna. Also, due to tolerances involved during actual fabrication, the realized antennas resonated at 1.4 GHz and 2.37 GHz

Table 4.1: Parameters defined in Figures 4.2 and 4.4 for the proposed intraocular antenna design at both the frequency bands (All dimensions in mm).

Intraocular antenna	S	L	l_a	l_b	l_s	w_a	w_b	w_c	w_s	m
1.45 GHz	6.25	5.75	4.25	2.25	0.75	0.5	0.5	0.5	–	–
2.45 Ghz	6.25	5.75	3.5	1.5	0.75	0.5	0.5	0.5	1.25	0.75

instead of the computationally designed 1.45 GHz and 2.45 GHz respectively. Hence, to maintain consistency of notation the antennas will be referred to belong to the corresponding 1.45 GHz band or the 2.45 GHz band and it should be understood that for the shown experimental results, the implemented antennas actually operated at 1.4 GHz and 2.37 GHz.

4.3 Human Head Model and FDTD Modelling

The data for the head model was obtained in the form of cross sectional slices of 1 mm resolution from the National Library of Medicine (NLM) "Visible Man Project" [95]. In this application, since it was essential to represent the tissues of the eye and head with a high degree of detail, the head model was discretized further—to reach a spatial resolution of 0.25 mm (64 times the original one) using a method of interpolation in all three dimensions [46]. The detailed features of the eye were represented as described in [96] and the dielectric properties of the body tissues at the frequencies of 1.45 GHz and 2.45 GHz were obtained from the online database compiled by C. Gabriel [97].

The dielectric properties of those tissues not explicitly available from the online database were obtained as mentioned in [96]. For the coupling performance and SAR computations, a portion of this head model was extracted and used in the computational domain as shown in Figure 4.5. A 3-dimensional D-H formulation of the FDTD method [52] has been employed with a uniform cell grid of 0.25 mm

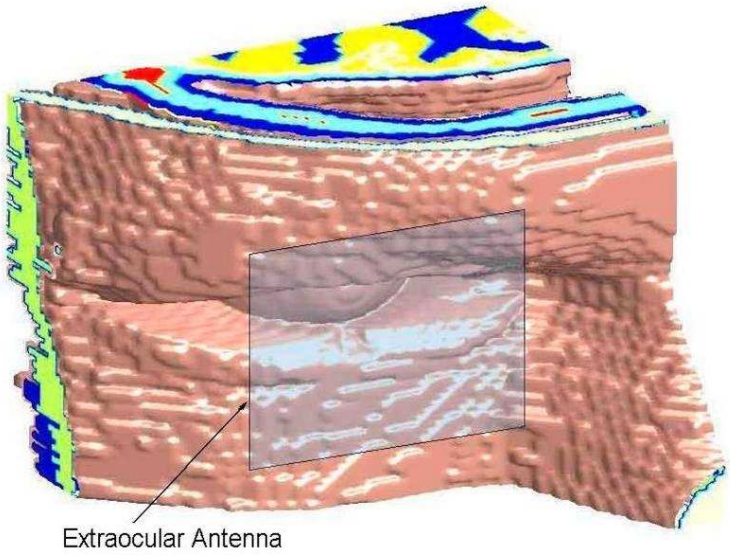

Figure 4.5: 3-D rendering of the portion of the head model used in the FDTD computational domain.

resolution to compute the performance of the data telemetry link in the presence of the head model. A material independent Perfectly Matched Layer (PML) is used as an absorbing boundary condition so that the model can be immersed in the PML layers as mentioned in [90]. The lens of the eye is removed from the head model (to be consistent with the actual intended surgical procedure) and the intraocular antenna is encapsulated with a thin 1 mm thick insulating layer and embedded in its place as shown in the cross sectional Figure 4.6. The extraocular antenna is modelled corresponding to its position on a pair of glasses at a distance of approximately 25 mm from the intraocular embedded antenna. At both the frequency bands, FDTD computations were performed to determine the coupling between the extraocular and implanted antennas in these positions. SAR computations were also carried out within the same computational model at 1.45 GHz and 2.45 GHz to determine the extent of power deposition in the head and eye tissues due to operation of the data telemetry link.

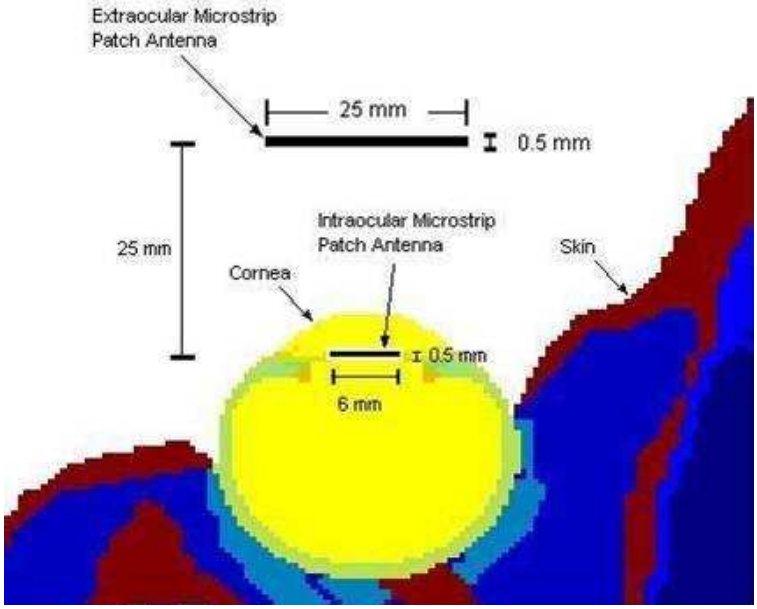

Figure 4.6: Horizontal cross sectional slice of the head model through the center of the eyeball depicting the relative locations of the Extraocular and intraocular antennas.

4.4 Experimental Setup

For coupling measurements in free space, both the antennas were fixed on a pair of clamps and were connected to an HP 8510C Network Analyzer. The extraocular and intraocular antennas were oriented on the same axis facing each other in their broadside direction. Coupling measurements as a function of free space separation and angular separation were performed in both frequency bands at 1.45 GHz and 2.45 GHz. The effect of misalignment on the coupling performance of the link was also investigated. To this objective, the distance of separation between the antennas was maintained constant (at approximately 25 mm) and a set of coupling measurements were taken as a function of the angular separation between the two antennas. At each frequency band (1.45 GHz and 2.45 GHz) two cases were considered for the coupling measurements. In the first case, the extraocular antenna was rotated along a path

which was symmetrical about the shorting post of the intraocular antenna as depicted in Figure 4.7, while in the second case the rotational path was asymmetrical to the shorting post of the intraocular antenna as depicted in Figure 4.8.

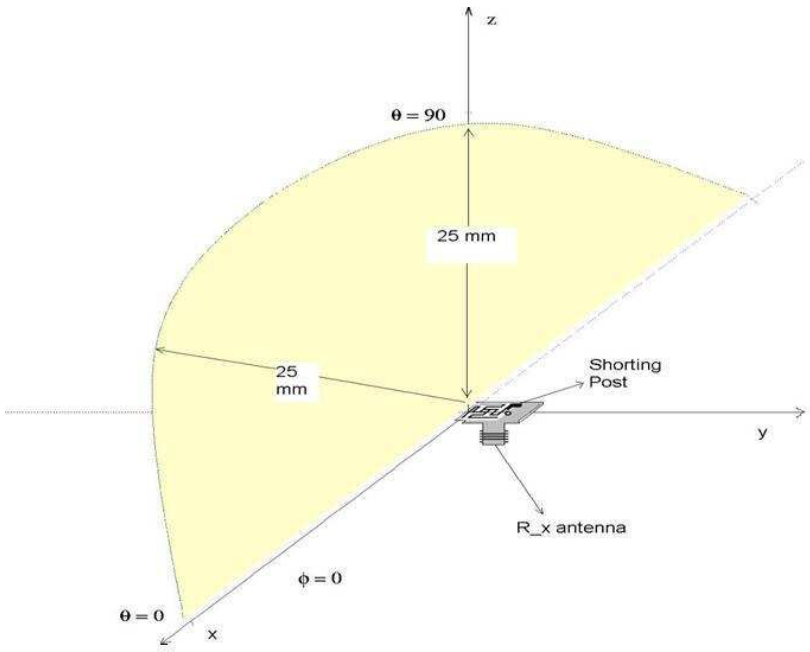

Figure 4.7: Symmetric rotation of the extraocular antenna with respect to the shorting pin of intraocular antenna (at a fixed separation of 25 mm).

To assess the performance of the data telemetry link in presence of the eyeball (with the intraocular antenna immersed in the eyeball), an eye phantom was realized by a thin plastic sphere filled with a liquid simulating the properties of the vitreous humor. To simulate the electrical properties of vitreous humor, a fluid with a composition of water and appropriate proportions of sugar and salt was developed. Two different vitreous humor simulant fluids were developed to closely simulate the electrical properties (dielectric constant and conductivity) of vitreous humor at 1.45 GHz and 2.45 GHz [97]. The electrical properties of the fluid were determined by using a coaxial probe and a technique described in [98].

To ensure stable position during measurements, this eye phantom was snugly

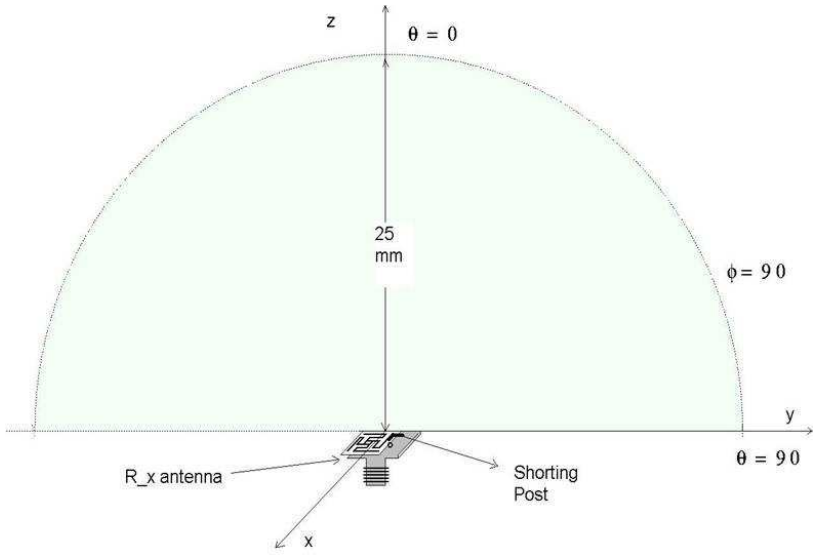

Figure 4.8: Asymmetric rotation of the extraocular antenna with respect to the shorting pin of intraocular antenna (at a fixed separation of 25 mm).

fit into a circular hole cut out of a square styrofoam sheet. A slice was removed from the top of the eye phantom to make the right sized opening for immersing the encapsulated intraocular antenna. To prevent any contact with the fluid vitreous humor simulant in the eyeball, the intraocular antenna (along with the coaxial cable connecting it) was encapsulated in a thick plastic sheath. The extraocular and the intraocular antennas were fixed on two supports and clamped on a vertical scaled bar. The encapsulated antenna was immersed into the eye phantom to the approximate depth required. With this setup, coupling measurements were taken as a function of separation between the extraocular and intraocular antennas. (in the computations, the intraocular antenna was embedded at a depth of 6–7 mm from the tip of the eyeball but during the experimental set up, difficulty in determining the immersed depth caused an uncertainty of 1–2 mm in the position of the immersed intraocular antenna).

4.5 Influence of the Eyeball on Intraocular Antenna Characteristics

When the encapsulated intraocular antenna is immersed in the eye phantom filled with humor simulant fluid, due to the dielectric loading effect, the antenna is detuned [99]. The resonant frequency gets lowered and the return loss degrades due to an inductive effect in its impedance characteristics. The dielectric loading effect is more pronounced at the higher frequency band of 2.45 GHz. This phenomenon is depicted in Figure 4.9.

Thus, for experimental measurements in presence of the model, a new set of intraocular antennas had to be implemented accounting for the inductive loading effect due to immersion in the eye phantom. The new intraocular antennas were designed so that they exhibit capacitive behavior at the desired extraocular antenna frequency in free space. To this end, the intraocular antennas as shown in Figure 4.2 and Figure 4.4, were modified by altering the widths of the shorting posts to make them capacitive in free space. This ensured that when these modified intraocular antennas were immersed in the eye phantom, the inductive dielectric loading influence would re-tune them (resonant with good impedance matching) to the desired frequency of the extraocular antenna. Henceforth, these modified intraocular antennas are termed as re-designed intraocular antennas. Currently, at both the frequency bands this new design has been accomplished by a tedious trial and error procedure due to lack of adequate data (specifying the amount of dielectric loading) for such novel applications.

Figure 4.10(a) and Figure 4.10(b) show the impedance characteristics of the re-designed intraocular antenna (in free space and after immersing in the eye phantom) and that of the transmitting antenna in the 1.45 GHz band. It is shown that in free

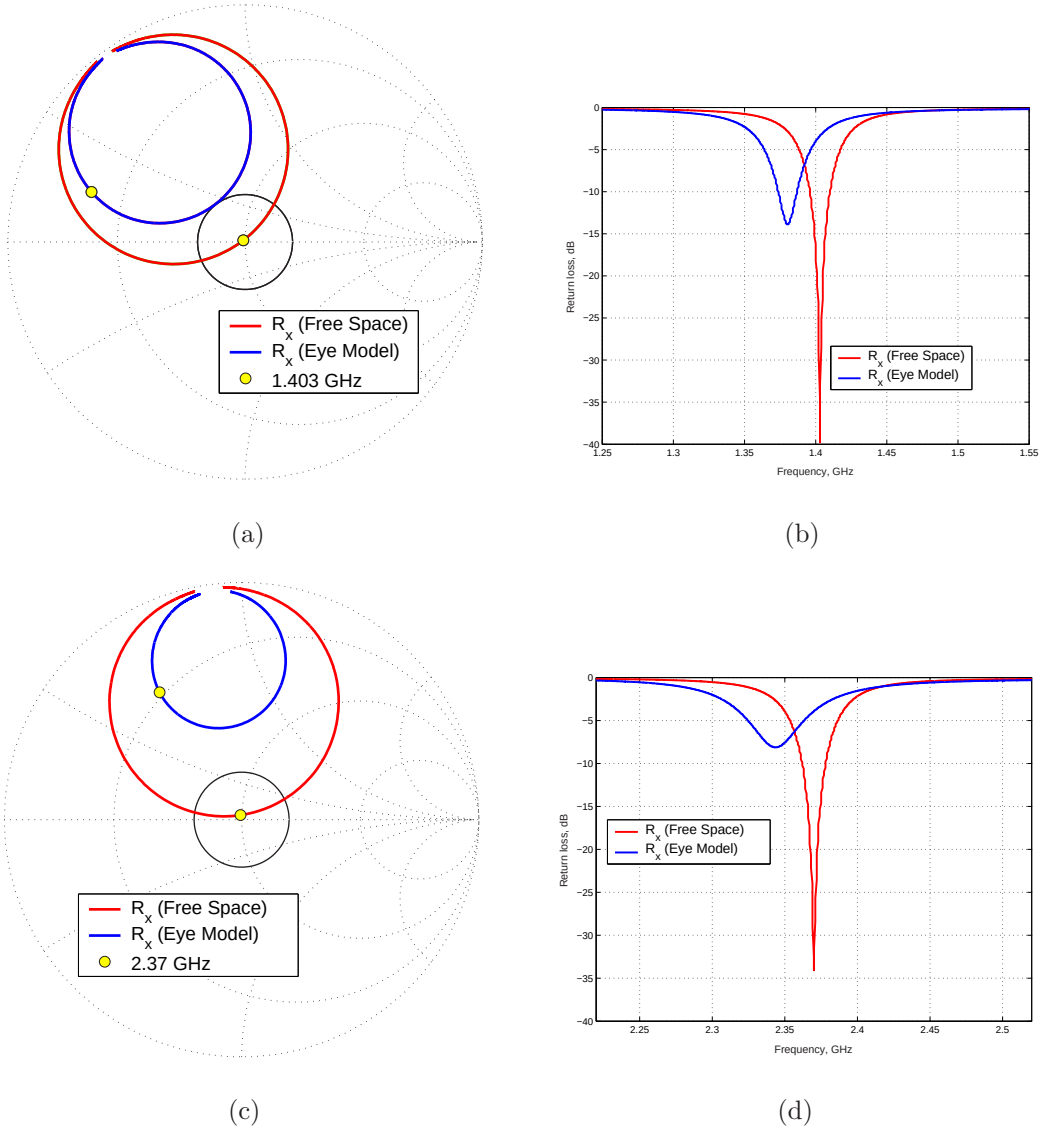

Figure 4.9: Inductive (dielectric) loading influence of the vitreous humor simulant fluid of the eye model on the intraocular antenna (encapsulated in a plastic sheath) and immersed to the appropriate depth in the model:
(a) Smith chart characteristics in the 1.45 GHz band;
(b) Return loss characteristics in the 1.45 GHz band;
(c) Smith chart characteristics in the 2.45 GHz band;
(d) Return loss characteristics in the 2.45 GHz band.

space there is an offset of 15 MHz between the resonant frequencies of the re-designed intraocular antenna and the transmitting antenna. However, when the re-designed intraocular antenna is immersed in the eye phantom, its resonant frequency matches that of the transmitting antenna at 1.4 GHz.

Similarly, Figure 4.10(c) and Figure 4.10(d) show the impedance characteristics for the intraocular antenna in the 2.45 GHz band. In this case, due to the pronounced effect of dielectric loading, the intraocular antenna was re-designed to exhibit substantial capacitive behavior in free space so that the inductive influence when immersed in the eye phantom leads to a good matching at the desired extraocular antenna frequency.

4.6 Coupling between the Antennas of the Data Telemetry Link

Numerically, due to the length of the simulations, coupling was computed only for a fixed separation of 25 mm between the extraocular and intraocular antennas. These computations were performed at both the frequency bands in free space as well as in the presence of the eye model. Experimentally, both in free space and in the presence of the eye model, coupling was observed as a function of broadside separation between the two antennas at both the frequency bands. Measurements with respect to angular separation (to determine effect of misalignment) were obtained only in free space. Numerical and experimental coupling results were compared for the separation of 25 mm between the two antennas in free space and in the presence of the eye model.

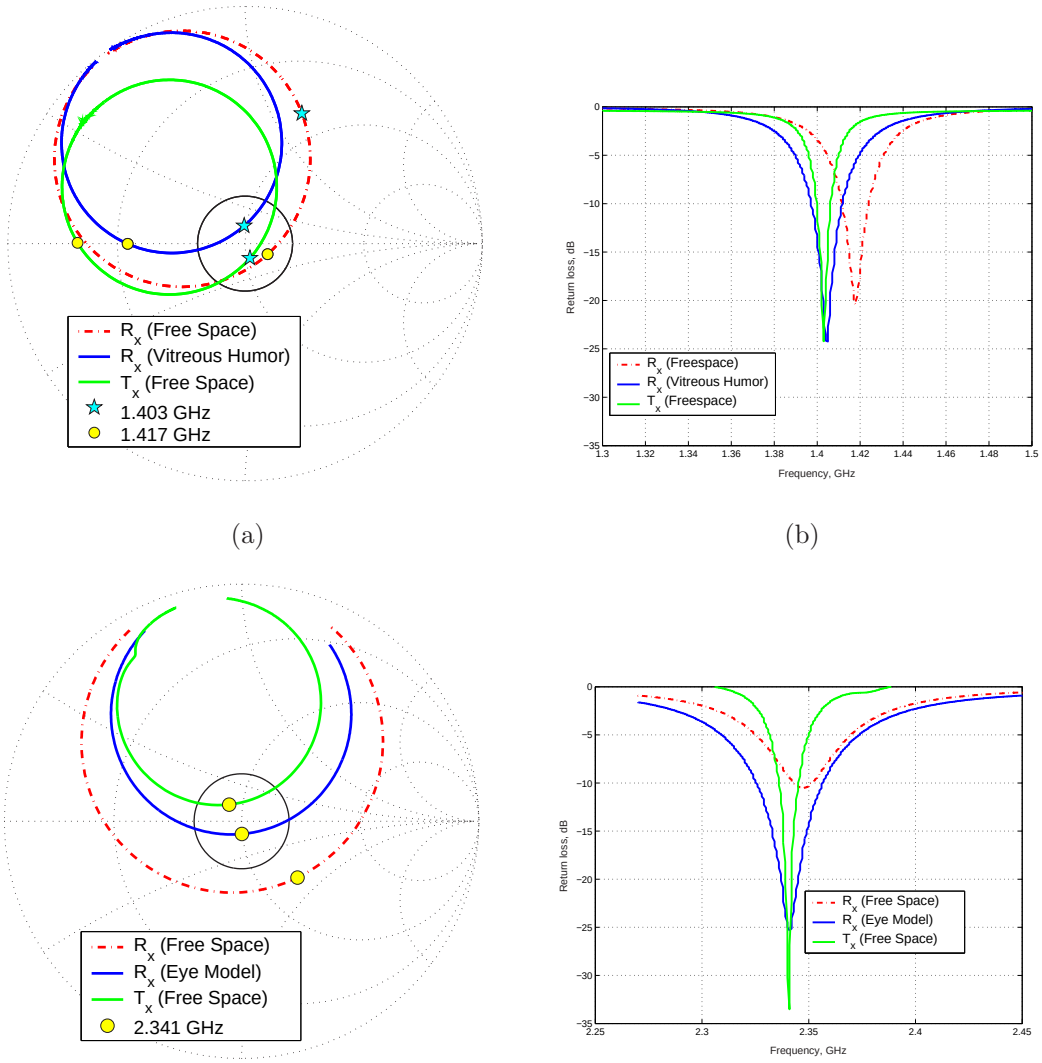

Figure 4.10: Experimental measurements showing the influence of the eye model on the impedance characteristics of the intraocular antenna; While the re-designed intraocular antenna is de-tuned in free space, it resonates at the same frequency of the transmitting antenna when immersed in the eye model:
(a) Smith chart characteristics in the 1.45 GHz band;
(b) Return loss characteristics in the 1.45 GHz band;
(c) Smith chart characteristics in the 2.45 GHz band;
(d) Return loss characteristics in the 2.45 GHz band.

4.6.1 Performance of the data telemetry link at 1.45 GHz

In the 1.45 GHz frequency band, at a separation of 25 mm in free space, the numerically computed coupling was −41.5 dB and the experimentally observed value was −42.5 dB. When the intraocular antenna was embedded in the eye model, numerically computed coupling increased to −34.6 dB while experimentally, the measured coupling was −37.2 dB. Numerical and experimental results are in close agreement as depicted in Figure 4.11 and the increase in coupling in the presence of the eye model suggests that the eye ball acts as a dielectric lens for the intraocular antenna and actually improves the coupling performance (the discrepancy in the computational and experimental frequency of operation is explained in 4.2).

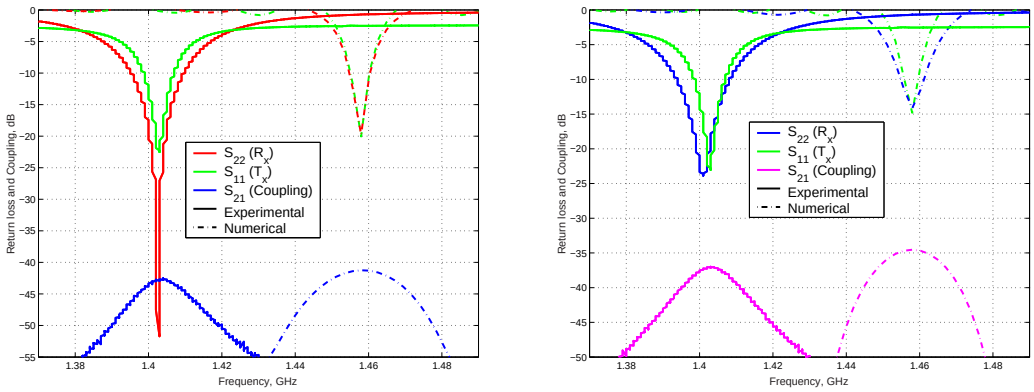

(a) (b)

Figure 4.11: Comparison between the experimentally (strong lines) and numerically (dotted lines) observed coupling values at a separation of 25 mm at 1.45 GHz:
(a) In Free Space;
(b) In the presence of the Eye Model (intraocular antenna immersed inside the eye model).

4.6.2 Performance of the data telemetry link at 2.45 GHz

In the 2.45 GHz band, again at a separation of 25 mm between the antennas, in free space the numerically computed coupling was −28.9 dB and experimentally it was observed to be −32.0 dB. In the presence of the eye model, there was a slight increase in coupling. Numerically, it increased to −27.4 dB while the experimentally measured value was −31.1 dB. It is seen that due to the dielectric lens effect of the eye ball, coupling at 1.45 GHz improved significantly by 4–6 dB while at 2.45 GHz, the improvement was less, around 1–2 dB. Also, it is observed that at a separation of 25 mm, coupling at 1.45 GHz is lower than that at 2.45 GHz. This may be attributed to the fact that for the same sized antennas, at 1.45 GHz the greater compactness deteriorates the antenna efficiency, thus degrading the coupling performance. Figure 4.12 depicts the coupling performance (both experimental and computational) in the 2.45 GHz frequency band.

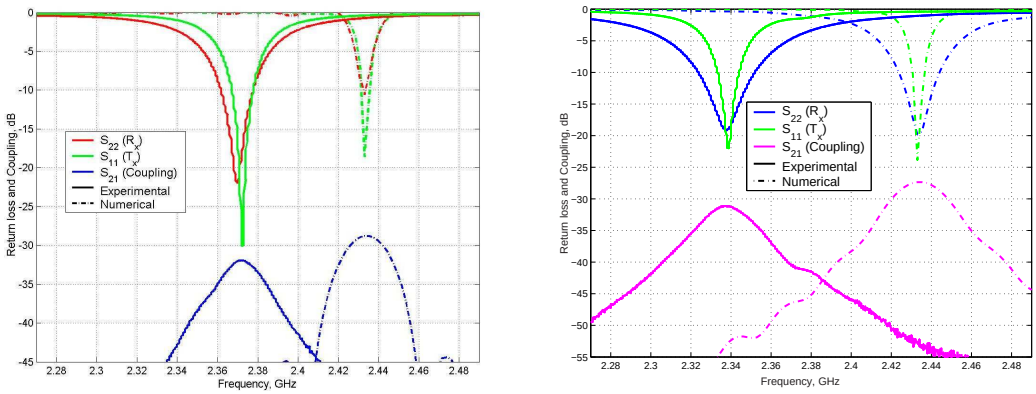

(a) (b)

Figure 4.12: Comparison between the experimentally (strong lines) and numerically (dotted lines) observed coupling values at a separation of 25 mm at 2.45 GHz :
(a) In Free Space;
(b) In the presence of the Eye Model (intraocular antenna immersed inside the eye model).

Table 4.2: Coupling performance at a separation of 25 mm at both frequency bands (1.45 and 2.45 GHz).

Frequency band	Free Space (dB)		Eye Phantom (dB)	
	Num.	Exp.	Num.	Exp.
1.45 GHz	−41.5	−42.5	−34.6	−37.2
2.45 GHz	−28.9	−32.0	−27.4	−31.1

4.6.3 Comparison of coupling performance at both the frequency bands

The coupling performance at 25 mm separation is summarized in Table 4.2.

Figures 4.13(a) and 4.13(b) compare the coupling performance at both the frequency bands at a separation of 25 mm in free space and in the presence of the eye model.

Numerically as well as experimentally, an improvement in coupling is observed (4–6 dB at 1.45 GHz and 1–2 dB at 2.45 GHz) when the intraocular antenna is immersed in the eye model. The discrepancy between the numerical and experimental frequencies of operation is due to the fact that the implemented antennas (for experimental results) operated at a lower frequency (as explained earlier in 4.2). Besides this, as seen in Figure 4.13(b) there is also a slight discrepancy between the experimentally obtained curves for free space and in the presence of the eye model. This is due to the fact that for measurements in the presence of the eye model, the antennas were re-designed (as explained in 4.5), and on implementation, operated at a lower frequency than those in free space.

Figures 4.14(a) and 4.14(b) compare the experimentally observed coupling as a function of the distance of separation both in free space as well as in the presence of the eye model at 1.45 GHz and 2.45 GHz respectively. At 1.45 GHz, for all distances of separation examined, observed coupling with the intraocular antenna embedded in

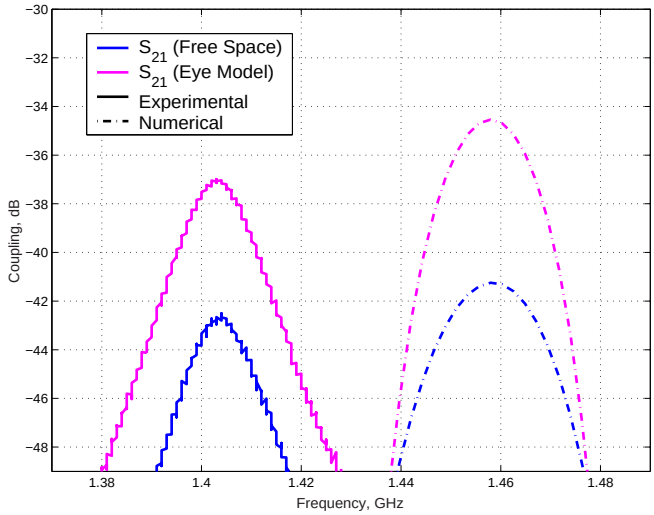

(a)

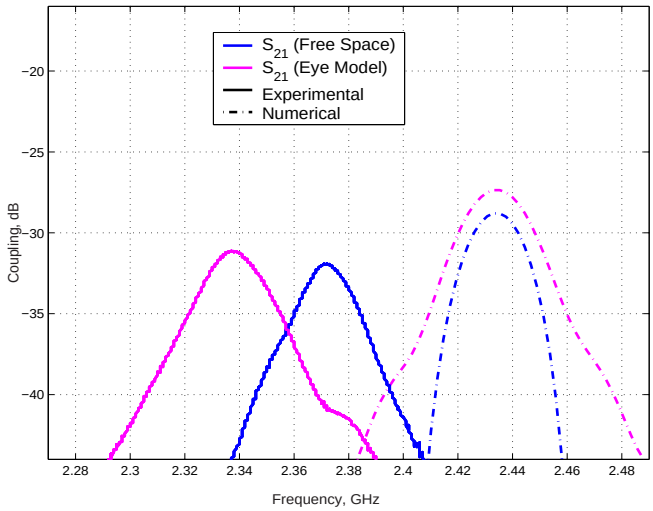

(b)

Figure 4.13: Improvement in coupling performance at 25 mm separation (experimental and numerical) in the presence of the eye model: (a) 1.45 GHz; (b) 2.45 GHz.

the eye model is higher than that in free space, while at 2.45 GHz, for separation less than 26 mm, coupling in the presence of the eye model is higher but it falls below the corresponding free space values beyond 26 mm.

Figures 4.15(a) and 4.15(b) show measured coupling as a function of angular orien-

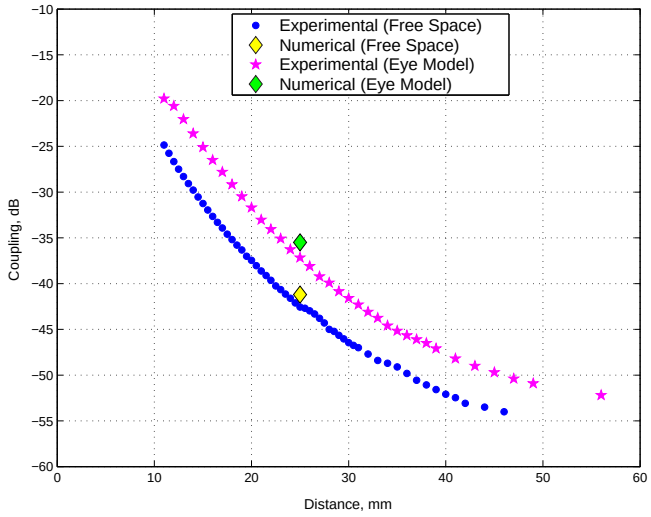

(a)

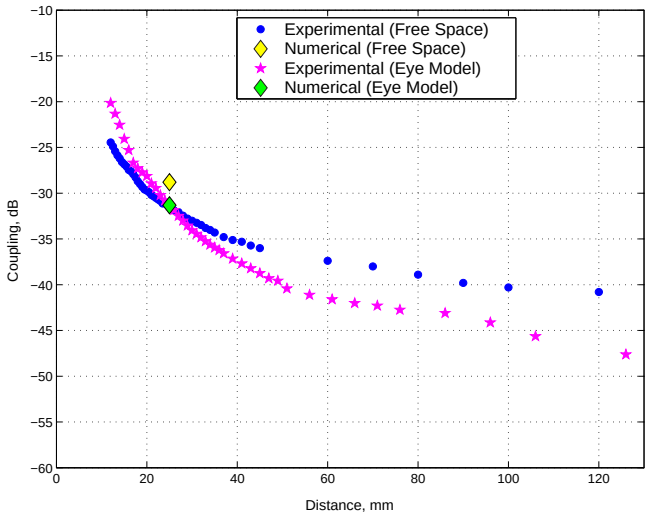

(b)

Figure 4.14: Comparison of coupling in free space and in presence of the eye model as a function of separation: (a) 1.45 GHz; (b) 2.45 GHz.

tation in free space between the two antennas for 1.45 GHz and 2.45 GHz respectively. At both frequency bands, when the extraocular antenna is rotated symmetrically with respect to the shorting post of the intraocular antenna (shown as the $\phi = 0°$ case), the coupling is maximum at broadside and symmetric on either side of the broadside

direction. For asymmetric rotation (shown as the $\phi = 90°$ case), coupling improves away from the broadside direction thus indicating that with a particular orientation of the antennas, the wireless link can be made quite robust to misalignment.

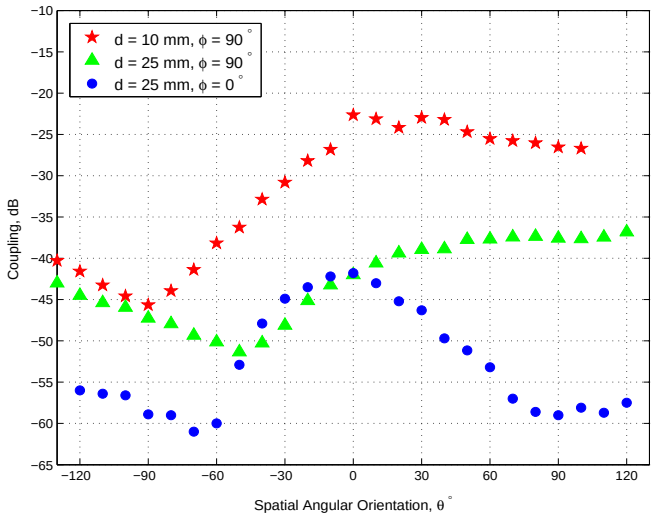

(a)

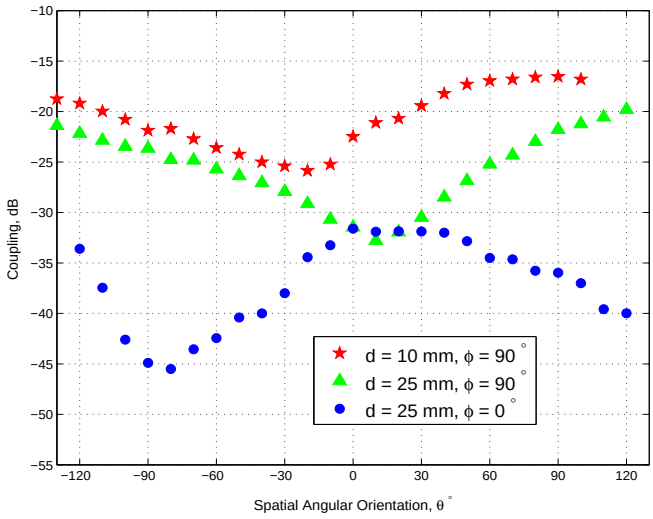

(b)

Figure 4.15: Coupling as a function of angular separation at a fixed distance of 25 mm (for symmetrical and asymmetrical rotation of extraocular antenna with respect to the shorting post of intraocular antenna: (a) 1.45 GHz; (b) 2.45 GHz.

We observed as expected, that the coupling is very sensitive to the intraocular antenna's depth of immersion in the eye model. Moreover, the intraocular antenna (which has been re-designed to account for the dielectric influence) operates with good impedance characteristics for only a specific range of depth of immersion (for experimental measurements), and therefore its positioning at the proper depth in the eye model was essential to ensure good matching at the desired frequency.

4.7 SAR computations

Electromagnetic energy gets deposited in the eye and surrounding head tissues due to the operation of the wireless data telemetry link. Computations to quantify the power deposited in terms of Specific Absorption Rate (SAR) were performed at both the frequency bands. Due to the sensitivity of receiver architectures that can be employed (to further process the received signal from the intraocular antenna), the transmitter antenna is not expected to radiate more than 50 mW. Hence, the SAR values were normalized to a maximum transmitted power of 50 mW. Peak 1-g SAR values were calculated at both the frequency bands to determine compliance with the IEEE/ANSI stipulated guidelines.

Figure 4.16 depicts the 1-voxel and 1-g SAR profiles in a horizontal and vertical cross sections taken through the head model for an operating frequency of 1.45 GHz (the electromagnetic energy deposition was computed after 101 cycles of transmitted signal for this study).

Similarly, Figure 4.17 depicts the 1-voxel and 1-g SAR profiles in a horizontal and vertical cross sections taken through the head model for an operating frequency of 2.45 GHz (for this frequency too, the electromagnetic energy deposition was computed after 101 cycles of transmitted signal).

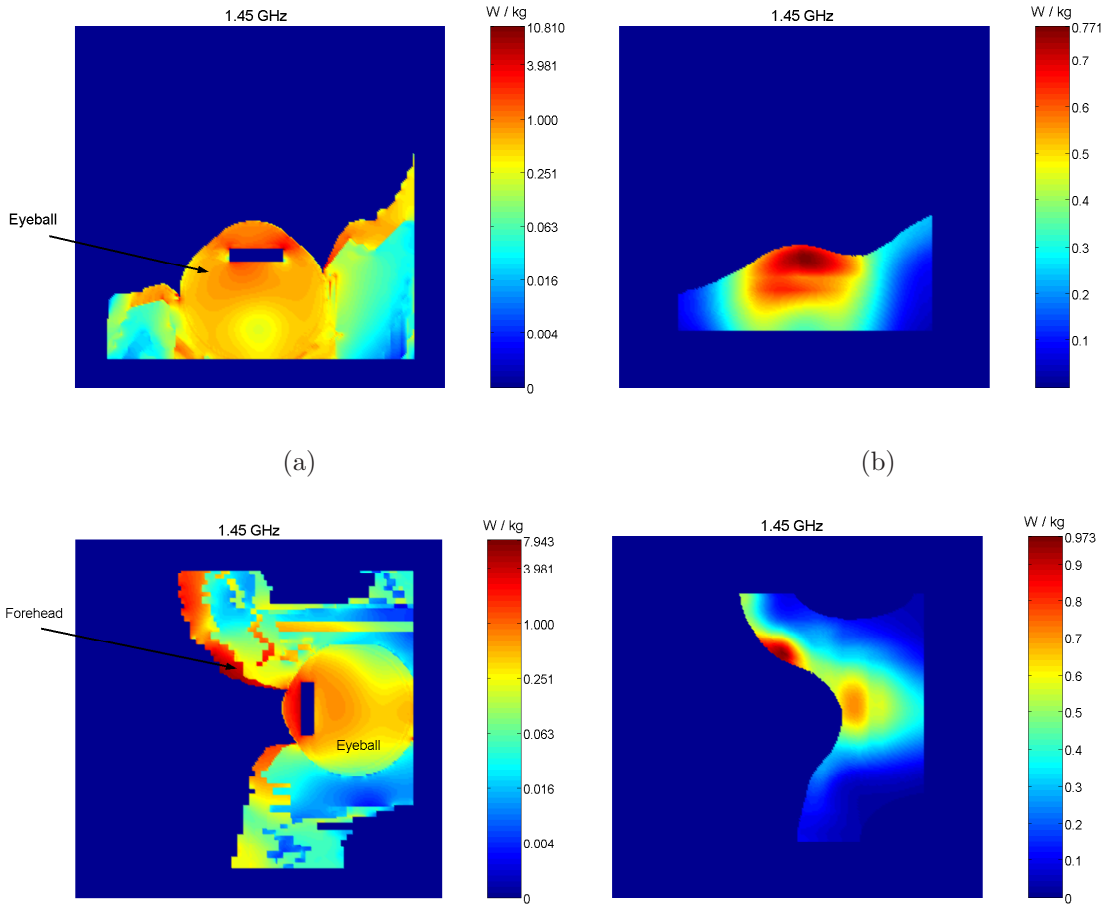

Figure 4.16: SAR profiles computed through various cross sections of the head model for a peak transmitted power of 50 mW at 1.45 GHz (It is observed that maximum power deposition takes place in the fore head region):
(a) Horizontal cross section showing the 1 voxel profile;
(b) The corresponding 1-g profile;
(c) Vertical cross section showing the 1-voxel profile;
(d) The corresponding 1-g profile.

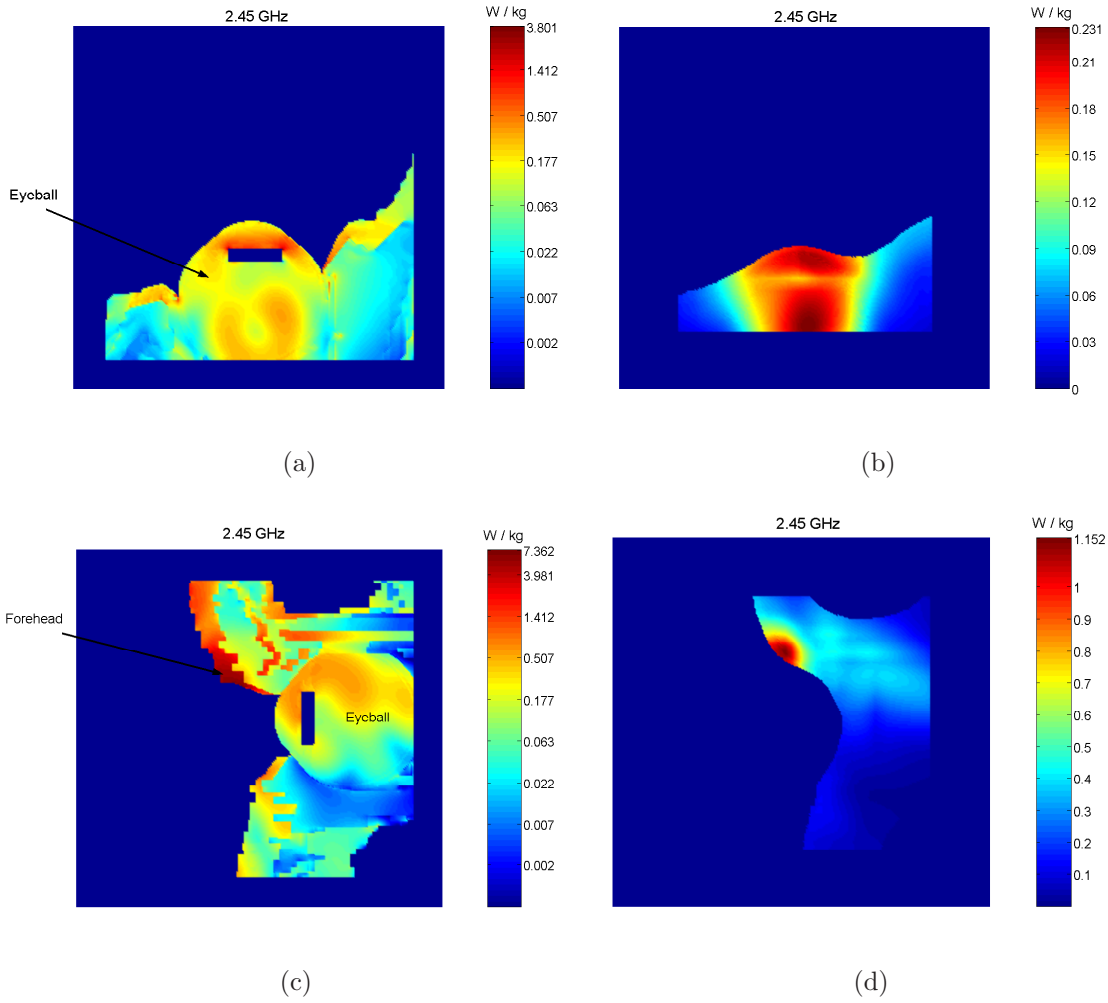

Figure 4.17: SAR profiles computed through various cross sections of the head model for a peak transmitted power of 50 mW at 2.45 GHz (It is observed that maximum power deposition takes place in the fore head region):
(a) Horizontal cross section showing the 1 voxel profile;
(b) The corresponding 1-g profile;
(c) Vertical cross section showing the 1-voxel profile;
(d) The corresponding 1-g profile.

It is observed that maximum power deposition takes place in the forehead region for both the frequency bands. This is attributed to the fact that the radiating extraocular antenna is closest to the forehead in the head model. At 1.45 GHz, a computed peak 1-g SAR of 0.985 W/kg and at 2.45 GHz, peak 1-g SAR of 1.158 W/kg was observed as summarized in Table 4.3. Thus, at both the frequency bands, for a maximum power transmitted of 50 mW, the SAR values do not exceed the IEEE/ANSI guidelines [47].

Table 4.3: Computed SAR at both frequency bands (1.45 and 2.45 GHz).

Frequency (GHz)	Peak 1-g (W/kg)
1.45	0.985
2.45	1.158

4.8 Summary

An investigation of a data telemetry link for a retinal prosthesis employing microstrip patch antennas has been performed and the feasibility of this novel approach is demonstrated both numerically and experimentally. The data telemetry link is established at two frequencies of 1.45 GHz and 2.45 GHz by designing appropriately sized extraocular and intraocular patch antennas. Coupling performance of the link is examined both numerically and experimentally in free space as well as with the intraocular antenna embedded in an eye phantom.

At a separation of 25 mm, in the frequency band of 1.45 GHz, experimentally the coupling was measured to be -42.5 dB in free space and it improved to -37.2 dB when the intraocular antenna was immersed in the eye phantom. At 2.45 GHz, the corresponding experimental free space coupling was -32.0 dB and it improved

to −31.1 dB in the presence of the eye phantom. Numerical and experimental values agreed well for all cases at a separation of 25 mm. The results suggest that the eye ball and tissues of head act as a dielectric lens and improve the coupling performance of the wireless link. Computed peak 1-g SAR at 1.45 GHz is 0.985 W/kg and at 2.45 GHz is 1.158 W/kg and hence are within the IEEE stipulated limit of 1.6 W/kg.

Improvement in the coupling performance due to the dielectric lens effect of the eyeball indicates that for some biomedical applications a microwave telemetry link can be established despite the high absorption of microwaves in the human body.

Chapter 5

Investigation of the Microwave Data Telemetry link Employing Wire Antennas

5.1 Introduction

In the previous chapter, the feasibility of establishing microwave data telemetry links for a visual prosthesis using external and implanted microstrip patch antennas was demonstrated. In the current design of the prosthesis, it is proposed that the implanted antenna and electronics (RF receiver, data processing and signal stimulator chips) reside on the same Si substrate. Such a configuration of the intraocular elements can be encapsulated in a single unit and consumes very little space inside the eyeball. The secondary coil (of the power transfer link) will surround the intraocular unit. It is expected that the fine features of the intraocular antenna (to increase the surface current length) will be achieved though solid state fabrication process. In such a scenario, with microstrip patch antennas as intraocular elements, there are a

couple of issues which need to be addressed for the successful implementation of the intraocular unit: a) The patch antennas comprise of a ground plane. This would necessitate the bonding of a metal layer (aluminum, Al) to the silicon wafer which adds complexity to the fabrication process. b) Since the secondary coil could enclose the ground plane, the mutual flux linkages with the external coil and hence the coupling efficiency for power transfer may be adversely affected.

Therefore, it could be useful to consider alternative compact antenna configurations as intraocular radiating elements to avoid complex performance issues after implementation. A class of antennas which are devoid of ground planes and can perform as effective compact radiators are wire dipoles. Here, we have studied wire dipoles as intraocular radiating elements and the techniques to miniaturize them for the visual prosthesis application.

Several techniques to make wire antenna configurations compact at the operating frequency have been reported in literature. Here, we have investigated the most popular of these structures known as the fractal geometries and the meander line dipoles. In utilizing these wire antennas, two points were of main concern: first, it was necessary to determine whether the fractal or other geometries could, in fact, provide the high degree of compactness that was essential for this application. Secondly, whether these compact wire structures could be impedance matched to the desired system resistance at their resonance frequency (since an important characteristic of compact wire geometries is the reduction in resonant resistance with increasing compactness).

Here, we investigate the different compact wire geometries with respect to the above mentioned criteria. It is demonstrated that fractal geometries can provide the requisite compactness but impedance matching increases the complexity in the feed location for such an antenna configuration. Also, we describe recent work which suggests the ineffectiveness of fractals as size reduced structures and study a planar

meander line dipole configuration which exhibits a high degree of compression efficiency. We propose a novel technique of impedance matching the planar meander line dipole which is simple and yet flexible in that the antenna can be matched at any impedance without additional complexity. Finally, its implementation for a visual prosthesis is discussed and it is shown that at the lower frequency band of 1.45 GHz, a wire antenna element as the intraocular radiating structure may, in fact, improve the performance of the data telemetry link as compared with the intraocular patch antenna.

This chapter is organized in the following manner: Section 5.2 describes the space filling fractal geometries and impedance characteristics for such antennas. Section 5.3 describes alternative compact geometry that could be used for our purpose and section 5.4 presents how effective this alternative compact geometry is compared to fractals. Section 5.5 discusses the implementation issues for a retinal prosthesis and 5.6 describes the dielectric loading influence of the eye on these implemented antennas. In section 5.7 the coupling results with embedded wire dipoles are compared with similar results that we obtained with the intraocular patch antennas.

5.2 Fractal Geometries

Fractal geometries are self-similar (or self-replicating) space filling curves which have been traditionally used for modelling complex objects found in nature such as clouds and coastlines. These contours can add a significant amount of electrical length in a smaller volume due to their unique mathematically iterative properties. Electrical lengths play an important role in antenna design and so this efficient packing abilities of fractals can be utilized for antenna miniaturization. Fractal curves have been extensively researched [100] and its application in antenna design has generated

a lot of interest in the last decade [101, 102, 103, 104]. The mathematical and electromagnetic properties of fractals have been discussed in detail [105] and for the sake of brevity they will not be repeated here.

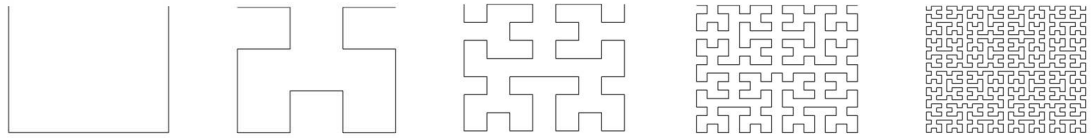

(a) $n = 1$ (b) $n = 2$ (c) $n = 3$ (d) $n = 4$ (e) $n = 5$

Figure 5.1: The first five iterations of the Hilbert curve.

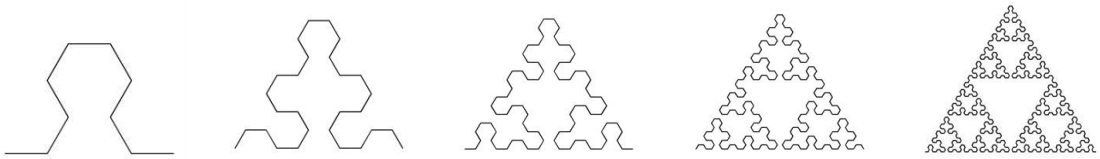

(a) $n = 1$ (b) $n = 2$ (c) $n = 3$ (d) $n = 4$ (e) $n = 5$

Figure 5.2: The first five iterations of the Sierpinski curve.

We studied the size reduction properties of 3 types of fractal dipoles mainly because they demonstrate a planar 2-dimensional 'foot print' which is essential for the intraocular antenna design. The three types of fractals we studied are the hilbert curve, the peano curve and, the sierpinski curve. The first few iterations of the hilbert and sierpinski curves are given in Figure 5.1 and Figure 5.2. To characterize these curves for their impedance matching properties and size reduction capabilities, we simulated prototypes in free space using the available NEC code [106]. For the purposes of this study, we used a wire radius of $10\mu m$ and side dimensions were kept 10 times the actual intended dimensions for a intraocular antenna (i.e. the prototypes had a side dimension of 52.5 mm and the intraocular antenna is supposed to be 5.25

mm a side).

5.2.1 Impedance Matching Fractal Antennas

Recently, techniques to impedance match such antennas have been reported [107]. This method outlines the means to impedance match fractal antennas at their fundamental resonance by moving the feed point along the length of the wire curve towards the end. We utilized this technique to match the fractal geometries we considered in numerical simulations using NEC. This matching technique was applied to the 4th order Hilbert curve, a 3rd order peano curve and a 5th order sierpinski curve to get a 50Ω match by moving the feed point towards the wire end. Figures 5.3, 5.4 and, 5.5 depict the radiation characteristics (current magnitude distribution and radiation pattern) of these fractal geometries along with the feed point location to achieve 50Ω matching at the fundamental resonance.

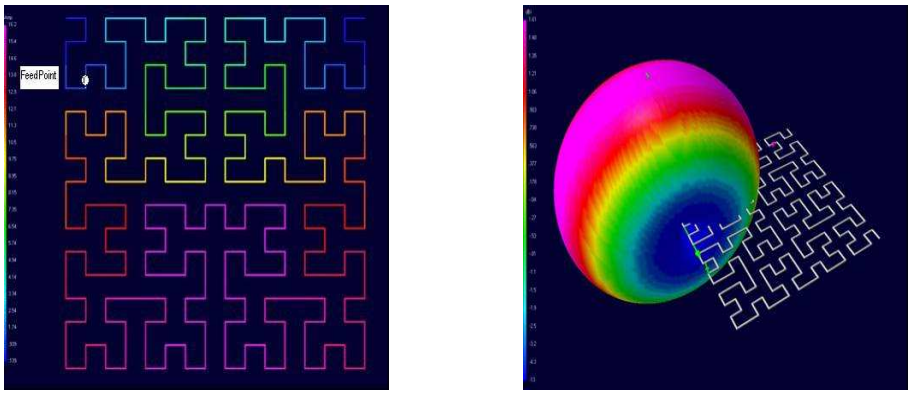

(a) (b)

Figure 5.3: 4th order Hilbert curve matched to 50Ω at its fundamental resonance (VSWR 3:1 BW of 0.05% and Max. Directivity of 1.76 dBi):
(a) The current distribution along its length and the location of the feed point (white dot);
(b) The total radiation pattern at the fundamental resonance.

At a given fundamental resonant frequency of operation (at which the antenna

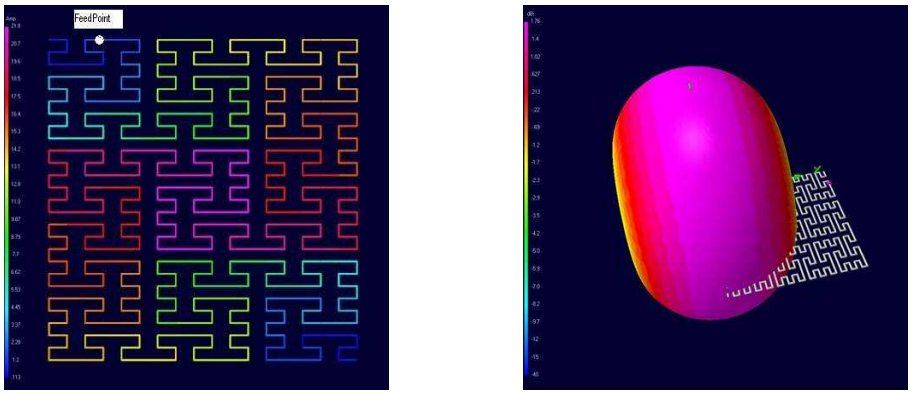

(a) (b)

Figure 5.4: 3rd order Peano curve matched to 50Ω at its fundamental resonance (VSWR 3:1 BW of 0.04% and Max. Directivity of 1.76 dBi):
(a) The current distribution along its length and the location of the feed point (white dot);
(b) The total radiation pattern at the fundamental resonance.

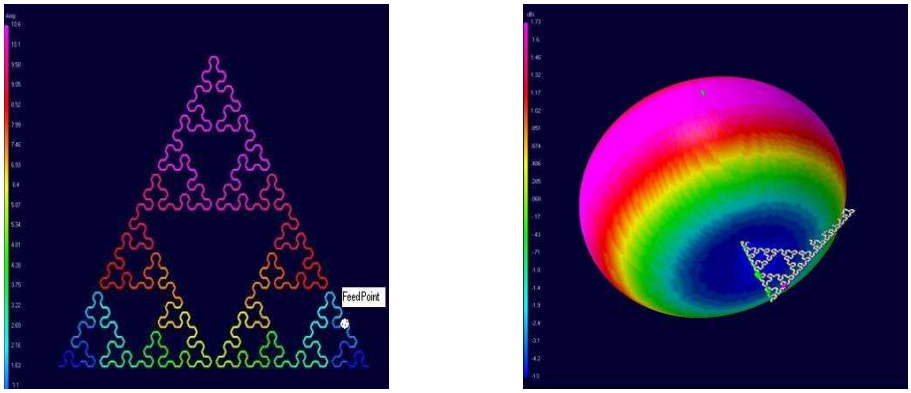

(a) (b)

Figure 5.5: 5th order Sierpinski curve matched to 50Ω at its fundamental resonance (VSWR 3:1 BW of 0.12% and Max. Directivity of 1.73 dBi):
(a) The current distribution along its length and the location of the feed point (white dot);
(b) The total radiation pattern at the fundamental resonance.

is matched), the peano curve exhibited the highest compression efficiency amongst all the three planar curves. Here, we define compression efficiency as the ratio of the frequency of the first full wave resonance of an ordinary dipole to the full wave resonant frequency of the compact dipole structure as given below :

$$C.E. = \frac{f_{dipole}}{f_{compactstructure}}\Bigg|_{fullwave} \tag{5.2.1}$$

Figure 5.2 shows the relative sizes for the three fractal geometries for the same frequency of operation (for the prototypes this frequency was 370 MHz). Table 5.1 lists the relative sizes of the antennas and the BW and directivity observed at the matched fundamental frequency of operation.

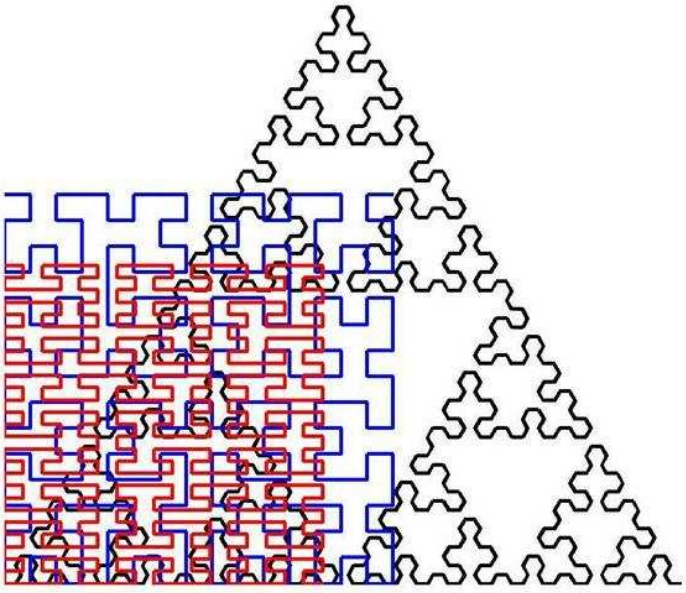

Figure 5.6: Relative size comparison of the three planar fractal dipole antennas at the same fundamental matched frequency of operation.

We observe that to match the fundamental resonance (to 50Ω) in all the three planar fractal dipole antennas considered, the feed point location is achieved towards

Table 5.1: Comparison of the characteristics of the planar fractal antennas.

Fractal	Size (units)	Bandwidth	Directivity (dBi)
Hilbert	3.45×3.45	0.05 %	1.61
Peano	2.82×2.82	0.04 %	1.76
Sierpinski	6×5	0.12 %	1.73

the wire end. Such a location for impedance matching (the match can also be achieved at any other resistance values by varying the location of the feed) may not be easily accessible by a microstrip coplanar balanced feed line in the eventual implemented antenna configuration for the retinal prosthesis.

Hence, for the actual prosthetic implant, an arbitrary location (as obtained for the fractal antennas) for the feed point of the intraocular antenna may be an additional complexity. Moreover, for the total length of the wire used, the fractal geometries offer lesser compression efficiencies than other simple compact meander line geometries. Therefore, it was essential to investigate alternative wire dipole structures which not only facilitate a fixed feed point location for impedance matching but also provide enhanced compactness for a given wire length.

5.3 Alternative Compact Dipole Geometry

Recently, it was reported that fractals may not be the most effective structures in terms of their ability to lower resonant frequency for a fixed total wire length. The effectiveness of any antenna in lowering resonant frequency is very much dependent on current vector alignment in parallel closely coupled sections of wires in its geometry [108]. Moreover, it was demonstrated that the resonant behavior of any space-filling wire antenna is a function of all of its physical characteristics which include its geometry, overall size, total wire length and wire diameter [109].

We investigated a space-filling geometry of a meander line dipole with a high degree of current vector alignment as shown in Figure 5.7(a).

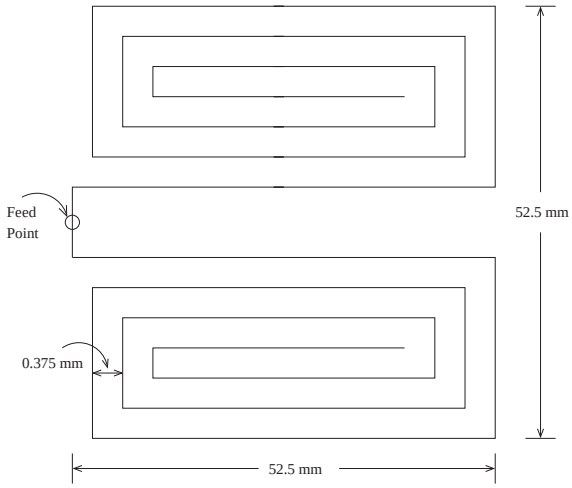

(a)

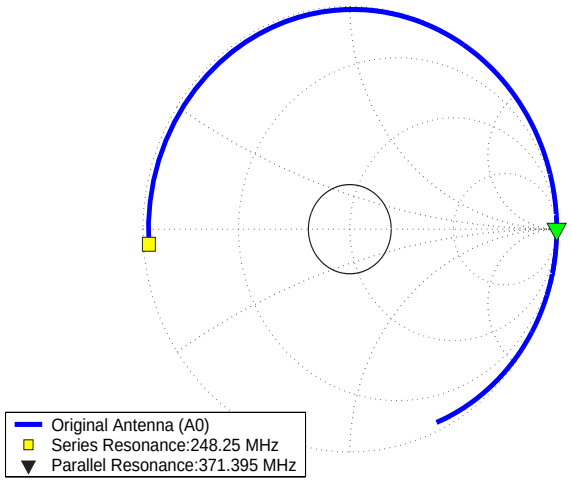

(b)

Figure 5.7: Planar meander dipole antenna configuration:
(a) The prototype A0 considered for NEC simulations (wire radius of 10μ m);
(b) Impedance characteristics of A0 with the feed point at the symmetrical center.

The prototype antenna for the computational study was scaled up 10 times in side length to measure 52.5×52.5 mm and is designated as A0. Its wire diameter was 10μm with a total wire length of 0.75875 m. The wire was considered to be

perfectly conducting devoid of any losses for this work. Its numerical investigation was performed using the NEC 2 engine of NEC Win-PRO where it was modelled using 607 segments each having a length of 1.25 mm. It exhibited its impedance characteristics as shown in Figure 5.7(b).

Here, the current vectors along parallel adjacent coupled sections of wire reinforce to increase the self-inductance and hence lower the resonant frequency lending this structure a very high compression efficiency as compared to the Hilbert curve [108]. This structure will be referred to as the planar meander dipole (or wire dipole) for the rest of this chapter. Moreover, it should be noted that the quality factor Q, or the antenna's radiative usefulness was not the focus of this study and hence is not discussed in detail. However, as is later observed, the prototype exhibits a $kr \sim 0.2$ (much smaller than a radian length; k is the wavenumber and r is the radius), and when operated at its higher order mode, this antenna gives very high directive gain at the expense of bandwidth leading to a very high Q radiator. This performance is consistent with what has been reported over the last few decades [66, 67, 68, 69, 70].

5.3.1 Impedance Matching for Planar Meander Dipole

5.3.1.1 Conventional Matching Technique

At its fundamental resonance, the phase remains almost constant along the length of the wire and it can be matched in the conventional way by moving the feed point towards the wire end. Antenna A0 was matched at its fundamental resonant frequency, by selecting an off-center feed point and moving it along the length of the wire till a good match to 50Ω was obtained. This planar dipole was designated as A1 and the match was achieved with the feed point positioned at segment 18 from the wire end of one of the arms. Figure 5.8 shows the current vector alignment and impedance characteristics for the prototype antenna A1 matched with its feed loca-

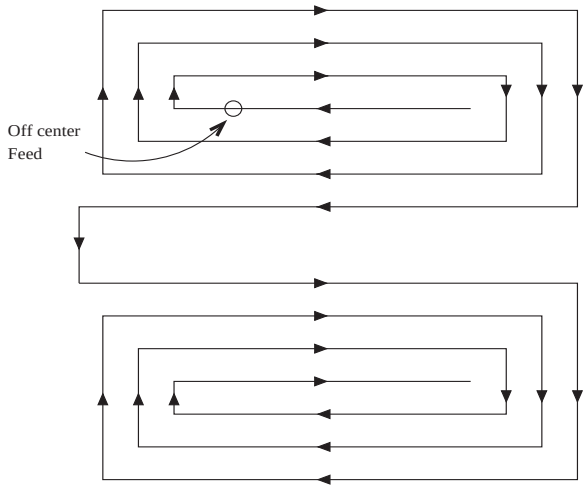

(a)

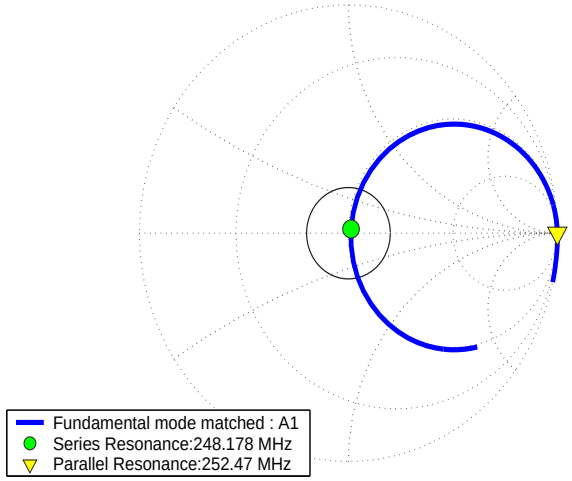

(b)

Figure 5.8: Conventional impedance matching of the fundamental mode by moving the feed point towards the wire end–antenna A1:
(a) Current vector alignment and feed point location;
(b) Impedance characteristics of A1.

tion as depicted. The fundamental resonance for the prototype occurred at 248 MHz and a VSWR 3:1 bandwidth of 0.06 % was observed. As seen from the figure, the current phase remains constant throughout the length of the dipole.

However, the conventional method of impedance matching presents the same complexity (arbitrary feed location) as was observed for the fractal case. In the next subsection, we show a novel method of antenna matching by inducing a current phase reversal along the length by a minor offset in the feed location and then compare this method with the conventional way of matching (feed point at the wire end).

5.3.1.2 Current Phase Reversal for Impedance Matching

To explain the current phase reversal we first consider a simple full wave dipole of the same total wire length of 0.75875 m. It is well understood [110] that when the full wave dipole is fed a quarter wavelength from one end, it exhibits a current distribution that is significantly different (in terms of phase) from the center-fed full-wave dipole. When fed at quarter wavelength offset, due to the induced phase reversal, the dipole exhibits a series resonance at a frequency very close to the full-wave parallel resonance of the center fed dipole as shown in Figure 5.9(a). The current phase reversal due to the off-center feed leads to broadside nulls which is an undesirable effect in the normal dipole. However, in the case of our planar meander line dipole, a phase reversal can improve the directivity in the broadside direction and provide an impedance match very close to the full-wave resonant frequency as is discussed below.

To impedance match the planar meander dipole antenna A0 by inducing a phase reversal, a minor offset had to be introduced in the location of the feed point. Instead of moving the feed point itself, one of the arms of the dipole was shortened to create the necessary minor offset in the feed point location. The dipole arm was shortened incrementally until the induced series resonance indicated a good match to 50 ohms.

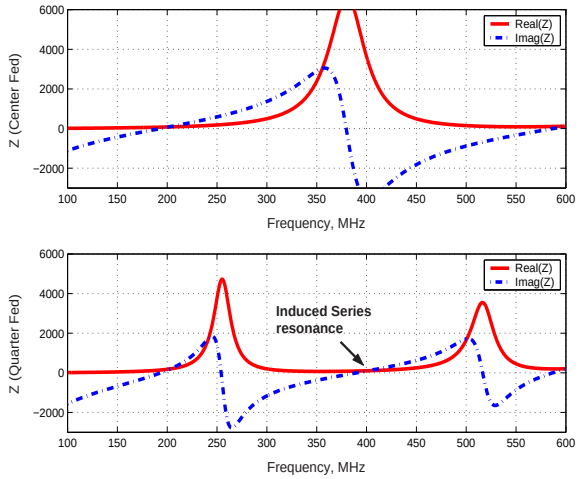

(a)

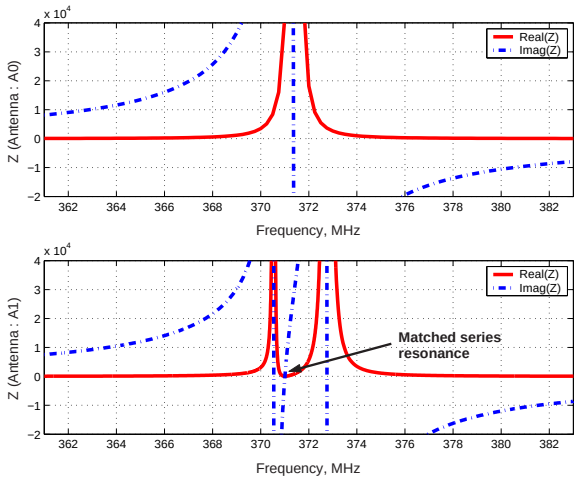

(b)

Figure 5.9: Comparing the impedance characteristics for center fed and off center fed dipole antennas; the off center feeding induces a series resonance for both the types of dipole:
(a) Center fed and Quarter wave offset fed linear dipole;
(b) Center fed and a Minor offset fed meander line dipole.

The impedance characteristics depicting the induced series resonance due to the off center feeding is shown in Figure 5.9(b).

In the prototype, the dipole arm was shortened by 2.5 mm (2 segment lengths) and the modified matched antenna was designated A2. Figure 5.10(a) depicts the modified matched antenna A2 and the current phase reversal which occurs right at its center. Its impedance characteristics are shown in Figure 5.10(b) where the meander dipole is matched at its induced series resonance.

The matched induced series resonance is obtained at 370.008 MHz for A2 which is very close to the unmatched full wave resonance of 371.395 MHz for the prototype antenna A0. (We observed that actually moving the feed point also leads to the same effect and that the exact amount of offset is very critical in obtaining a good match at the induced series resonance). The antenna could be matched at any resistance by controlling the amount of offset (or shortening of the arm) in the feed location. The bandwidth deteriorated significantly and for the prototype considered a VSWR 3:1 bandwidth of 0.0002 % was observed.

Moreover, it was seen that the degree of offset (and hence the amount of shortening of the dipole arm) necessary for inducing a current phase reversal (immediately beyond its full wave resonant frequency) is dependent on the compression efficiency (CE) of the given antenna geometry. In [109] it was shown that due to the high level of current vector alignment in its parallel adjacent arms, an antenna geometry such as A0 in much more efficient in lowering resonant frequency than a Hilbert curve fractal geometry. And, though it is not explicitly reported here, we observed that for a Hilbert curve (order 4) and a Sierpinski curve (order 5), which exhibit a lesser compression efficiency (as defined in Equation 5.2.1), a significant amount of dipole arm had to be shortened in order to induce a current phase reversal.

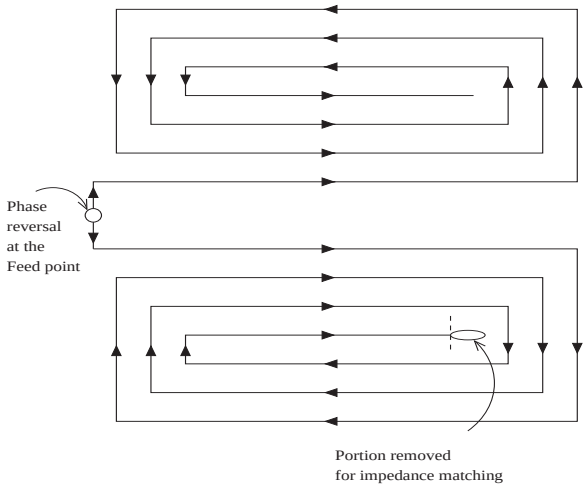

(a)

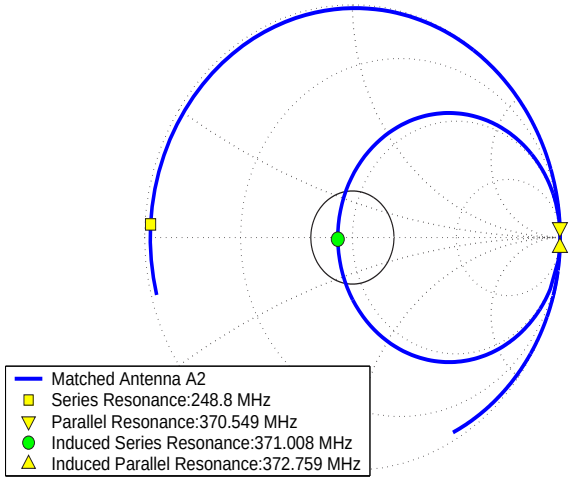

(b)

Figure 5.10: Impedance matching the meander dipole by current phase reversal (while retaining the feed point at the edge)–Antenna A2:
(a) Current phase reversal at the center due to minor feed offset;
(b) Impedance characteristics of A2 showing matching to 50Ω at the induced series resonance.

5.3.2 Current Distribution and Radiation Pattern

Figure 5.11 shows the current distribution (magnitude and phase) for antennas A1 and A2 at their respective matched frequencies. While there is a slight variation of phase along the length of A1 (at its fundamental mode), A2 depicts a phase reversal by 180 degrees approximately at its symmetric center.

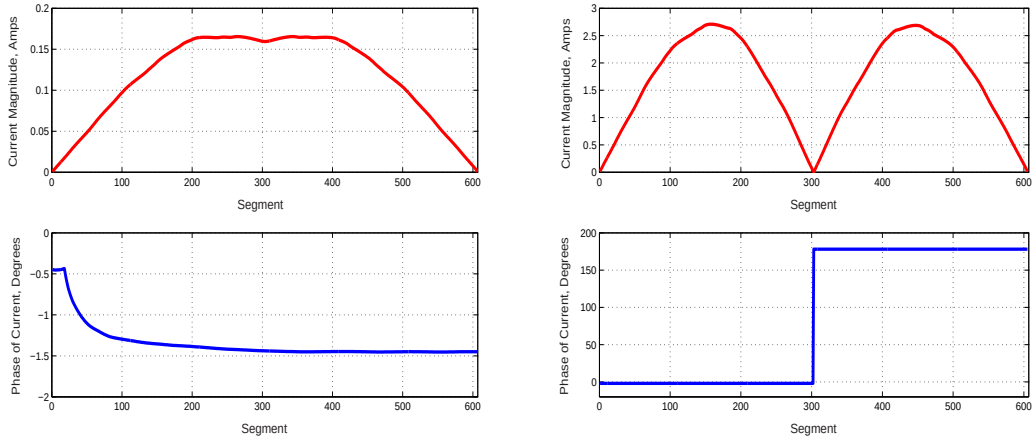

(a) (b)

Figure 5.11: Simulated Current magnitude and phase distribution:
(a) Antenna A1 (fundamental mode matched) ;
(b) Antenna A2 (full wave mode matched).

Figure 5.12(a) and Figure 5.12(b) depict the xy radiation patterns due to antennas A0 (at its unmatched full-wave resonance) and A2 (at its matched series resonance). The phase reversal at the midpoint of A2 facilitates the specific current vector alignment as shown in Figure 5.10(a) which contributes to a highly directive radiation pattern broadside to the plane of the antenna. It is observed from Figure 5.12(a) and Figure 5.12(b), that the radiation from A0 (with no phase reversal) is directed in the azimuthal plane while A2 focuses the radiation in the broadside direction.

Figure 5.12(c) and Figure 5.12(d) compare the radiation patterns of antennas A2 and A1 at their respective matched frequencies. Again, the maximum directivity

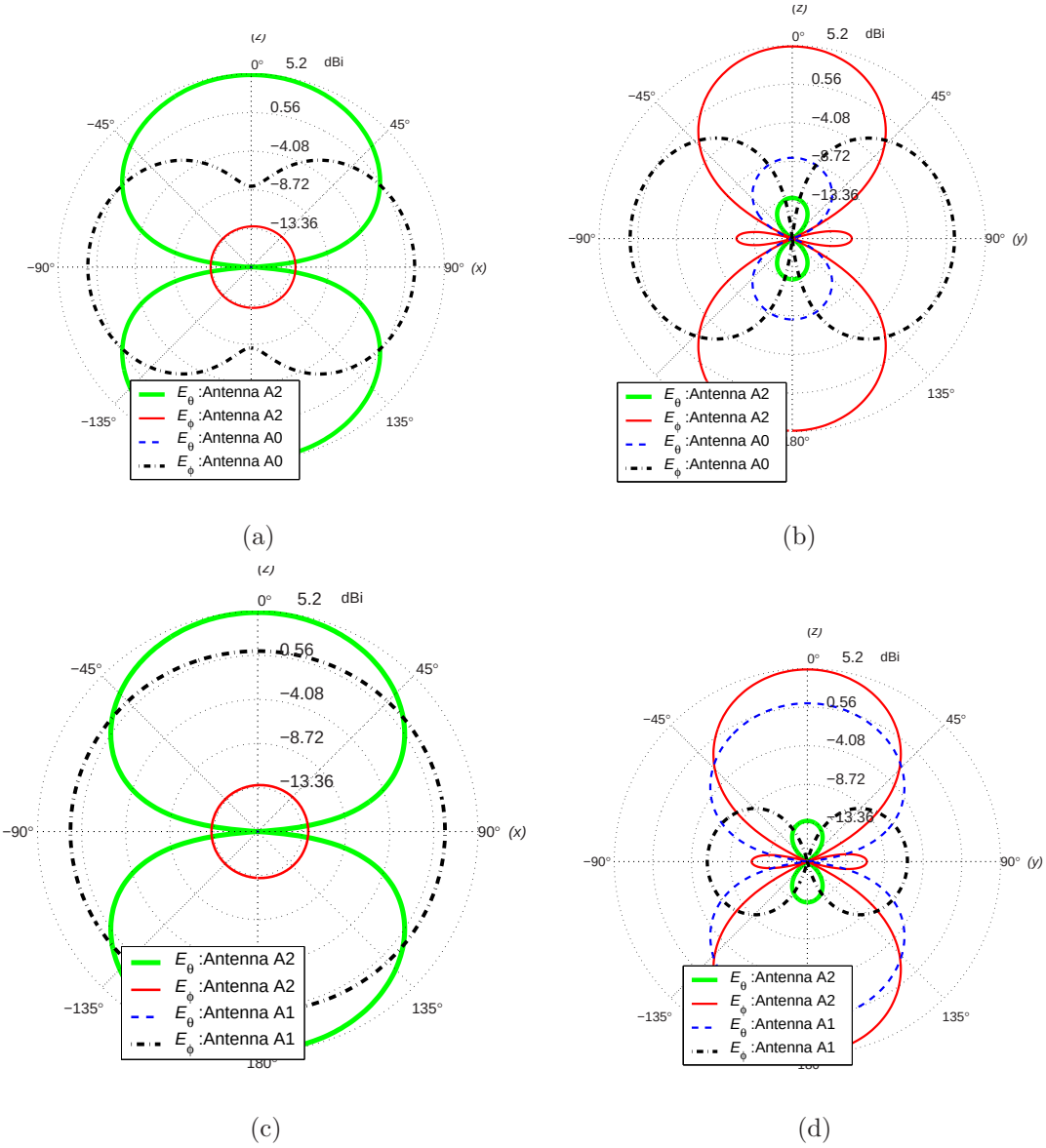

Figure 5.12: Radiation pattern comparison between antennas A0, A1 and A2: (a) Antennas A0 and A2 (XZ plane); (b) Antennas A0 and A2 (YZ plane); (c) Antennas A2 and A1 (XZ plane); (d) Antennas A2 and A1 (YZ plane).

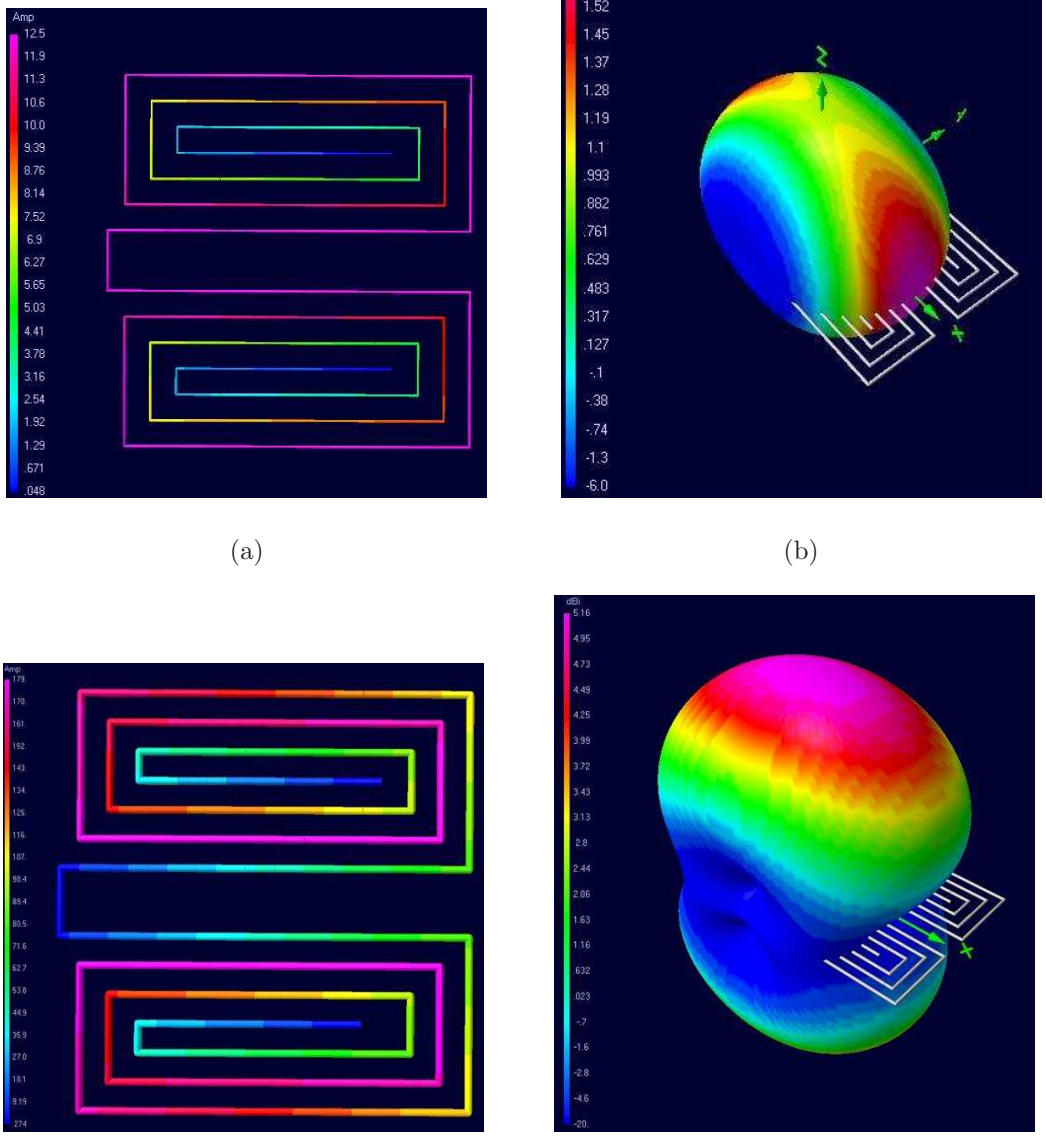

(a) (b)

(c) (d)

Figure 5.13: Total directivity and current magnitude plots for antennas A1 and A2: (a) Current distribution at the matched fundamental resonance; (b) Corresponding total gain plot;
(c) Current distribution at the matched full wave resonance; (d) Corresponding total gain plot.

of A1 conforms to the theoretically expected [110] value for small antennas of ∼1.7 dBi while for antenna A2 it is 5.16 dBi. It must be mentioned that the increase in directivity in Antenna A2 is compensated by a severe reduction in the impedance bandwidth.

We have observed that the method of current phase reversal to impedance match small antennas will improve broadside directivity only in specific cases (like antenna A2) on which the current vectors in adjacent wire segments are aligned favorably. Attempts at matching fractal antenna geometries of Hilbert (order 4) and Sierpinski curves (order 5) by current phase reversal did not yield any improvement in the directivity due to the arbitrary current vector alignment in fractals.

Figure 5.13 depicts the total directivity patterns and current magnitudes of the conventionally matched antenna A1 and antenna A2 matched by an induced current phase reversal at their respective frequencies.

5.4 Comparison of Fractal Antennas with the Edge Matched Planar Meander Line Dipole

Due to the high degree of current vector alignment in the planar meander line antenna, the compactness achieved was significantly more than that with the fractal geometries. To position the feed location at the edge, the planar meander line antenna was impedance matched at its full wave resonance by inducing a current phase reversal. The three different types of planar fractal geometries considered were matched at their fundamental resonances by moving the feed point towards the wire end. At the same matched frequency of operation (approximately 370 MHz–fundamental resonance for the fractals and full wave resonance for the planar meander dipole), a relative size comparison of the prototypes is shown in Figure 5.14. Table 5.2 compares

Table 5.2: Comparison of the characteristics of the planar fractal antennas with the planar meander line dipole.

Geometry	Size (units)	Bandwidth	Directivity (dBi)
Hilbert	3.45×3.45	0.05 %	1.61
Peano	2.82×2.82	0.04 %	1.76
Sierpinski	6×5	0.12 %	1.73
Planar Meander Line	5.25×5.25	0.0002 %	5.16

the performance parameters for all the considered planar wire structures.

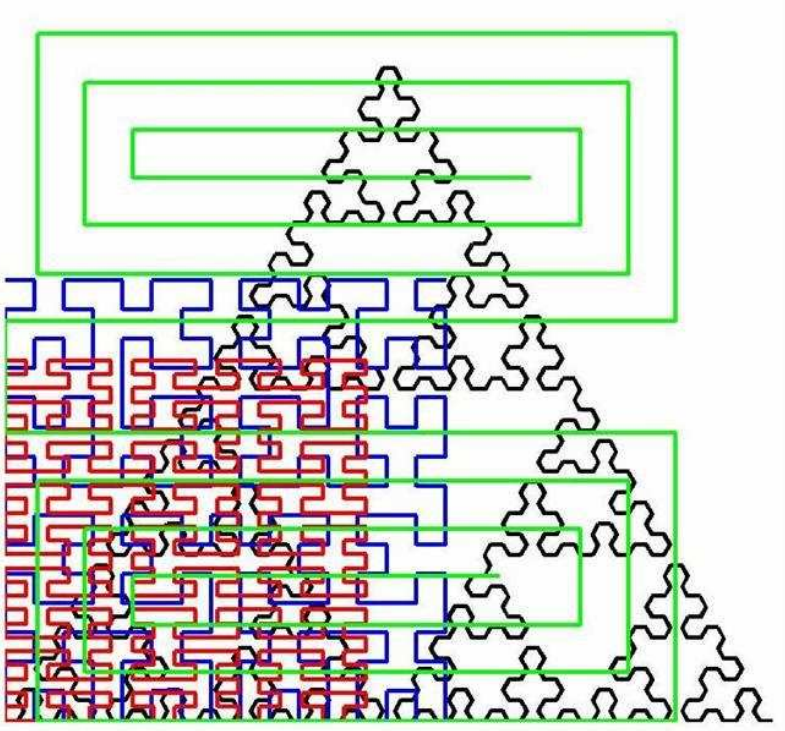

Figure 5.14: Relative size comparison of the three planar fractal dipole antennas and the planar meander line dipole–all matched at the same frequency of operation.

It is seen that the area occupied by the planar meander line antenna at its second resonance, does not increase beyond the fractals by a significant amount due to its inherent compression efficiency. Moreover, it facilitates matching the intraocular antenna configuration at any system impedance while retaining the feed point at the edge. Hence, such a design can be investigated for a visual prosthesis implant to

characterize the performance of the data telemetry link.

5.5 Implementation of the Planar Meander Dipole for a Retinal Prosthesis

The prototypes studied in the NEC simulations measured 52.5 × 52.5 mm and operated at approximately 370 MHz. For the retinal prosthesis, the implemented intraocular wire antennas had to operate in the 1.45 GHz and 2.45 GHz frequency bands. This would enable a performance comparison between the patch and wire antennas as intraocular elements. Moreover, the size had to be restricted to 6 × 6 mm to enable implantation within the eyeball.

Therefore, the wire antennas were designed with dimensions of 5.25×5.25 mm. In free space, the antennas operated at approximately 3.9 GHz (a 10 times increase in frequency of operation). Hence, a high dielectric constant of 9.2 was used with a thickness of 1.5 mm and the intraocular antennas were implemented using standard PCB prototyping milling machines to operate in the 1.45 GHz frequency band. An unbalanced feed mechanism was used (SMA connectors) and the antennas were matched to 50Ω by shortening one of the arms. The final implemented matched intraocular wire dipoles operated at approximately 1.41 GHz and their resonance frequency was matched to that of the extraocular antenna (microstrip patch antenna) by adjusting the length of the arms.

A picture showing the implemented wire antenna and corresponding extraocular antenna operating at approximately 1.41 GHz is shown in Figure 5.15. In this work, the data telemetry link was characterized for intraocular wire dipoles only in the 1.45 GHz frequency band. Also, the experimental set up used for measurements was identical to the one described in chapter 4.

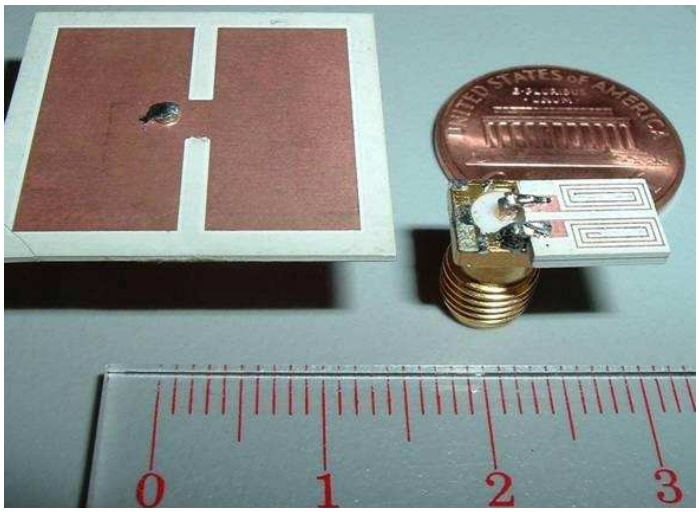

Figure 5.15: The implemented T_x (extraocular) and R_x (intraocular wire dipole) antennas to operate in the 1.45 GHz frequency band.

5.6 Influence of the Eyeball on the Intraocular Wire Antenna Characteristics

Similar to the case of the patch antenna, when the encapsulated intraocular wire antenna is immersed in the eye phantom filled with humor simulant fluid, due to the dielectric loading effect, the wire dipole is completely de-tuned [99]. The resonant frequency gets lowered and the return loss degrades due to an inductive effect in its impedance characteristics.

Thus, for experimental measurements in presence of the model, the same procedure as was done for intraocular patch antennas was carried out. The intraocular wire antenna was modified to account for the inductive loading effect due to immersion in the eye phantom. The new intraocular antenna was designed so that it exhibits significant capacitive behavior at the desired extraocular antenna frequency in free space. This was achieved by altering the lengths of both the arms of the wire dipole till it exhibited capacitive behavior in free space. Thus, when the capacitive wire

dipole was encapsulated and immersed in the eye phantom, the inductive loading influence improved the impedance characteristics and re-tuned its matched resonant frequency to that of the extraocular patch antenna.

It was observed that the inductive influence deteriorated the impedance characteristics of the immersed wire antenna much more than the patch antenna in the 1.45 GHz band. And consequently it was more difficult to achieve a proper capacitive behavior in free space to account for the inductive influence (on immersion) for the intraocular wire dipole antenna. Figure 5.16 depicts the influence of the eyeball on the antenna characteristics. For reference, Figure 5.16(a) and Figure 5.16(b) show the impedance characteristics for the re-designed intraocular patch antenna (in free space and after immersing in the eye phantom) and Figure 5.16(c) and Figure 5.16(d) show the same for the intraocular wire antenna.

The implemented re-designed antenna to operate when embedded in the eye model and the one designed to work in free space are shown in Figure 5.17.

In the NEC simulations of the prototype meander line dipole in free space, the bandwidth was very less at the matched induced series resonance. On implementation on a thick dielectric substrate ($\epsilon_r = 9.2, h = 1.5$) mm, the bandwidth improved due to the losses involved. At 1.41 GHz operation, a 2:1 VSWR bandwidth of approximately 20 MHz was observed as is evident from Figure 5.16(d).

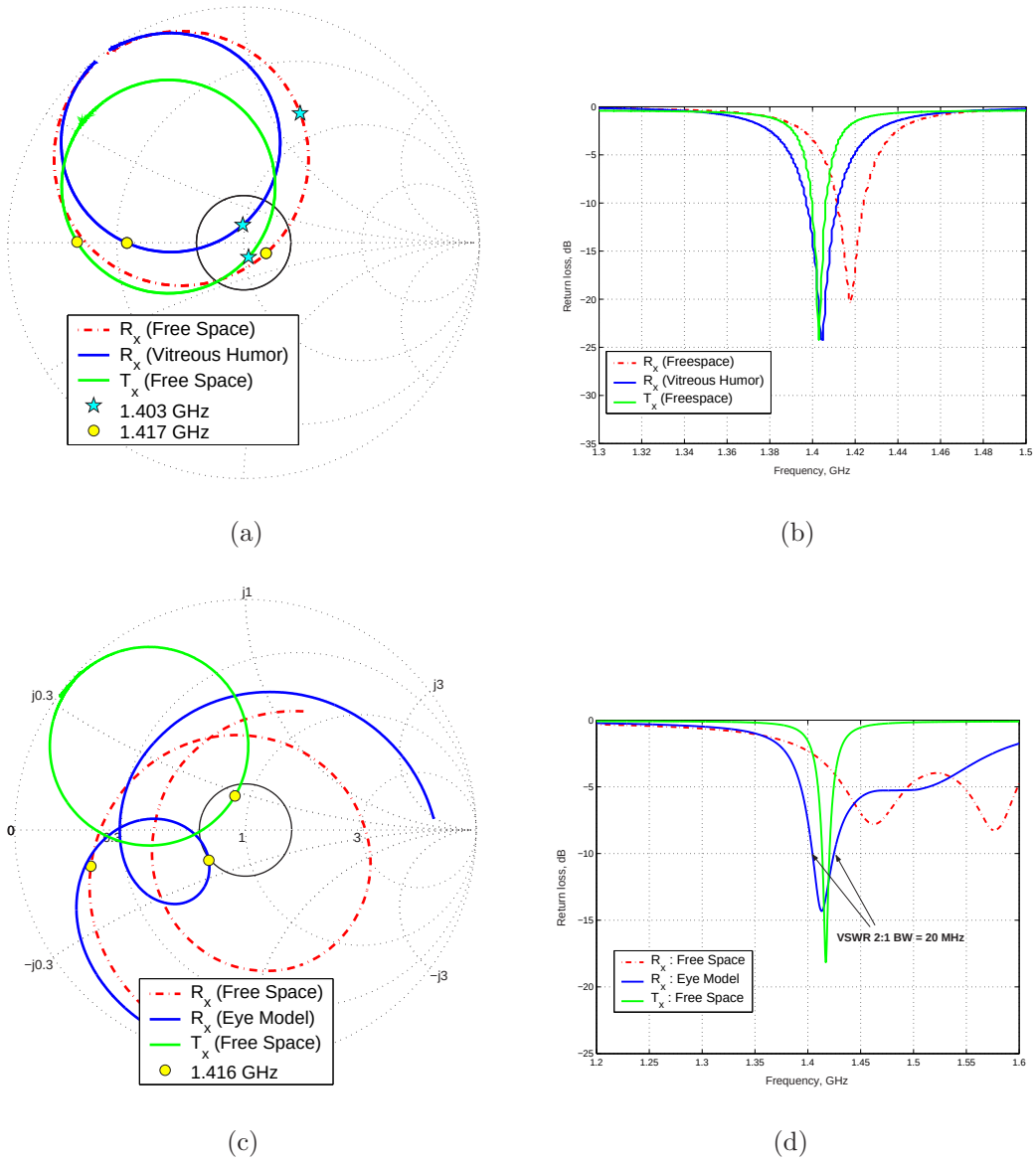

Figure 5.16: Inductive (dielectric) loading influence of the vitreous humor simulant fluid of the eye model on the intraocular antenna (encapsulated in a plastic sheath) and immersed to the appropriate depth in the model:
(a) Influence on patch antenna and its correction;
(b) Return loss characteristics for the patch antenna in the 1.45 GHz band;
(c) Influence on meander wire dipole antenna and its correction;
(d) Return loss characteristics for the wire dipole antenna the 1.45 GHz band.

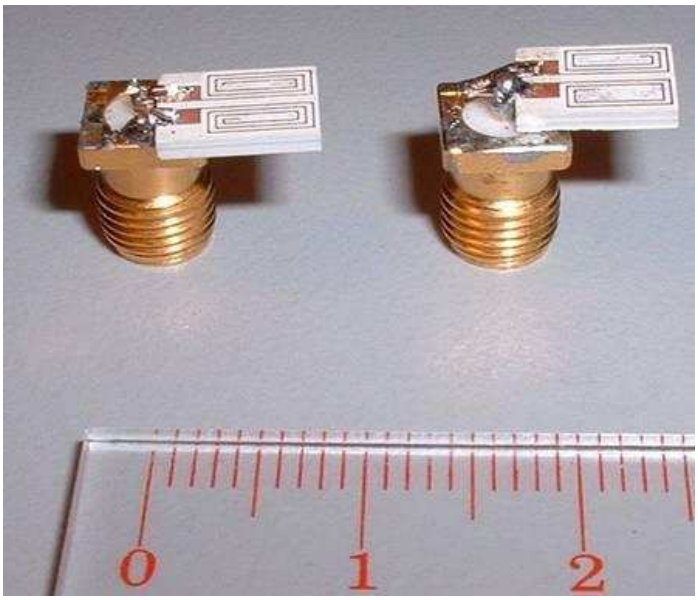

Figure 5.17: The implemented R_x antennas: On the left is R_x designed to operate in free space; Shown on the right is the R_x re-designed to operate when embedded inside the eye model.

5.7 Comparison between Patch and Wire antennas as Intraocular elements in the Data Telemetry Link

5.7.1 Coupling Measurements in Free Space

At a separation of 25 mm in free space (between the extraocular and intraocular (immersed) antennas), coupling with embedded patch antenna is experimentally observed to be -43.5 dB while with the embedded wire dipole antenna coupling is -36.8 dB. Figure 5.18 compares the coupling observed with the patch antenna and the wire dipole antenna.

A significant improvement in coupling (6–7 dB) is observed with the intraocular wire dipole antenna as compared to the patch antenna. This is attributed to the

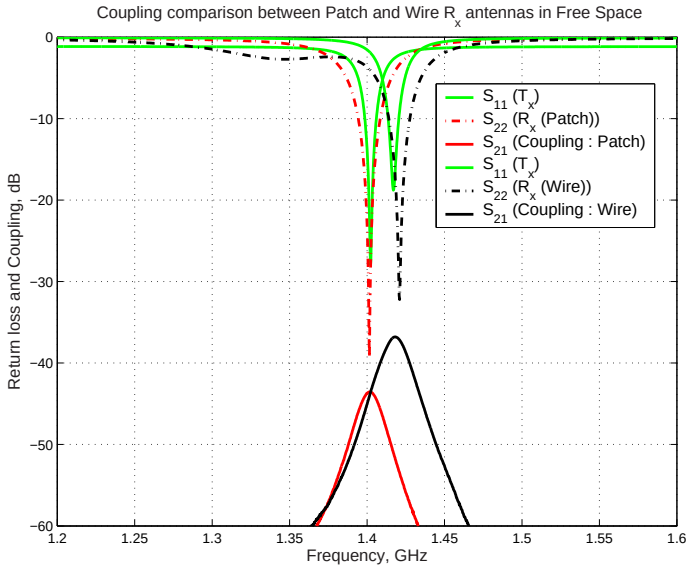

Figure 5.18: Comparison of the coupling performance between patch and wire dipole antenna as the intraocular element (in free space at a fixed separation of 25 mm between the extraocular and intraocular antenna).

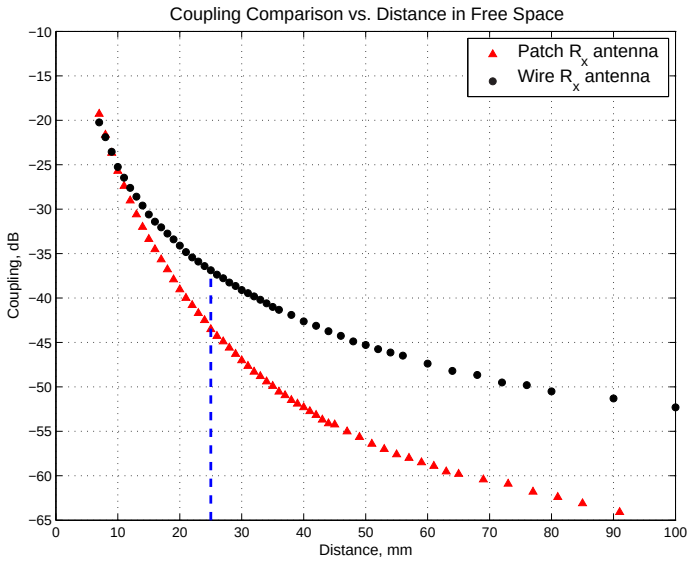

Figure 5.19: Coupling comparison as a function of separation in free space (between the patch and wire dipole antenna as the intraocular element).

enhancement in broadside directivity of the wire dipole antenna (due to the current phase reversal). Moreover, the use of an unbalanced feed mechanism may be affecting the coupling result to an extent. Figure 5.19 depicts the coupling performance as a function of separation which shows improved coupling with the wire dipole antenna.

5.7.2 Coupling Measurements in Presence of the Eye Model

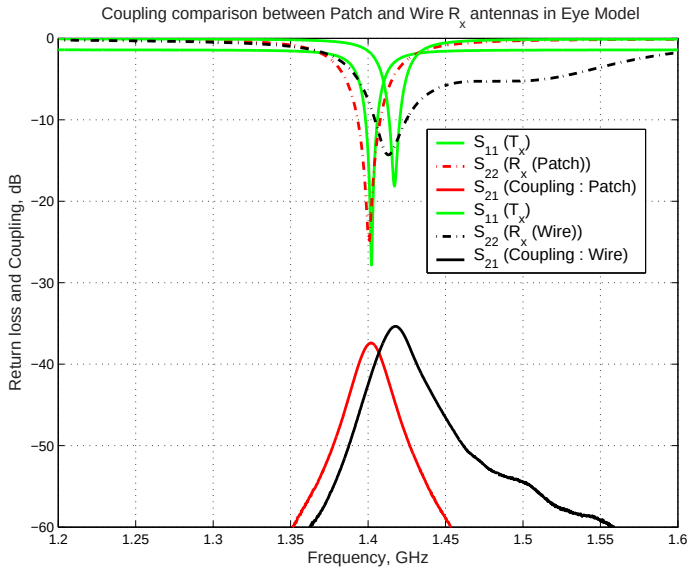

Figure 5.20: Comparison of the coupling performance between patch and wire dipole antenna as the intraocular element (with the intraocular antenna embedded in the eye model at a fixed separation of 25 mm between it and the extraocular antenna).

For comparison with an intraocular patch antenna, a similar set of measurements were taken with the re-designed intraocular wire dipole (to account for inductive influence) immersed in the eye model. At a separation of 25 mm (between the extraocular patch antenna and the encapsulated wire dipole immersed in the eye phantom), coupling was observed to be -35.8 dB while with the intraocular embedded patch antenna it was observed to be -37.8 dB. Figure 5.20 compares the coupling observed with the patch antenna and the wire dipole antenna.

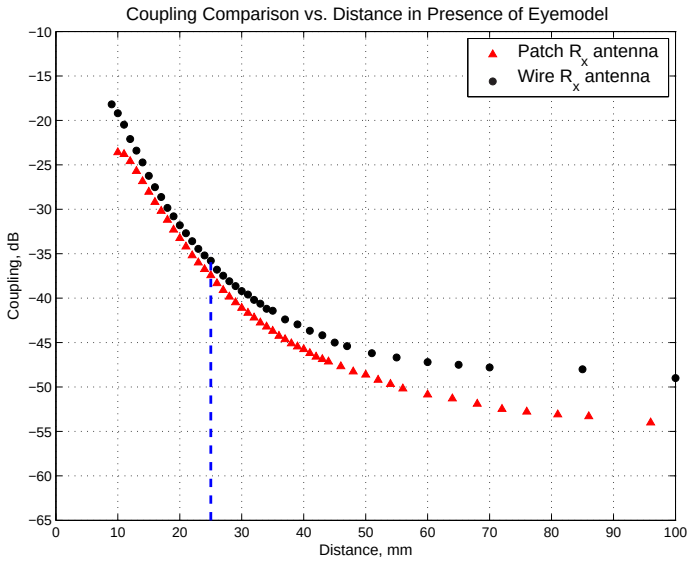

Figure 5.21: Coupling comparison as a function of separation in the presence of the eye model (between the patch and wire dipole antenna as the intraocular element).

In this case, a minor improvement in coupling with embedded wire antenna is observed (1–3 dB). As is evident from Figure 5.21, even in presence of the eye model, the performance of the link as a function of separation was better (higher coupling) with the embedded wire dipole than with the embedded patch antenna.

5.7.3 Enhancement in Coupling Performance Due to the Dielectric Lens Effect of the Eye Model

It was reported in chapter 4, that when the intraocular antenna is immersed in the eye model, both numerically and experimentally, an enhancement in coupling was observed. This enhancement was of the order of 4–6 dB at 1.45 GHz and 1–2 dB at 2.45 GHz for the intraocular patch antennas. This effect was attributed to the fact that the curvature of the eyeball and the head tissues may act as a dielectric lens and enhance coupling performance.

Hence, it was of interest to observe the enhancement in coupling with the wire

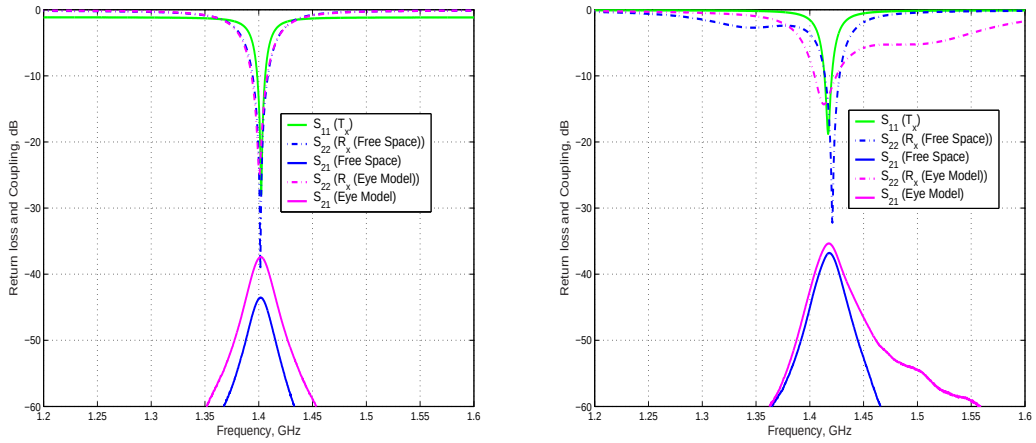

(a) (b)

Figure 5.22: Comparing the enhancement in coupling due to the dielectric lens effect (with intraocular patch and wire dipole antenna) in the 1.45 GHz band:
(a) Improvement with the embedded patch antenna (4–6 dB);
(b) Improvement with the embedded wire dipole antenna (1–2 dB).

dipole and compare the results with the corresponding patch antenna results. Figure 5.22 compares the improvement observed with intraocular wire dipole and patch antenna. As depicted in Figure 5.22(a), with the patch antenna element, the improvement was of the order of 4–6 dB while as seen from Figure 5.22(b) the improvement was lesser of the order of 1–2 dB with the intraocular wire dipole antenna.

5.8 Summary

Compact planar wire dipole antenna geometries' impedance matching properties and compression efficiencies are compared with respect to their use as intraocular elements in a retinal prosthesis. A novel method of matching a specific planar meander line dipole antenna at its higher order mode (full wave resonance) has been discussed and compared with the conventional technique of matching the fundamental mode. It was demonstrated that for specific meander wire antenna geometries—a minor offset

in the feed point—introduced by shortening one of the dipole arms can induce a current phase reversal and provide an impedance match while retaining the feed point at the structure's symmetrical center. Phase reversal on wire antenna configurations possessing a high degree of current vector alignment among adjacent wire lengths can improve the broadside directivity, albeit at a deterioration in the bandwidth.

An edge fed planar meander line dipole antenna measuring $5.25 \times 5.25 \times 1.5$ mm is implemented to operate at 1.45 GHz for its use as an intraocular element in a retinal prosthesis. This wire dipole antenna is impedance matched using the current phase reversal technique. Coupling measurements are performed both in free space and with the wire dipole antenna embedded in an eye model and compared with corresponding results with an embedded patch antenna. At a fixed separation of 25 mm, the coupling measurements in free space and in the presence of the eye model are -36.8 dB and -35.8 dB respectively. It is observed that both in free space and in presence of the eye model, the coupling with the embedded wire dipole antenna is higher than that observed with an embedded patch antenna.

Compact wire dipole antennas can be implemented and matched to any system impedance using the novel impedance matching technique discussed here for their use in human body implants.

Chapter 6

Characterization of the Thermal Elevation in the Human Eye and Head due to the Operation of a Retinal Prosthesis

6.1 Introduction

Chapter 1 outlined the current progress towards a rehabilitative prosthetic device which can be designed to provide artificial electrical stimulation on the retina and thus partially reverse visual loss in some patients. We are considering a dual unit visual

prosthetic system. Chapter 4 and 5 described the feasibility of using antennas for data telemetry as a possible future enhancement beyond the inductive data telemetry system currently in existence. However, for the results described in this chapter, only the currently existing inductive coil telemetry is considered in the operation of the system. In such a system, the extraocular unit includes a camera for image collection, data encoding chip and a primary coil for inductive telemetry. A secondary coil, signal processing chips, current stimulator chip and an electrode array make up the intraocular unit.

Operation of the wireless inductive telemetry link leads to electromagnetic (EM) power absorption in the eye and surrounding tissues. Physiological hazards due to EM power deposition in tissues are known to be largely thermal in nature [111]. Also, the power dissipation due to operation of the implanted chip leads to increase in the natural steady state temperature of the eye and surrounding head tissues. Hence, both, the deposited EM energy due to wireless telemetry link (quantified in terms of specific absorption rate or SAR) as well as the power dissipation in the implanted electronics account for the heating induced in the eye and head tissues [96].

Several studies have been conducted to investigate the temperature increase in head and eye due to cell phone usage [112, 113], in the presence of wireless LANs [114] or to determine heating induced in the eye and formation of cataracts [115, 116, 117]. In [96], SAR and thermal elevation in a 2-dimensional model of the human head and eye due to the operation of the retinal prosthesis is computed. As is mentioned in [96], a 3-dimensional model is essential for a complete characterization of the temperature distribution in implanted electronics and to model the heat flow in the head.

In this work, first we present the methods and models employed to compute thermal elevation in a 3-dimensional human head-eye model due to the operation of the wireless telemetry link and implanted electronics of a retinal prosthesis. Specifically,

an explicit Finite Difference Time Domain (FDTD) formulation of the Bio-Heat equation (BHE) is employed with a 3-dimensional head eye model to evaluate the temperature increase in the eye and surrounding head tissues. As a first step, a validation of the thermal model and method used is presented by comparison with *in vivo* measurements of intraocular heating performed in the eyes of dogs. Induced temperature increase in the eye and surrounding tissues is then estimated for several different operational conditions of the implanted chip. It is shown that, in the vitreous cavity, a temperature elevation of 0.26°C is observed after 26 minutes for a chip dissipating 12.4 mW when positioned in the mid-vitreous while it is 0.16°C when the chip is positioned in the anterior portion between the eye's ciliary muscle. Corresponding temperature rises observed on chip are 0.82°C for both the positions of the chip.

This chapter presents a comprehensive account of temperature elevations in different tissues under different operational conditions and is organized into six main sections. A description of the anatomically accurate head model (and its portions) used in the computational domain is given in section 6.2 followed by a brief summary of the numerical methods employed in section 6.3. Section 6.4 shows a validation of the thermal model used in simulations by comparison with measured data obtained from experiments involving implanted heaters in the eyes of dogs. Simulated results on power absorption due to operation of the wireless link and temperature increase in the head model due to the implanted chip power dissipation are reported in sections 6.5 and 6.6. Influence of different positions, orientations, sizes and power dissipation levels of the implanted chip on thermal elevation are investigated.

6.2 Human head model

As explained in chapter 4, the data for the head model was obtained in the form of cross sectional slices of 1 mm resolution from the National Library of Medicine (NLM) "Visible Man Project" [95]. The head model was discretized further–to reach a spatial resolution of 0.25 mm (64 times the original one) using a method of interpolation in all three dimensions. The detailed features of the eye were represented as described in [96] and the dielectric properties of the body tissues at the frequency of 10 MHz were obtained from the online database compiled by C. Gabriel [97]. For the SAR computation, a portion of this head model was extracted and used in the computational domain along with the extraocular coil as shown in Figure 6.1.

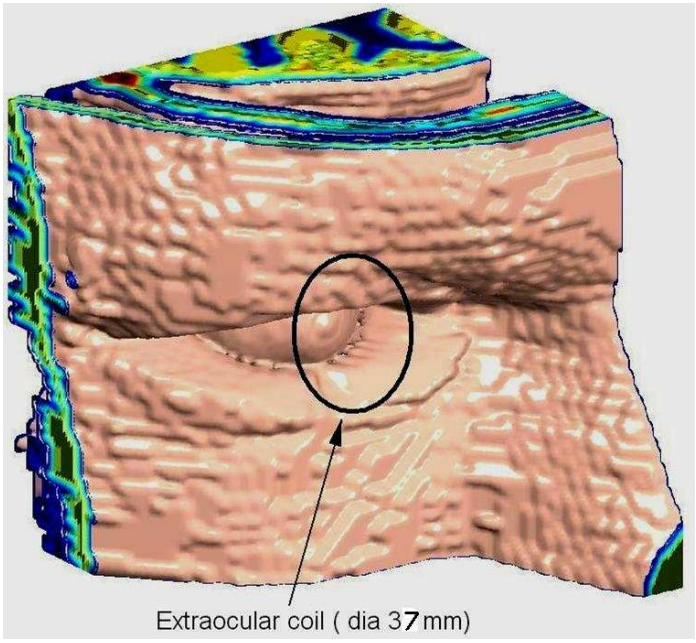

Figure 6.1: Portion of the head model along with the external (primary) coil utilized for computing the SAR induced due to wireless telemetry link.

While computing the initial basal temperature distribution, almost the whole upper portion of the head was included in the computational domain as shown in Figure 6.2. This was done to ensure that the inaccuracies in the temperature distribution

due to the abrupt truncation of the head model occurred at regions far removed from the eye and its surrounding head tissues. A portion of the head model similar to the one shown in Figure 6.1 was extracted and utilized in the computational domain (without the coil) for thermal elevation computations. For thermal simulations, the resolution of the model was reduced to 0.5 mm to reduce the size of the model and hence save on the computational resources of time and memory.

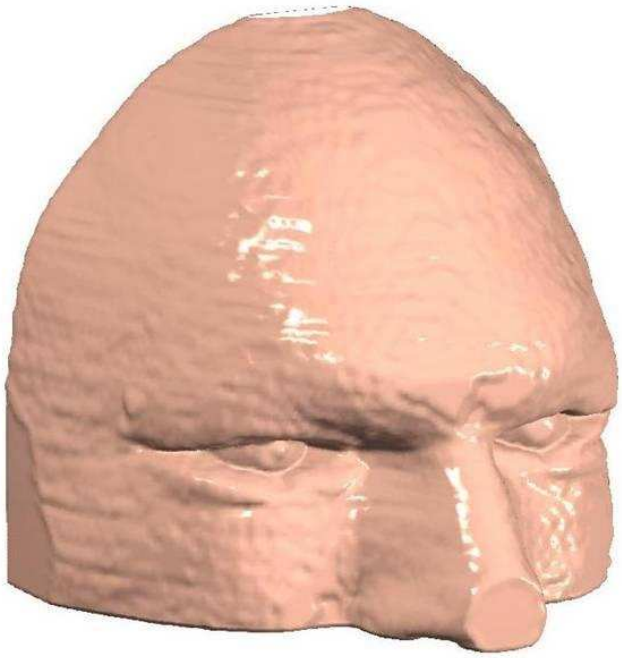

Figure 6.2: Head model utilized for computing the initial steady state temperature distribution.

The eye lens was removed in all cases of SAR computations and simulations for thermal elevations since the intraocular unit of the retinal prosthesis is meant to be encapsulated and hinged in between the eye's ciliary muscle.

6.3 Methods for Computational Analysis

Electromagnetic energy is deposited in the eye and surrounding head tissues due to the operation of the wireless telemetry link through coils at a low frequency (2–10 MHz). The Finite Difference Time Domain (FDTD) method is employed to quantify the power deposition in terms of SAR. If the SAR values exceed the stipulated guidelines [47], electromagnetic power deposition will be considered as an external heat source in the thermal simulations.

6.3.1 SAR computation

A 3-dimensional D-H formulation of the FDTD method [52] is used to compute the induced electromagnetic energy in a 0.25 mm resolution head model. Material independent Perfectly Matched Layer (PML) is used as an absorbing boundary condition so that the model can be immersed in the PML layers as done in [90].

For computing the SAR induced by the wireless telemetry link, a circular coil of approximately 37 mm diameter is modelled at a distance of 20 mm from the eye and excited by a 2 A current at 10 MHz. Absorbed power is quantified as $SAR = \sigma|\overrightarrow{E}|^2/2\rho$ in [W/kg] for conductivity, σ, electric field $\overrightarrow{E}$, and mass density, ρ at each cell. In order to determine their conformity to the IEEE/ANSI standard [47], peak 1-g SAR (SAR_{1g}) is evaluated.

6.3.2 Thermal Model

Thermal elevation in biological tissue can be computed by means of the bio-heat equation. The formulation of the bio-heat equation for numerical implementation in this work closely parallels that in [96, 118], and will only be briefly summarized here. Taking into account external thermal sources, the bio heat equation can be written

as:

$$C\rho\frac{\partial T}{\partial t} = \nabla\cdot(K\nabla T) + A - B(T - T_B) + \underbrace{\rho SAR + P_{chip}^{(density)}}_{ExternalHeatSources} \quad \left[\frac{W}{m^3}\right] \tag{6.3.1}$$

where the expression on the left is the temperature increase per unit time multiplied by the thermal capacitance per unit volume (given as the product of the specific heat of that specific tissue (C[J/(kg $\cdot^\circ$ C)]) and density of that tissue (ρ[kg/m^3])). The terms on the right represent the different ways of heat accumulation or removal from the tissue:–

- $\nabla\cdot(K\nabla T)$: Thermal spatial diffusion term leading to heat transfer through conduction (K[J/m $\cdot$ s $\cdot^\circ$ C]).
- A: tissue specific internal metabolic heat production (J/(m^3 $\cdot$ s)).
- B: tissue specific capillary blood perfusion coefficient (J/(m^3 $\cdot$ s $\cdot^\circ$ C) leading to heat transfer proportional to difference in tissue temperature (T) and blood temperature (T_B).
- External heat sources: ρSAR due to induced electromagnetic power deposition and $P_{chip}^{density}$ due to implanted chip power dissipation.

Heat exchange at the tissue interface with the surrounding environment is modelled by imposing the continuity of heat flow perpendicular to the skin surface as the boundary condition and is expressed as:

$$K\frac{\partial T}{\partial n}(x,y,z) = -H_a(T_{(x,y,z)} - T_a) \qquad \left[\frac{W}{m^2}\right] \tag{6.3.2}$$

Table 6.1: Thermal parameters of the head model tissues under natural steady state conditions AND material composition of the heater probe and implanted chip

Tissue	C J/(kg $\cdot^\circ$ C)	K J/(m $\cdot$ s $\cdot^\circ$ C)	B_0 J/(m^3 $\cdot$ s $\cdot^\circ$ C)	A_0 J/(m^3 $\cdot$ s)
Air (Internal)	1300	0.030	0	0
Aqueous Humor	3997	0.594	0	0
Blood	3840	0.530	0	0
Bone cortical	1300	0.400	3400	610
Bone cancellous	1300	0.400	3300	590
Bone marrow	2700	0.220	32000	5700
Brain Grey matter	3700	0.570	35000	10000
Brain white matter	3600	0.500	35000	10000
Cartillage	3400	0.450	9100	1000
Cornea	4178	0.580	0	0
Cerebro Spinal Fluid	4200	0.620	0	0
Eye's ciliary muscle	4178	0.580	0	0
Fat	2500	0.250	520	180
Lens	3000	0.400	0	0
Muscle	3600	0.500	2700	690
Mucous membrane	3300	0.430	9000	1600
Retina	3680	0.565	35000	10000
Skin	3500	0.420	9100	1000
Vitreous Humor	3997	0.578	0	0
Composition of IMPLANTED HEATER and its thermal properties				
Teflon	1172	0.200	0	0
Ceramic	1025	29.00	0	0
Copper	380	60.00	0	0
Composition of IMPLANTED CHIP and its thermal properties				
Composite material	700	60.00	0	0
Insulation	880	30.00	0	0

where n is the normal to the skin surface and the right hand expression models the heat losses from surface of the skin due to convection and radiation which are proportional to the difference between the skin temperature ($T_{(x,y,z)}$) and external environment temperature (T_a assumed constant at 24°C), H_a is the convection coefficient for heat exchange with the external temperature. Heat losses due to sweating are not considered in this study.

Thermoregulatory mechanisms impart the capability to the human body to regulate the temperature at an almost constant value of approximately 37°C at its core. Owing to the nature of application for the thermal problem in the present work, thermoregulatory effects are considered to influence only two physiological parameters in Equation 6.3.1. The tissue specific basal metabolic rate (A) and blood perfusion coefficient (B) are modelled to be temperature dependent. Thermal dependence of basal metabolic rate is expressed as [118]:

$$A(x,y,z,T) = A_0(x,y,z,T)(1.1)^{(T(x,y,z)-T_0(x,y,z))} \tag{6.3.3}$$

where T_0 is the basal temperature and A_0 is the basal metabolic rate at cell (x,y,z). Regulatory mechanism affecting the internal tissue blood perfusion coefficient is dependent on the local tissue temperature and can be expressed as [118]:

$$\begin{aligned} B(x,y,z,T) &= B_0 \qquad (6.3.4)\\ &\quad if\ T(x,y,z) \leq 39°\text{C} \\ B(x,y,z,T) &= B_0[1 + S_B(T(x,y,z) - 39)] \qquad (6.3.5)\\ &\quad if\ 39°\text{C} < T(x,y,z) < 44°\text{C} \\ B(x,y,z,T) &= B_0(1 + 5S_B) \qquad (6.3.6)\\ &\quad if\ T(x,y,z) > 44°\text{C} \end{aligned}$$

Lastly, thermoregulation in the skin due to vasodilatation is considered by regulating the skin blood flow according to

$$B(x,y,z,T) \;=\; [B_0 + F_{sb}\overline{\Delta T_s}] \cdot 2^{\frac{(T(x,y,z)-T_0(x,y,z))}{6}} \tag{6.3.7}$$

where $\overline{\Delta T_s}$ is the average skin temperature increase and F_{sb} is the weight associated with it. The temperature of blood is assumed to be constant at 37°C and the external environment temperature is fixed at 24°C. S_B is assumed to have a value of $0.8°C^{-1}$ [118] and H_a is assumed to be 10.5 $W/(m^2 \cdot^\circ C)$ [119]. It should be noted that this value of H_a is used for both the skin-air and cornea-air interfaces in this work. The value of H_a suggested for the cornea-air interface is 20 $W/(m^2 \cdot^\circ C)$ [120]. Though it is not explicitly reported here, simulations have been performed for different values of H_a and the variation in temperature rise on the tissues due to the source of heat (implanted chip power dissipation) was observed to be negligible and hence a constant value of $H_a = 10.5$ $W/(m^2 \cdot^\circ C)$ has been used for all the simulations in this study. The thermoregulatory influence of sweating is neglected.

The thermal parameters for all the tissues in the head model have been directly obtained from either [96] or [118] and are reported in Table 6.1. Thermal parameters of the choroid are determined on the basis of its physiological functions. Since it is highly vascularized, it is modelled with the dielectric and thermal properties as well as mass density of blood. However, it should be noted that in all the thermal simulations considered, choroidal temperature is not fixed at blood temperature but is allowed to evolve in accordance with the bio-heat equation. Also, the cooling influence of the choroid on the retina is accounted for as mentioned in [96].

As outlined and implemented in [118], equations 6.3.1 and 6.3.2 were spatially and temporally discretized to realize an explicit finite difference time domain formulation of the bio-heat equation in the computational domain comprising of the 3-dimensional head-eye model. As a first step, it was necessary to determine the natural steady

state thermal distribution in the head-eye model in the absence of any external heat sources. This basal temperature distribution was then used as the starting point for all thermal simulations involving the operation of the retinal prosthesis.

In the next section, a validation of the thermal method and model is performed by comparing the simulated results with actual experimental observations in the eyes of dogs. It should be noted that human thermal parameters as mentioned above are used for this validation purpose even though they may not correspond exactly with thermal parameters for dogs.

6.4 Thermal Model Validation

Experiments have been performed [121] to investigate the thermal effects of power dissipation from implanted electronics on the vitreous cavity and retina in the eyes of dogs. The main objective of these studies were to determine the thermal conditions harmful to the retina and aid in the development of an implantable intraocular electronic retinal prosthesis.

Two different types of tests were carried out: In protocol 1, a heater probe, each time dissipating a different amount of power, was positioned at different points of the retina to observe immediate as well as chronic (4 weeks later) thermal damage inflicted. In protocol 2, a heater dissipating 500 mW of power was mechanically held in the vitreous cavity for 2 hours. These experiments were carried out on dogs due to the similarity between the eyes of dogs and those of humans. The heater utilized in the experiments was a custom made probe which measured approximately $1.4 \times 1.4 \times 1.0$ mm. The teflon insulation of the probe enclosed a 240Ω resistor to generate heat. The insulation also included a thermocouple to measure temperature increase right next to the heater. Another thermocouple was positioned in the vitreous cavity to

measure temperature increase in the fluid environment.

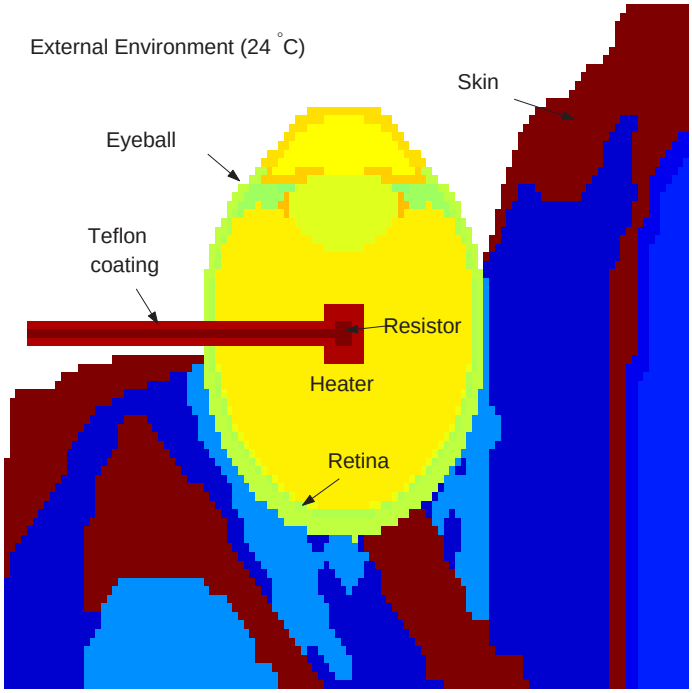

Figure 6.3: Cross section of the head model showing the implanted heater location

Due to numerical and physical constraints (inability of the head model to register damage), in this work, only protocol 2 of the experimental study mentioned above was implemented and investigated. The heater was modelled as a $1.5 \times 1.5 \times 1.0$ mm ceramic material connected to a copper wire. Since in the experimental study a teflon insulation was used around the heater resistor, in the model a 1 mm thick teflon coating insulated the wire and the heater probe from the vitreous cavity. The heater assembly was inserted from the side of the eyeball and the probe was positioned in the center of the vitreous cavity. The relative size of the head model used and placement of the heater is shown in a cross-sectional slice in Figure 6.3. As mentioned before, in the thermal simulation the choroidal temperature was not fixed at T_B but allowed to evolve naturally and the heater was allowed to dissipate 500 mW uniformly for 1

hour of simulated physical time. Temperature increase above the basal distribution at several points in the model was recorded and it was observed that thermal elevation reached a steady state within 60 minutes of physical time.

In the experimental study, five breeds of dogs were subjected to protocol 2 for 2 hours and temperature increase in the vitreous cavity and on the heater recorded at discrete intervals of time. Approximately, an average of $6-8°C$ temperature increase was observed in the vitreous cavity, $2-3°C$ on the retina and about $50-60°C$ increase was registered on the thermocouple placed on the heater. Histological samples of the eye taken (acutely as well as after 4 weeks) showed no retinal damage. It was also observed that, despite the high temperature at the heater, the temperature increase in the vitreous cavity remained within several degrees and it was concluded that the fluid environment (vitreous humor) acted as an ideal heat sink in dissipating the heat generated by the heater probe (or implanted electronics).

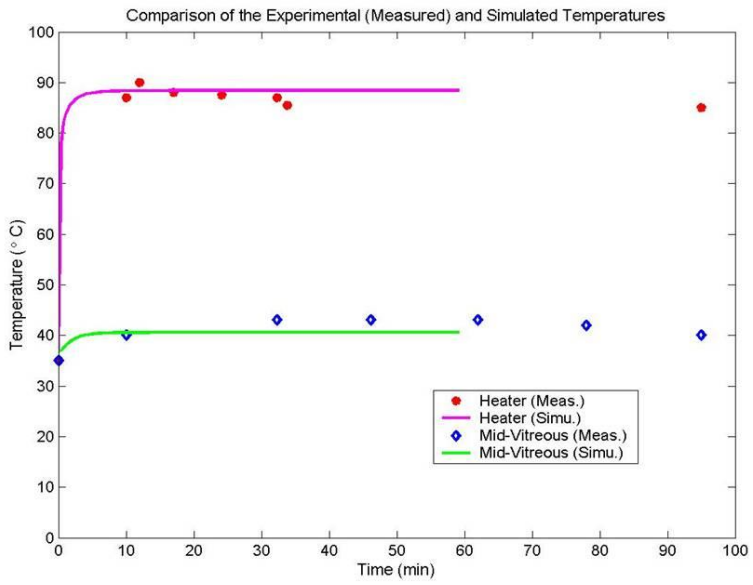

Figure 6.4: Experimentally observed vs. Numerically obtained data for thermal elevation due to implanted heater dissipating 500 mW for 2 hours.

Numerically, after 60 minutes of implementing protocol 2, the temperature in-

crease obtained in the vitreous cavity, retinal tissue and at the heater showed good agreement with the experimentally measured values. The mid-vitreous region registered a temperature increase of approximately $8-9$°C while temperature of the retinal tissue increased by $4-6$°C. Temperature at the heater also increased by 60°C. In the numerical model, increases in temperature of 0.07°C in white matter of the brain, 0.18°C in the sinuses of the forehead, 6.03°C on the cornea and 1.07°C on the skin of cheek were observed after 60 minutes of the mid-vitreous heater dissipating 500 mW.

The experimental study did not outline the precise locations of the thermocouple while recording the temperature increase at the retina and in the mid vitreous. Computationally, this led to some uncertainty in selecting specific points (in the mid-vitreous and on the retina) at which to record the temperature increase. The slight difference in experimentally measured and numerically obtained thermal elevation results is attributed to this variation in the selection of specific points in the model. Figure 6.4 shows the experimental and simulated temperature data monitored at definite intervals for a point next to the heater and in the mid-vitreous. The close agreement observed between the experimental and measured data indicates that the current model and simulation method employed are sufficiently reliable for estimating the thermal elevation in biological tissues due to power dissipated by prosthetic implants.

Since this was a validation of the thermal model and method used, it was of interest to study the cooling effect of the thermoregulatory mechanisms. Hence, two cases of numerical implementation of the bio-heat equation were considered. In the first case, the time dependency of the thermoregulatory mechanisms (B_0 and A_0 and vasodilatation) was included in the bio-heat equation while in the second case the time dependency of the thermoregulatory mechanisms was neglected. Several tissue points were monitored and it was observed that the difference in temperature rise between

the two cases was of the order of a few hundredths of a degree despite the fact that the actual temperature of that tissue rose by a few degrees in each case. Thus, in all the simulations with implanted chips, the time dependency of the thermoregulatory effects was neglected.

6.5 SAR Results

Power absorption in the head and eye tissues due to the wireless link was computed by modelling a 2 A current at 10 MHz excited in a single turn circular coil of approximately 37 mm diameter positioned 20 mm away from the cornea. Peak 1-g SAR values were evaluated and observed to be $SAR_{1g} = 0.021$ [W/kg]. The SAR profile in the head model cross section is depicted in Figure 6.5.

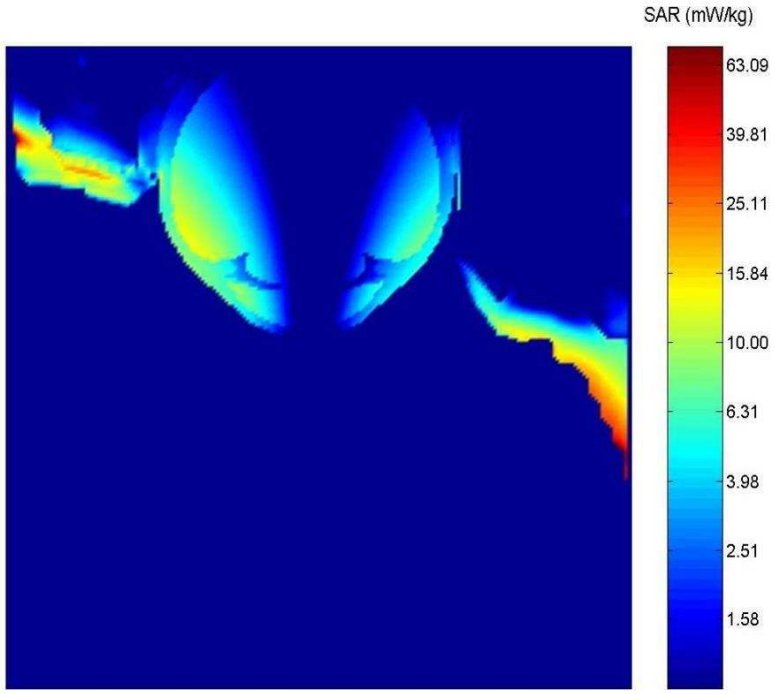

Figure 6.5: A horizontal cross section of the head model showing the deposition of electromagnetic energy (SAR profile).

Since at these currently estimated operating power and current levels the SAR values for the inductive communication link do not exceed the IEEE safety limits for power absorption [47], the contribution of SAR to the final temperature elevation would be negligible as compared to the rise in temperature due to power dissipation in the implanted chip. Therefore, the power dissipation of the implanted chip alone has been considered as an external heat source in the thermal simulations.

6.6 Thermal Elevation Results

In order to compute the thermal elevation in the head model due to implanted electronics, it was necessary to first obtain the natural basal temperature distribution in the absence of any external heat sources. The basal temperature distribution was obtained for the larger portion of the head model shown in Figure 6.2 (as noted in section 6.2) with no external heat sources and the external environment temperature being fixed at 24°C.

A portion of this model was extracted and the implant was modelled with the dimensional and material properties of an electronic chip. This implanted chip was modelled to have a composite thermal conductivity (K) of $60[\mathrm{J/m \cdot s \cdot^\circ C}]$ and encapsulated in a 0.5 mm thick layer of insulation ($K = 30[\mathrm{J/m \cdot s \cdot^\circ C}]$). Several thermal simulations were performed with the chip modelled with different sizes, placed at different locations (in the eyeball) and also dissipating different amounts of power in order to gain an insight into the best possible configuration (from the point of view of least thermal elevation) for an implant in the eye. In the following subsections, results obtained for all the different cases considered are presented.

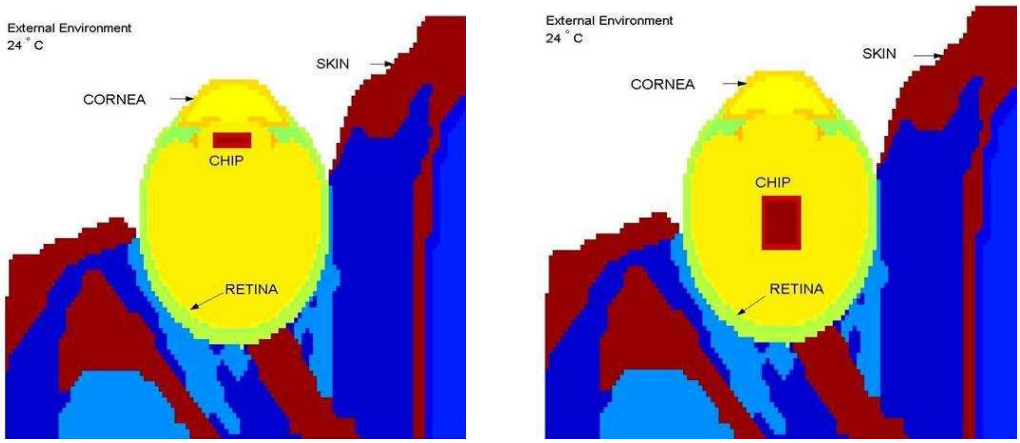

(a) (b)

Figure 6.6: Cross section of the head model depicting the location of the chip :
(a) Anterior Chip ;
(b) Center Chip.

6.6.1 Influence of LOCATION of Implant on tissue heating

Two locations are being considered for the placement of implanted electronics. In the first case, the lens is removed and the implanted chip (along with the intraocular receiving antenna of the wireless link) is hinged between the ciliary muscles of the eye (referred to as the Anterior position) as shown in Figure 6.6(a). The other position under consideration as shown in Figure 6.6(b) is in the middle of the vitreous cavity parallel to the axis of the eyeball (referred to as the Center position). The head model used is the same as the one utilized in the thermal validation case. The implanted chip is modelled at both these aforementioned locations and thermal simulations performed to study the variation in temperature increase in different tissues as a function of the implant location.

For both the above cases, the size of the implanted chip was kept constant at $4 \times 4 \times 0.5$ mm (exclusive of the 0.5 mm insulating material) and was allowed to dissipate 12.4 mW (anticipated worst case power dissipation from an implanted current stimulator

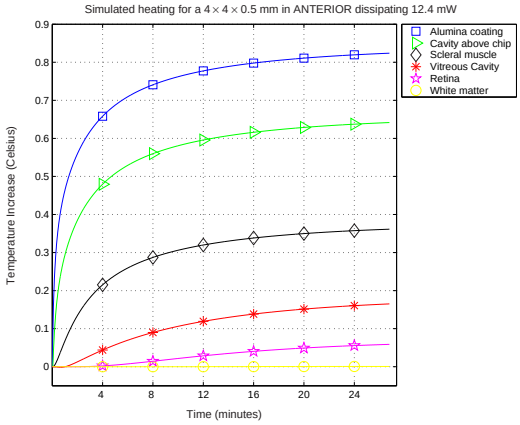

(a) Anterior positioned $4 \times 4 \times 0.5$ mm chip dissipating 12.4 mW

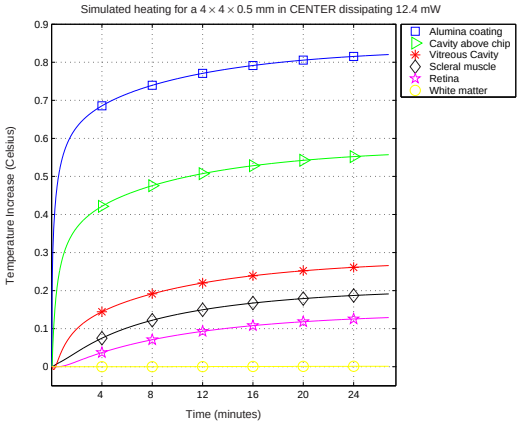

(b) Center positioned $4 \times 4 \times 0.5$ mm chip dissipating 12.4 mW

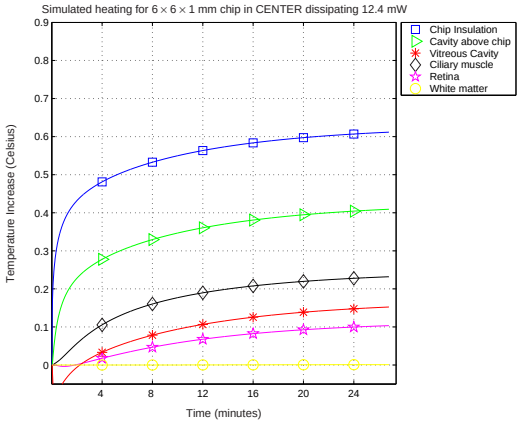

(c) Center positioned $6 \times 6 \times 1$ mm chip dissipating 12.4 mW

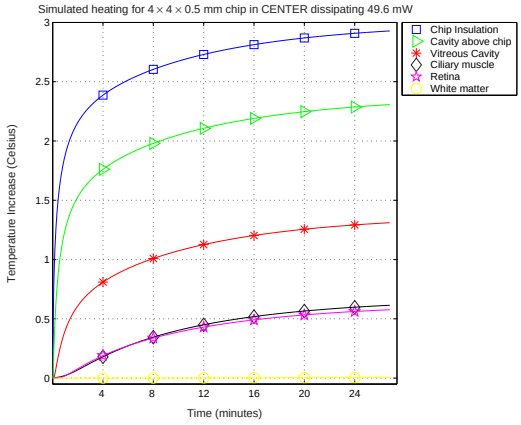

(d) Center positioned $4 \times 4 \times 0.5$ mm chip dissipating 49.6 mW

Figure 6.7: Simulated heating for different configurations.

chip driving a 16 electrode array positioned on the retina). The power density for each cell (W/m^3) was calculated from the total power dissipated (12.4 mW) and was kept uniform for each cell of the modelled chip throughout its size [96]. Figures 6.7(a) and 6.7(b) show the temperature increase observed in the different tissues with the implanted chip in anterior and center positions respectively allowed to dissipate 12.4 mW for approximately 26 minutes of simulated physical time.

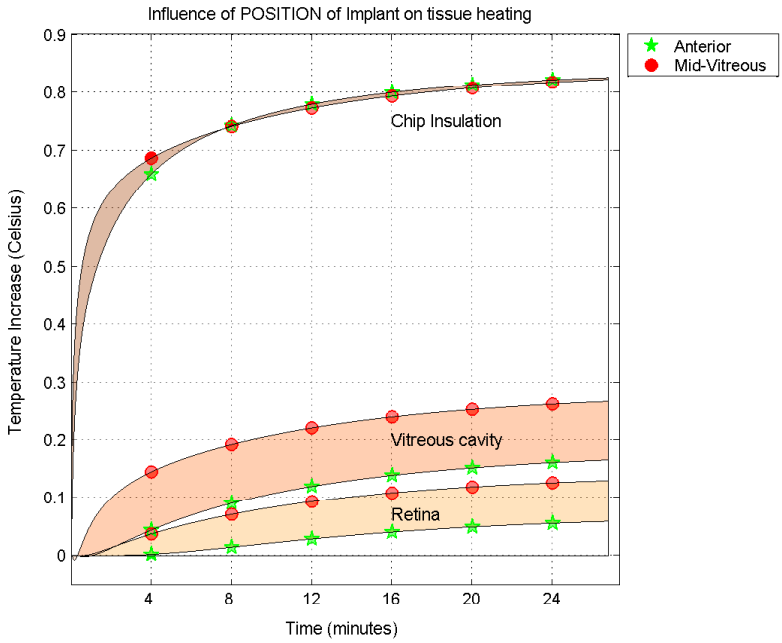

Figure 6.8: Simulated thermal rise showing the influence of chip's LOCATION

The maximum temperature increase for both the chip positions is obtained on the surface of the insulating layer. At the specific location monitored in the numerical simulation, it is observed to be about 0.82°C for both chip positions. As can be expected, due to its proximity to a chip placed in the anterior region, the ciliary muscles for this case heat up by 0.36°C as compared to 0.19°C with the chip in the center position. Temperature rise in the vitreous cavity is observed to be 0.26°C for the chip placed in center while a anterior chip raises its temperature by 0.16°C.

Even though there is no standard accepted threshold for the induction of thermal damage on the retina, it is a very sensitive membrane on which temperature rise is of interest since in an actual prosthesis it is proposed that an electrode array will rest on the retina to provide artificial stimulation. An anterior placed chip raises retina's temperature by less than half the amount that a chip placed in the center does (0.05°C by anterior chip as compared to 0.12°C by a center chip). Here, also, the vitreous cavity seems to be acting as a heat sink since the rise in temperature of tissues farther from the eye is very small indicating that a miniscule amount of heat flows beyond the eye ball.

Figure 6.8 graphically compares the temperature increases on the insulator, vitreous cavity and the retina between a anterior placed chip and a center placed chip. It is observed that the anterior position is preferable in order to minimize the temperature rises in the vitreous cavity and on the retina.

6.6.2 Influence of SIZE of Implant on tissue heating

Besides location, the physical size of the implant is another parameter which can be varied to bring about a reduction in temperature elevation for a given amount of power dissipation. Hence, it is of interest to investigate the effect of *increase* in the implanted chip's size on thermal elevation for a fixed amount of power dissipation.

Two sizes of the implanted chip are considered: $4 \times 4 \times 0.5$ mm (small) and $6 \times 6 \times 1$ mm (large). In both cases, the chips are placed in center position and allowed to dissipate 12.4 mW of power for 26 minutes of simulated physical time. Again, the power density is kept uniform for each cell throughout the size of the chip and with both chips dissipating the same power, the power density for each cell of the larger chip is much smaller than that for each cell of the smaller chip. Figures 6.7(b) and 6.7(c) show the temperature increase observed in the different tissues with the

small and large implanted chips in the center position dissipating 12.4 mW of power for 26 minutes of simulated physical time.

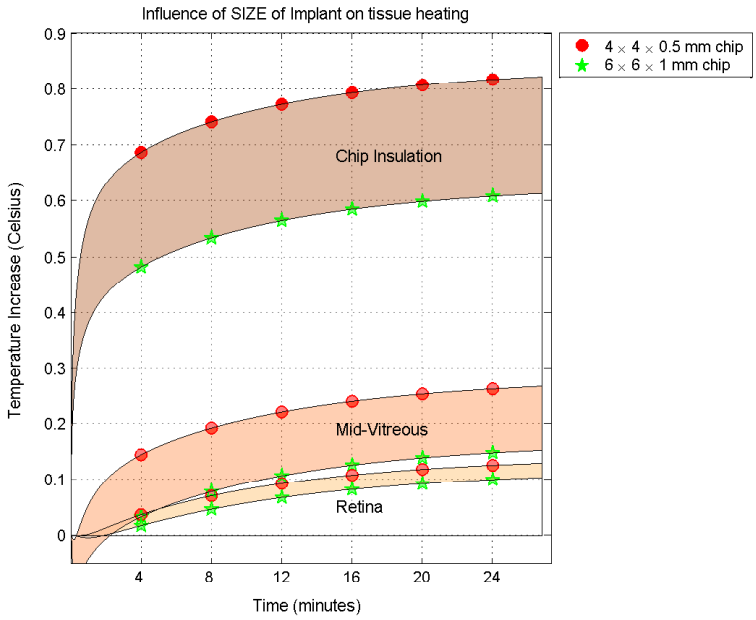

Figure 6.9: Simulated thermal rise showing the influence of chip's SIZE

Figure 6.9 graphically compares the temperature increase observed on the insulator, in the vitreous cavity and on the retina for both the cases. With the larger chip (less power density), temperature rise decreases on the insulator by 0.20°C, in the vitreous cavity by 0.11°C and on the retina by 0.02°C as compared to temperature rise due to the smaller chip.

However, it is observed that thermal elevation in tissues lying towards the anterior portion of the model (towards the external environment like cornea, ciliary muscle, skin et al.), is slightly higher due to the larger chip than the smaller chip. The reason for this slight increase may be attributed to the following factors. The larger chip extends out by a few computational cells in all the directions as compared to the smaller chip. Since blood perfusion in anterior tissues is lesser, temperature increase in

this portion is slightly more as compared to that observed for smaller chip. In tissues posterior to the chip (retina, muscle) however, higher blood perfusion facilitates more cooling and hence the power density of the chip influences the temperature increase (rather than the proximity to the chip). Thus, in the posterior tissues, temperature increase with the larger chip is less than that observed for the smaller chip. Table 6.2 reports the simulated heating observed in different tissues after 26 minutes of simulated physical time for different configurations of the implant.

6.6.3 Influence of POWER DISSIPATION of Implant on tissue heating

The maximum value of allowable power dissipation in an implant is decided by a fine tradeoff between satisfaction of its functional requirements and prevention of any thermal damage on the surrounding tissues. It is of interest to observe the influence of varying power dissipation levels on corresponding thermal elevation incurred in the head model.

In the 16-electrode array design of the retinal prosthesis chip, power dissipation in the implanted chips is not expected to rise above 12.4 mW. To investigate the influence of varying power dissipation, thermal rise is computed with the chip dissipating 12.4 mW in the first case and 49.6 mW in the second case (for the same size chip $4 \times 4 \times 0.5$ mm placed in the center position). Power density is again kept uniform throughout the chip's size. Figures 6.7(b) and 6.7(d) respectively show the temperature increase observed in the different tissues with the center placed $4 \times 4 \times 0.5$ mm chip dissipating 12.4 mW and 49.6 mW for 26 minutes of simulated physical time.

Figure 6.10 graphically compares the temperature increase observed on the insulation, in the vitreous cavity and on the retina for both the cases. From the thermal elevation results as tabulated in Table 6.2, it is observed that increasing the power

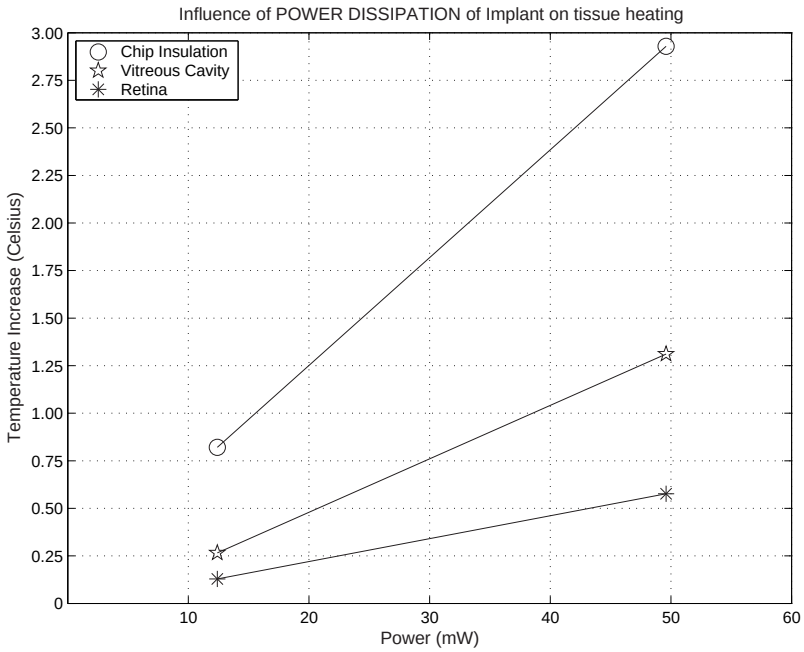

Figure 6.10: Simulated thermal rise showing the influence of chip's POWER DISSIPATION

dissipation by a factor of 4 does not necessarily lead to a rise in the temperature by the same factor. As reported in Table 6.2, on the insulator the temperature rose by a factor of 3.57 while in the vitreous cavity and on the retina the temperature increased by 4.93 and 4.47 times, respectively. In the majority of tissues, a temperature rise by a factor of around 3.5 to 5 is observed for a four times increase in the power dissipation in the implant.

Figure 6.11 depicts the thermal rise in a cross section of the head model for all the four cases considered above.

6.7 Summary

A detailed numerical investigation of the thermal elevation induced in the head and eye on account of the operation of a retinal prosthetic system has been performed.

Table 6.2: Simulated tissue heating observed due to variation in implant's size, location and power dissipation level

Tissue	**Increase above basal temperature** ($\Delta T = T - T_0$) (°C) Observed cases for different size, location and power dissipation level of Implanted chip:				Ratio $\frac{(\text{Case4})}{(\text{Case3})}$
	Case 1	**Case 2**	**Case 3**	**Case 4**	
	Center $6 \times 6 \times 1$ mm 12.4 mW	Anterior $4 \times 4 \times 0.5$ mm 12.4 mW	Center $4 \times 4 \times 0.5$ mm 12.4 mW	Center $4 \times 4 \times 0.5$ mm 49.6 mW	
Insulator around chip	0.61	0.82	0.82	2.92	3.56
Eye's ciliary muscle	0.23	0.36	0.19	0.61	3.21
Cavity just above chip	0.40	0.64	0.55	2.30	4.18
Vitreous cavity	0.15	0.16	0.26	1.31	5.03
Retina	0.10	0.05	0.12	0.57	4.75
White matter of brain	0.001	0.001	0.001	0.005	5.00
Forehead sinuses	0.003	0.003	0.003	0.013	4.33
Skin on forehead	0.002	0.002	0.002	0.010	5.00
Skin of cheek	0.029	0.042	0.026	0.097	3.73

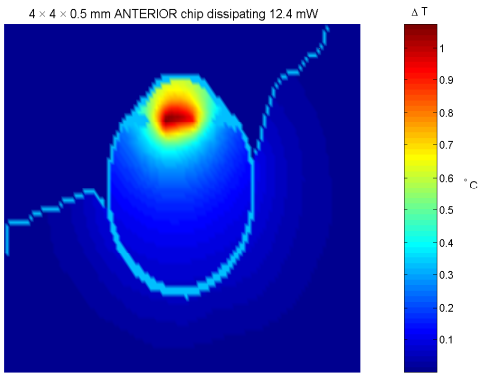

(a) Anterior positioned $4 \times 4 \times 0.5$ mm chip dissipating 12.4 mW

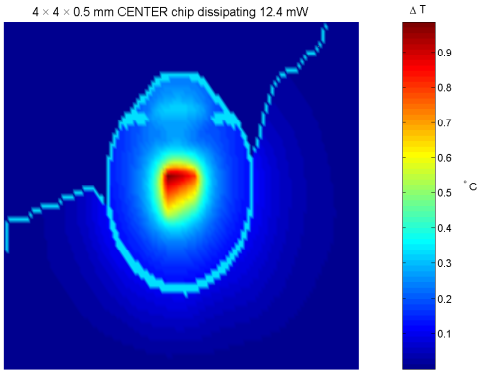

(b) Center positioned $4 \times 4 \times 0.5$ mm chip dissipating 12.4 mW

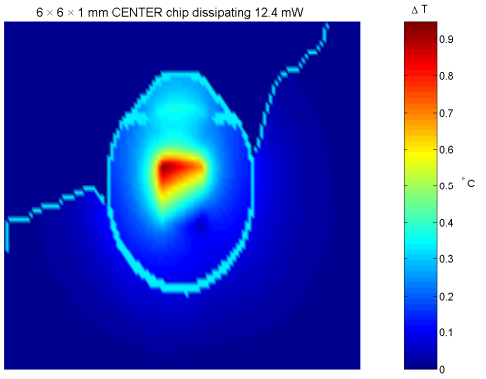

(c) Center positioned $6 \times 6 \times 1$ mm chip dissipating 12.4 mW

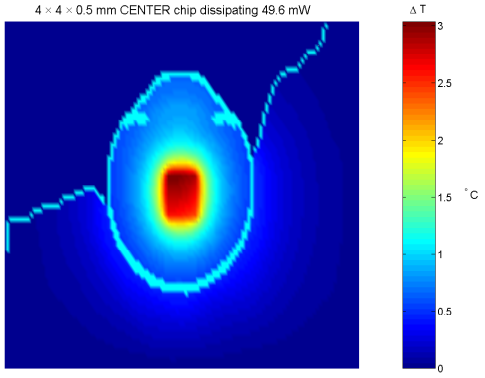

(d) Center positioned $4 \times 4 \times 0.5$ mm chip dissipating 49.6 mW

Figure 6.11: Cross section depicting the temperature rise profile for different considered heating configurations.

Operation of a retinal prosthesis (wireless telemetry link and implanted electronics) causes a rise in the natural steady state temperature of the eye and surrounding head tissues. In this work, two aspects of operation of the retinal prosthesis that lead to thermal elevation are considered : electromagnetic power deposition due to the operation of the wireless telemetry link and power dissipation in the implanted microchips.

It was noted that the SAR induced due to operation of the considered wireless telemetry link (inductive power and data transfer using coils at 10 MHz) was within the IEEE/ANSI [47] stipulated guidelines.

Several thermal simulations were performed to study the temperature elevation associated with the power dissipation in the implanted chip. When the chip is placed in the anterior position, the temperature increases on the vitreous cavity and retina were less by 0.1°C and 0.07°C respectively as compared to the case when the chip was located in the center of the vitreous cavity. Also, a larger chip ($6 \times 6 \times 1$ mm as compared to $4 \times 4 \times 0.5$ mm) dissipating the same amount of power reduced the temperature increase on the vitreous cavity and retina by 0.11°C and 0.02°C respectively. A four times rise in the power dissipation in the implant led to a corresponding temperature rise by a factor of 3.5 to 5 depending on the specific tissue.

The use of a 3-dimensional model instead of the 2-dimensional model employed in [96] facilitated the detailed characterization of the profile of the head and temperature distribution on the chip and eye. Due to excessive computation times, temperature rise on the tissues was monitored for 26 minutes of physical time, at which time the temperature rise was estimated to be within 5% of the steady state temperature increase.

Chapter 7

Conclusions and Future Work

7.1 Summary and Contributions

Research presented in this dissertation has dealt with exploring novel techniques to design physically small, electrically long (large) antennas for untapped and emerging fields in biomedical engineering and wireless applications. The salient contributions resulting from this investigation can be summarized as follows:

7.1.1 Compact Dual Polarized Antennas

An innovative and intuitive method of accomplishing compactness in a dual polarized microstrip patch antenna while retaining the isolation between the two input ports is described. Patch antennas inductively loaded with a symmetric pattern of slots are designed, implemented and characterized for variations in slot parameters. Size reduction of up to 51% is achieved and the potential for enhancing compactness even more by using such symmetrically slot loaded designs is demonstrated. Such antennas can be utilized on mobile network nodes to enhance capacity by polarization diversity.

7.1.2 Microwave Data Telemetry for Embedded Prosthetic Devices Employing Ultra Compact Implanted Antennas

A wireless microwave communication link with a prosthetic device implanted in the human body is proposed and studied. Conventional data communication with human body implanted electronics takes place via inductive coupling using coils (as in cochlear prostheses). This approach may suffer from lack of adequate bandwidth for a data intensive application such as a visual prosthesis.

Here, we have demonstrated the feasibility of high bandwidth links using antennas as external and implanted elements for wireless communication in a visual prosthesis. These wireless links were established at 1.45 GHz and 2.45 GHz using extremely compact extraocular (25×25 mm) and embedded intraocular (6×6 mm) antennas at both frequency bands. The small intraocular antennas ($kr < 0.2$, much smaller than the radiansphere at both frequency bands) were designed and implemented to operate in free space. These small antennas were modified appropriately to account for the extremely inductive influence of the lossy vitreous humor simulant fluid of the eye.

The microwave data telemetry link was characterized computationally using FDTD in the presence of an anatomically accurate 0.25 mm resolution model of the human head and eye. Moreover, it was also characterized experimentally by implanting the intraocular antenna inside an eye phantom filled with vitreous humor simulant fluid. Computational and experimental values agree well. Interestingly, it was observed that the eye ball and surrounding head tissues act as a form of dielectric lens and improve the coupling performance between the antennas (as compared to the coupling in free space).

7.1.3 Novel Intraocular Antennas

Two entirely different types of novel small antennas (6×6 mm) were designed and implemented to be used as intraocular elements in the data telemetry link : Microstrip patch antennas and Meander line dipole antennas.

Microstrip patch antennas were designed using inductive loading slots and shorting posts to achieve the requisite compactness. The designs at both the frequency bands (1.45 GHz and 2.45 GHz) was similar and facilitated minor alterations for matching the operating frequency with the extraocular antenna. Moreover, the designs facilitated modifications to change the impedance characteristics to account for the dielectric loading influence of the eye ball.

Novel impedance matching techniques were employed to implement the planar meander line dipole antennas for the retinal prosthesis. The design of the wire dipole antennas permitted matching and operating them at any desired frequency with the requisite compactness. A current phase reversal technique is described and used to impedance match these antennas which enhances and directs the radiation broadside to the antennas.

The microwave telemetry link was experimentally characterized with both types of embedded small antennas and the coupling performance with wire dipoles improved significantly as compared to embedded patch antennas. This is attributed to the highly directive broadside radiation pattern of the wire dipoles.

In this research, not only were novel small antennas designed and implemented but also their feasibility in a specific biomedical application (a visual prosthesis) was demonstrated experimentally.

7.1.4 Electromagnetic and Thermal Characterization of the Operation of a Retinal Prosthesis

Electromagnetic energy deposition in the head and eye tissues due to the operation of the wireless link for a retinal prosthesis was evaluated computationally using FDTD within an anatomically accurate head model.

Energy deposition was quantified in terms of Specific Absorption Rate (SAR) for the microwave data telemetry link (at 1.45 GHz and 2.45 GHz) and the inductive power link (at 10 MHz). SAR was computed for a maximum transmitted power of 50 mW for the data telemetry links and with a 2 A excitation of the primary single turn coil for the power link. Peak 1-g power absorbed in the human head model was evaluated and was observed to be within the IEEE stipulated guidelines of 1.6 W/kg.

The bio-heat equation was discretized and implemented in a 3-dimensional FDTD code. Power dissipation in an implanted chip was modelled to evaluate the thermal rise in the eye and head tissues due to operation of the implanted electronic circuitry. The electromagnetic power deposition was not considered as a source of heat since the SAR values were within IEEE limits. A comprehensive account of temperature elevations in different tissues under different operational conditions of the implanted chip was presented.

7.2 Ongoing Efforts and Future Research

The progress and research reported here on the small antenna design and the electromagnetic and thermal effects of a visual prosthesis is extensive but certainly not comprehensive. Several opportunities for continued work on the different aspects of antenna design and development of a retinal prosthesis exist. Below are outlined some key points of interest which can be addressed:

7.2.1 Antenna Design for Wireless Applications

The dual polarized antennas can be employed in a wireless test bed and the capacity gain due to polarization diversity characterized. Currently, such channel characterizations are being carried out with four identical such antennas and its results are awaited. Also, novel compact antenna design for capacity enhancement in Multiple Input Multiple Output (MIMO) applications is currently underway in our research group.

7.2.2 Characterizing the Data Telemetry Link

In the research reported here, the microwave data telemetry link was experimentally investigated using eye phantoms filled with vitreous humor simulant fluid. This eye phantom can be placed inside a human head model filled with a muscle simulant fluid and the data telemetry link established again.

Moreover, due to limited computational resources of time and memory, numerically the telemetry link has been characterized for a fixed separation of 25 mm. Future attempts can characterize the link at different separations computationally which will enable further comparison between the the numerical and observed experimental results.

7.2.3 Intraocular Antenna Design

Several avenues exist to enhance the intraocular small antenna design and implementation. New designs should be explored which facilitate further compactness at minor deterioration in performance. Further work on designing the antennas to operate in the ISM band (900 MHz) with the same size restrictions is required.

7.2.3.1 Patch antennas

The compactness of the microstrip patch antennas can certainly be increased by finer slot implementation. Also, means to add the shorting pin during fabrication process itself (rather than soldering later) can be investigated and applied to ease the fabrication process.

7.2.3.2 Novel wire antennas

Further work on increasing the number of spiral turns on the meander line dipole can certainly enhance its compactness. Also, a balanced feed mechanism for the dipole can be used and the telemetry link coupling characterized again and the results compared with those obtained with the unbalanced (SMA) feed.

Moreover, such planar extremely compact antenna structures with enhanced broadside directivity can serve as sensors in short range wireless connections (bluetooth, Zigbee, WiFi) besides bio-implantable devices. These devices can also be employed in RFID readers and such mechanisms which currently rely on low frequency inductive coil coupling for communication.

It would be most interesting to see if 3-dimensional wire antenna structures can be utilized for the intraocular element. A 3-dimensional structure would fill up more of the effective volume of the radian sphere and thus enhance the performance. Bandwidth can be maximized for a given radiation gain if novel 3-dimensional geometries can be designed which not only provide compactness at the lower order modes but also fill up the radian sphere volume most efficiently. However, impedance matching the radiating structure to the system impedance at the lower operating modes might present a formidable obstacle. Insights gained from designing wire antennas can be utilized in pursuing more efficient radiators (extremely compact 3-dimensional antenna structures that adhere to the theoretical Chu-Harrington performance limit–

lowest Q possible).

7.3 Further Work on Electromagnetic and Thermal Modeling

Detailed computational studies of electromagnetic power deposition for various operational conditions of the wireless link can be performed. Moreover, thermal elevation can be evaluated for several aspects of operation of the entire implanted system.

7.3.1 SAR Calculations for Various Antenna and Coil Geometries

Currently, SAR calculations have been made only with the extraocular patch antenna at both the frequency bands. This antenna can be modified or a different type of antenna can be used and SAR computations performed for the same power transmitted of 50 mW. Moreover, various combinations of transmitter and receiver antenna types can be used to completely characterize the data telemetry link.

Complicated coil geometries for the extraocular (primary) coil can be used and excited with actual anticipated currents to observe the power deposited in the head and eye tissues. Work on novel embedded coil geometries to enhance power coupling with the extraocular coil is currently under progress in our group.

7.3.2 Temperature rise for Different Chip Operational regions

It is understood that different portions of the implanted chip and circuitry will dissipate different amount of heat under actual operational conditions. Hence, the actual spatio-thermal power dissipation on the chip surface can be modelled in thermal simulations to evaluate temperature rise in tissues. Comparisons between the thermal effects due to non-uniform and uniform power dissipation on the chip surface can be performed.

7.3.3 Thermal Characterization of the Entire Implanted Prosthetic System

The implanted system consists of the implanted coil, signal processing/current stimulator chips and the electrode array to provide actual stimulation to the retinal cells. To comprehensively evaluate the thermal effects associated with the operation of the implanted unit, power dissipation in the secondary coil and electrode array should be modelled along with the chip. The secondary coil dissipates power due to I^2R losses associated with the induced current and the electrode array consists of micro-electrodes which inject the requisite amount of current in the retinal cells for stimulation.

Both these functions lead to power dissipation which will augment the thermal rise observed due to the implanted chips/signal processing circuitry. A comprehensive account of elevation due to all possible thermal sources is necessary to determine the extent of temperature rise that such an implanted prosthetic system can cause and identify performance constraints for safety purposes.

Bibliography

[1] G.S. Brindley and W. S. Lewin,"The sensations produced by electrical stimulation of the visual cortex," *J. Physiology*, 196:479–493, 1968.

[2] B. Smith, T. Zhengnian, M. W. Johnson, S. Pourmehdi, M. M. Gazdik, J. R. Buckett, and P. H. Peckham, "An externally powered, multichannel, implantable stimulator-telemeter for control of paralyzed muscle," *IEEE Tran. on Biomedical Engineering*, 45(4):463–475, April, 1998.

[3] S. Robin, M. Sawan, J. F. Harvey, M. Abdel-Gawad, T. M. Abdel-Baky, and M. M. Elhilai, "A new implantable microstimulator dedicated to selective stimulation of the bladder," *Proc. of the 19th Annual International Conference of the Engineering in Medicine and Biology Soc.,* 4:1792–1795, 1997.

[4] P. C. Loizou, "Mimicking the human ear," *IEEE Signal Processing Magazine*, 15(5):101–103, September, 1998.

[5] D. H. Liang, H. S. Lusted, and R. L. White, "The nerve-electrode interface of the cochlear implant: current spread," *IEEE Trans. on Biomedical Engineering*, 46(1):35–43, January, 1999.

[6] E. Zrenner, "Will Retinal Implants Restore Vision?", *Science Mag.*, 295:1022–1025, 8 February 2002.

[7] "Various Eye Care Statistics," *Association of Vision Science Librarians*, 1993. (http://spectacle.berkeley.edu/library/stats.htm).

[8] http://www.theretinasource.com

[9] A. Santos, M. S. Humayun, E. de Juan Jr., R. J. Greenberg, M.J. Marsh, A. H. Milam, "Inner retinal preservation in retinitis pigmentosa: a morphometric analysis," *Archives of Ophthalmology*, 115:511–515, 1997.

[10] J. L. Stone, W. E. Barlow, M. S. Humayun, E. De Juan Jr., and A. H. Milam,"Morphometric analysis of macular photoreceptor and ganglion cells in retinas with retinitis pigmentosa," *Archives of Ophthalmology*, 110:1634–1639, 1992.

[11] M. S. Humayun, E. de Juan Jr., J.D. Weiland, G. Dagnelie, S. Katona, R. J. Greenberg, S. Suzuki, "Pattern electrical stimulation of the human retina," *Vision Research*, 39:2569–2576, 1999.

[12] E. Margalit, M. Maia, J.D. Weiland, R. J. Greenberg, G. Y. Fujii, G. Torres, D. V. Piyathaisere, T. M. O'Hearn, W. Liu, G. Lazzi, G. Dagnelie, D. A. Scribner, E. de Juan Jr., M. S. Humayun, "Retinal Prosthesis for the Blind," *Survey of Ophthalmology*, 47(4):335–356, 2002.

[13] A.Y. Chow, M.T. Pardue, G. A. Peyman, N. S. Peachey, "Development and application of subretinal semiconductor microphotodiode array," in Peyman FA, Meffert SA, Conway MD, Chou F (eds): *Vitreoretinal Surgical Techniques*, London, Martin Dunitz, Ltd, 2001, pp 576.

[14] E. Zrenner, A. Stett, S. Weiss, R. B. Aramant, E. Guenther, K. Kohler, K. D. Miliczek, M. J. Seiler and H. Haemmerle, "Can Subretinal Microphoto-

diodes Successfully Replace Degenerated Photoreceptors ?," *Vision Research*, 39(15):2555–2567, July, 1999.

[15] A.Y. Chow and V. Y. Chow, "Subretinal electrical stimulation of the rabbit retina," *Neuroscience Letters*, 225:13–16, 1997.

[16] R. Eckmiller, "Learning Retina Implants with Epiretinal Contacts," *Ophthalmic Research*, 29:281–289, 1997.

[17] M. V. Narayanan, J. F. Rizzo, D. Edell and J. L. Wyatt, "Development of a Silicon Retinal Implant: Cortical Evoked Potentials following Focal Stimulation of the Rabbit Retina with Light and Electricity," *Investigative Ophthalmology and Visual Science*, 35:1380, 1994.

[18] J. Wyatt and J.F. Rizzo, "Ocular implants for the blind," *IEEE Spectrum*, pp. 47–53, 1996.

[19] T. Yagi, Y. Ito, H. Kanda, S. Tanaka, M. Watanabe, and Y. Uchikawa, "Hybrid retinal implant: fusion of engineering and neuroscience," *Proc. of the 1999 IEEE International Conference on Systems, Man, and Cybernetics*, 4:382–385, 1999.

[20] G. J. Suaning and N. H. Lovell, "A 100-channel stimulator for excitation of retinal ganglion cells," *Proc. of the 20th International Conference of the IEEE Engineering in Medicine and Biology Soc.,* October 1998.

[21] M. Clements, K. Vichienchom, W. Liu, C. Hughes, E. McGucken, C. DeMarco, J. Mueller, M. Humayun, E. De Juan Jr., J. Weiland, and R. Greenberg, "An implantable neuro-stimulator device for a retinal prosthesis," *International Solid State Circuits Conference*, 216–217, February 1999.

[22] W. Liu, M. S. Humayun, E.McGucken, E. de Juan Jr., J. D. Weiland, S. C. DeMarco and M. Clements,"Multiple Unit Artificial Retina Chipset System to Benefit the Visual Impaired," Chapter 2, in *Intelligent Systems for the Disable* (edited by N. Theodorescu), CRC Press (invited chapter), December 2000.

[23] J. Wyatt, J. Mann, D. Edell, J. Raffel, and J. F. Rizzo, "Development of a Silicon Retinal Implant: demonstration of microelectronic system for optical transmission of signal and power," *Investigative Ophthalmology and Visual Science*, 36(4):1130, April 1995 (Accompanying poster presentation online at: http://rleweb.mit.edu/retina).

[24] W. Liu, K. Vichienchom, M. Clements, S. C. DeMarco, C. Hughes, E.McGucken, M. S. Humayun, E. de Juan Jr., J. D. Weiland, R. J. Greenberg, "A Neuro-Stimulus Chip with Telemetry Unit for Retinal Prosthetic Device," *IEEE Journal of Solid-State Circuits*, 35(10):1487–1497, October 2000.

[25] C. Veraart, C. Raftopoulos, J. T. Mortimer, J. Delbeke, D. Pins, G. Michaux, A. Vanlierde, S. Parrini, and M. C. Wanet-Defalque, "Visual Sensations produced by optic nerve stimulation using an implanted self-sizing spiral cuff electrode," *Brain Research*, 813(1):181–186, 1998.

[26] C. Veraart, J. Delbeke, M. C. Wanet-Defalque, A. Vanlierde, J. D. Legat, and C. Trullemans, "Chronic electrical stimulation of the optic nerve in a retinitis pigmentosa blind volunteer," *Investigative Ophthalmology and Visual Science*, 40:S783, 1999.

[27] R. A. Normann, E. M. Maynard, P. J. Rousche, D. J. Warren,"A neural interface for a cortical vision prosthesis," *Vision Research*, pp. 2577–2587, 1999.

[28] P. K. Campbell, K. E. Jones, R. J. Huber, K. W. Horch, and R. A. Normann,

"A silicon based three dimensional neural interface: manufacturing processes for an intracortical electrode array," *IEEE Trans. on Biomedical Engineering*, 38:758–768, 1991.

[29] A. B. Majji, M. S. Humayun, J. D. Weiland, S. Suzuki, S. A. D'Anna, and E. De Juan Jr., "Long term histological and electrophysiological results of an inactive epi-retinal electrode array implantation in dogs," *Investigative Ophthalmology and Visual Science*, 40(9):2073–2081, August, 1999.

[30] L. Rucker and A. Lossinsky, "Percutaneous Connectors" *30th Neural Prosthesis Workshop, NINDS, NINCD, NIH*, October, 1999.

[31] M. Gross, R. Buss, K. Kohler, J. Schaub, and D. Jager, "Optical signal and energy transmission for a retina implant," *Proceedings of the First Joint BMES/EMBS Conference*, 1:476, 1999.

[32] K. Inoue, K. Shiba, E. Shu, K. Koshiji, K. Tsukahara, T. Ohu-mi, T. Masuzawa, E. Tatsumi, Y. Taenaka, and H. Takano, "Transcutaneous optical telemetry system-investigation on deviation characteristics," *Proceedings of the 19th International Conference of Engineering in Medicine and Biology Society*, 5:2235–2237, 1997.

[33] J. Schuder, H. Stephenson, and J. Townsend, "High-level electromagnetic energy transfer through a closed chest wall," *IRE International Convention Record*, 9:119–126, 1961.

[34] M. Ghovanloo, K. Beach, K.D.Wise and K. Najafi, "A BiCMOS wireless interface chip for micromachined stimulating microprobes," *IEEE-EMB Sp. Topic Conf. Microtechnologies in Med. and Biology*, 277–282, 2002.

[35] J. A. Von Arx and K. Najafi, "A wireless single-chip telemetry-powrered neural stimulation system," *IEEE Conf. on Solid-State circuits*, 214–215, 1999.

[36] T. Akin, K. Najafi and R. M. Bradley, "A wireless implantable multichannel digital neural recording system for a micromachined sieve electrode," *IEEE Journal of Solid State Circuits*, 33(1):109–118, January, 1998.

[37] J. A. Von Arx and K. Najafi, "On-chip coils with integrated cores for remote inductive powering of integrated microsystems," *IEEE Conf. on Solid State Sensors and Actuators*, 2:999–1002, 1997.

[38] N. Donaldson and T.A. Perkins, "Analysis of resonant coupled coils in the design of radio frequency transcutaneous links," *Medical and Biological Engineering and Computing*, 21:612–627, 1983.

[39] W.H. Ko, S.P. Liang, and C.D.F. Fung, "Design of radio-frequency powered coils for implant instruments," *Medical and Biological Engineering and Computing*, 15:634–640, 1977.

[40] F.C. Flack, E.D. James, and D.M. Schlapp, "Mutual inductance of air-cored coils: effect on design of radio-frequency coupled implants," *Medical and Biological Engineering and Computing*, 9:79–85, 1971.

[41] C. M. Zierhofer and E. S. Hochmair, "High efficiency coupling insensitive transcutaneous power and data transmission via an inductive link," *IEEE Tran. on Biomedical Engineering*, 37(7):716–722, July, 1990.

[42] C. M. Zierhofer and E. S. Hochmair, "Geometric approach for coupling enhancement of magnetically coupled coils," *IEEE Tran. on Biomedical Engineering*, 43(7):716–722, July, 1996.

[43] S. C. DeMarco, *The architecture, design and electromagnetic and thermal modeling of a retinal prosthesis to benefit the visually impaired.* Ph.D Dissertation, North Carolina State University, 2003.

[44] D. Marin, M. Troosters, I. Martinez, E. Valderrama, J. Aguilo, "New developments for high performance implantable stimulators: First 3 Mbps upto 4.46 Mbps demodulator chip through a wireless transcutaneous link," *Int. Conf. on Microelectronics for Neural, Fuzzy and Bio-inspired systems*, 120–126, 1999.

[45] M. Ghovanloo and K. Najafi, "A high-rate frequency shift keying demodulator chip for wireless biomedical implants," *Proc. of the 2003 International Symposium on Circuits and Systems*, 5:25–28, May 2003.

[46] K. Gosalia, P. Brown, W. Liu and G. Lazzi, "FDTD Investigation of a Microwave link for Data Telemetry in Retinal Prosthesis Applications," *Int. Symp. on Antennas and Propagation,* 1:807–810, 2002.

[47] *IEEE Standard for Safety Levels with Respect to Human Exposure to radio Frequency Electromagnetic Fields, 3 kHz to 300 GHz*, IEEE Standard C95.1-1999.

[48] R. F. Harrington, *Field Computation by Moment Method*, New York, Macmillan, 1968.

[49] R. Courant, "Variational methods for the solution of problems of equilibrium and vibrations," *Bull. Am. Math. Soc.*, 49:1–23, 1943.

[50] K. S. Yee, "Numerical solution of initial boundary value problems involving Maxwell's equations," *IEEE Transactions on Antennas and Propagation*, 14:302–307, 1966.

[51] R. Garg, P. Bhartia, I. Bahl and A. Ittipiboon, *Microstrip antenna design handbook*, Artech House, 2001.

[52] D. Sullivan. *Electromagnetic Simulation Using the FDTD Method*. IEEE Press, New York, NY, 2000.

[53] A. Taflove and S. Hagness, *Computational electrodynamics: The Finite Difference Time Domain method*, Artech House, 2000.

[54] J. P. Berenger, "A perfectly matched layer for the absorption of the electromagnetic waves," *Journal of Computational Physics*, 114:185–200, 1994.

[55] Constantine A. Balanis. *Antenna Theory : Analysis and Design*. John Wiley and Sons, Inc., 2nd Edition, 1997.

[56] John D. Kraus and Ronald J. Marhefka. *Antennas For All Applications*. McGraw Hill, 3rd Edition, NY, 2002.

[57] R. E. Collin. *Antennas And Radiowave Propagation*. McGraw Hill, 1985.

[58] R.S.Elliott. *Antenna theory and design*. Prentice Hall, c1981.

[59] J. Q. Howell, "Microstrip antennas," *IEEE Transactions on Antennas and Propagation,* 23(1):90–93, January 1975.

[60] Y.T.Lo, D. Solomon and D. Richards, "Theory and Experiment on Microstrip antennas," *IEEE Transactions on Antennas and Propagation,* 27(2):137–145, March 1979.

[61] K. R. Carver, J. W. Mink, "Microstrip Antenna Technology," *IEEE Transactions on Antennas and Propagation,* 29(1):2–24, January 1981.

[62] W.F. Richards and Y. T. Lo, "An improved theory for Microstrip antennas and applications," *Dig. Int. Symp. Antennas and Propagation Soc.,* Seattle, WA pp:113–116, June 1979.

[63] A. G. Derneryd, "A theoretical investigation of the rectangular Microstrip antenna element," *IEEE Transactions on Antennas and Propagation,* 26(4):532–535, July 1978.

[64] A. G. Derneryd, "Extended Analysis of Rectangular Microstrip Resonator Antennas," *IEEE Transactions on Antennas and Propagation,* 27(6):846–849, November 1979.

[65] P. K. Agarwal and M. C. Bailey, "An analysis technique for Microstrip antennas," *IEEE Transactions on Antennas and Propagation,* 25(6):756–759, November 1977.

[66] L. J. Chu, "Physical limiatations on omni-directional antennas," *Journal of Applied Physics*, 19:1163–1175, Dec., 1948.

[67] R. F. Harrington, "Effect of antenna size on gain, bandwidth, and efficiency," *J. res. NBS*, vol. 64D, pp.1–12, January, 1960.

[68] H. A. Wheeler, "Fundamental limitations of small antennas," *Proc. of IRE*, 35:1479–1488, 1947.

[69] C. Puente, J. Romeu, A. Cardama, "The koch monopole: A small fractal antenna," *IEEE Tran. on Antennas and Propagation*, 48(11):1773–1781, November, 2000.

[70] S. R. Best, "On the performance properties of the Koch fractal and other

bent wire monopoles," *IEEE Transactions on Antennas and Propagation*, 51(6):1292–1300, June 2003.

[71] S. Maci and G. B. Gentili, "Dual Frequency Patch Antennas," *IEEE Antennas and Propagation Magazine,* 39(6):13–20, December 1997.

[72] S. C. Gao, L. W. Li, T. S. Yeo and M. S. Leong, "FDTD Analysis of a Slot-Loaded Meandered Rectangular Patch Antenna for Dual Frequency Operation," *IEE Proc. of Microwaves, Ant. and Prop.,* 148(1):65–71, February 2001.

[73] K. L. Wong, *Compact and Broadband Microstrip Antennas*, John Wiley and Sons, 2002.

[74] J. T. Rowley and R. B. Waterhouse, "Performance of Shorted Microstrip Patch Antennas for Mobile Communication Handsets at 1800 MHz," *IEEE Transactions on Antennas and Propagation,* 47(5):815–822, May, 1999.

[75] R. B. Waterhouse, "Broadband Stacked Shorted Patch," *Electronic Letters,* 35(2):98–100, January, 1999.

[76] R. B. Waterhouse, S. D. Targonski and D. M. Kokotoff, "Design and Performance of Small Printed Antennas," *IEEE Transactions on Antennas and Propagation,* 46(11):1629–1633, November, 1998.

[77] K. H. Kan and R. B. Waterhouse, "A Small Printed Antenna for Wireless Communication Handset Terminals," *IEEE Transactions on Antennas and Propagation,* 47(5):815–822, May, 1999.

[78] R. B. Waterhouse and N. V. Shuley, "Frequency Agile Microstrip Rectangular Patches using Varactor diodes," *Int. Symp. on Ant. and Propagation,* Vol. 4, 1992.

[79] D. H. Schaubert, F. G. Farrar, A. Sindoris and S. T. Hayes, "Microstrip Antennas with Frequency Agility and Polarization Diversity," *IEEE Transactions on Antennas and Propagation,* 29(1):118–123, Janruary 1981.

[80] R. B. Waterhouse and N. V. Shuley, "Full Characterisation of Varactor Loaded, Probe-fed, Rectangular, Microstrip Patch Antennas," *IEE Proc. of Microwaves, Antennas and Propagation,* 141(5):367–373, October, 1994.

[81] N. Serinken, M. Jorgenson, K. W. Moreland, S. Chow, T. Willink, "Polarization diversity in high frequency radio data systems," *Electron. Lett.,* 32(19):1824–1826, Sept. 1996.

[82] K. Hettak, G. Delisle, M. Boulmalf, "A Novel Integrated Antenna for Millimeter-Wave Personal Communications Systems," *IEEE Trans. Antennas and Propagation,* 46(11):1757–1758, 1998.

[83] G. J. Foschini and M. J. Gans, "On limits of wireless communications in a fading environment when using multiple antennas," *Wireless Personal Communications,* 6(3):311–335, March 1998.

[84] A. Adrian, D. H. Schaubert, "Dual aperture-coupled microstrip antenna for dual or circular polarization," *Electron. Lett.,* 23(23):1226–1228, Nov. 1987.

[85] M. Edimo, A. Sharaiha, C. Terret, "Optimised feeding of dual polarized broadband aperture-coupled printed antenna," *Electron. Lett.,* 28(19):1785–1787, Sept. 1992.

[86] M. Yamazaki, E. T. Rahardjo, M. Haneishi, "Construction of a slot coupled planar antenna for dual polarization," *Electron. Lett.,* 30(22):1814–1815, 1994.

[87] W. S. T. Rowe, R. B. Waterhouse, "Dual polarized broadband CPW fed patch antennas," *Microwave Conference,* Asia-Pacific, pp.1423-1426, 2000.

[88] G. S. Row, S. H. Yeh, and K. L. Wong, "Compact dual-polarized microstrip antennas," *Microwave Optical Technology Letters,* 27:284–287, November 2000.

[89] T. W. Chiou and K. L. Wong, "Designs of compact microstrip antennas with a slotted ground plane," *IEEE Antennas and Propagation International Symposium digest,* pp. 732–735, 2001.

[90] G. Lazzi, O. P. Gandhi and D. Sullivan, "Use of PML absorbing layers for the truncation of the head model in cellular telephone simulations," *IEEE Transactionson Microwave Theory and Techniques*, 48(11):2033–2039, November 2000.

[91] A. C. Ludwig, "The Definition of Cross Polarization," *IEEE Trans. on Antennas and Propagation.,* Vol. AP-21, Jan. 1973, pp.116-119.

[92] W. L. Stutzman. *Polarization in Electromagnetic Systems.* Artech House, MA, 1993.

[93] R. E. Marc and B. W. Jones, "Retinal Remodeling in Inherited Photoreceptor Degenerations," *Molecular Neurobiology*, 28(2):139–148, October, 2003.

[94] K. Gosalia, W. Liu, J. Weiland, M. S. Humayun and G. Lazzi, "An Investigation of the Coupling between Extremely Compact Microstrip Patch Antennas in a Link for Biomedical Implants," *Int. Symp. on Antennas and Propagation,* URSI, 2003.

[95] The National Library of Medicine. The Visible Human Project. http://www.nlm.nih.gov/research/visible/visible_human.html, 2000.

[96] S. C. DeMarco, G. Lazzi, W. Liu, J. D. Weiland and M. S. Humayun, "Computed SAR and Thermal Elevation in a 0.25mm 2–D Model of the Humal Eye and Head in response to an Implanted Retinal Stimulator: Parts I and II,". *IEEE Transactions on Antennas and Propagation*, 51(9):2274–2295, September 2003.

[97] Dielectric Properties of Body Tissue:http://safeemf.iroe.fi.cnr.it/tissprop/.

[98] Y. Wei and S. Sridhar, "Technique for measuring the frequency dependent complex dielectric constants of liquids up to 20 GHz," *Rev. Sci. Instrum.*, 60(9):3041–3046, September, 1999.

[99] I.J.Bahl, P. Bhartia and S. S. Stuchly, "Design of Microstrip Antennas Covered with a Dielectric Layer," *IEEE Trans. Antennas and Propagation*, 30(2):314–318, March, 1982.

[100] B. B. Mandelbrot, *The Fractal Geometry of Nature*, New York, W. H. Freeman and Company, 1977.

[101] J. P. Gianvittorio and Y. Rahmat-Samii, "Fractal Antennas : A novel antenna miniaturization technique and applications," *IEEE Antennas and Propagation Magazine,* 44(1):20–36, February, 2002.

[102] D. H. Werner and R. Mittra, *Frontiers in Electromagnetics*, New York, IEEE Press, 2000.

[103] C. Puente, R. Pous, J. Romeu, and X. Garcia, "Antenas fractales o multifractales," Spanish Patent no. 2112163, May 19, 1995.

[104] C. Puente, J. Romeu, R. Pous, J. Ramis, and A. Hijazo, "Small but long Koch fractal monopole," *IEE Electronics Letters*, 34:9–10, January, 1998.

[105] J. P. Gianvittorio, "Fractal Antennas : Design, Characterization and Applications," Master's thesis, University of California, Los Angeles, 2000.

[106] www.nittany-scientific.com/nwp/
NEC Win Pro available from Nittany-Scientific.

[107] J. Zhu, A. Hoorfar, and N. Engheta, "Bandwidth, Cross-Polarization and feedpoint characteristics of matched Hilbert antennas," *IEEE Antennas and Wireless Propagation Letters*, 2:2–5, 2003.

[108] S. R. Best and J. D. Morrow, "The effectiveness of space-filling fractal geometries in lowering resonant frequency," *IEEE Antennas and Wireless Propagation Letters*, 1:112–115, 2002.

[109] S. R. Best and J. D. Morrow, "On the significance of current vector alignment in establishing the resonant frequency of small space-filling wire antennas," *IEEE Antennas and Wireless Propagation Letters*, 2:201–204, 2003.

[110] W. L. Stutzman and G. A. Thiele, *Antenna Theory and Design*, John Wiley and Sons, Inc., 2nd Ed., 1998.

[111] E.R. Adair and R. C. Petersen, "Biological effects of radiofrequency/microwave radiation," *IEEE Transactions of Microwave Theory and Techniques*, 50(3):953–962, March 2002.

[112] J. Wang and O. Fujiwara, "FDTD computation of temperature rise in the human head for portable telephones," *IEEE Transactions on Microwave Theory and Techniques*, 47(8):1528–1534, August, 1999.

[113] P. Bernardi, M. Cavagnaro, S. Pisa and E. Piuzzi, "Specific absorption rate and

temperature increases in the head of a cellular-phone user," *IEEE Transactions on Microwave Theory and Techniques*, 48(7):1118–1126, July, 2000.

[114] P. Bernardi, M. Cavagnaro, S. Pisa and E. Piuzzi, "SAR distribution and temperature increases in an anatomical model of the human eye exposed to the field radiated by the user antenna in a wireless LAN," *IEEE Transactions on Microwave Theory and Techniques*, 46(12):2074–2082, December, 1998.

[115] A. Taflove and M. E. Brodwin, "Computation of the electromagnetic fields and induced temperatures within a model of the microwave-irradiated human eye," *IEEE Transactions on Microwave Theory and Techniques*, 23(11):888–896, November, 1975.

[116] A. Hirata, S. I. Matsuyama and T. Shiozawa, "Temperature rises in the human eye exposed to EM waves in the frequency range 0.6–6 GHz," *IEEE Transactions on Electromagnetic compatibility*, 42(4):386–393, November, 2000.

[117] A. Hirata, U. Ushio and T. Shiozawa, "Formation of hot spots in the human eye for plane wave exposures," *Asia Pacific Microwave Conference,* 2:477–480, 1999.

[118] P. Bernardi, M. Cavagnaro, S. Pisa and E. Piuzzi, "Specific absorption rate and temperature elevation in a subject exposed in the far-field of radio-frequency sources operating in the 10–900 MHz range," *IEEE Transactions on Biomedical Engineering*, 50(3):295–304, March 2003.

[119] H. N. Kritikos, K. R. Foster and H. P. Schwan, "Temperature profiles in spheres due to electromagnetic heating," *Journal of Microwave Power*, nos. 3/4, 16:327–344, 1981.

[120] J. J. W. Lagendijk, "A mathematical model to calculate temperature distributions in human and rabbit eyes during hyperthermic treatment," *Physics, Medicine and Biology*, 27(11):1301–1311, 1982.

[121] D. V. Piyathaisere, E. Margalit, S. J. Chen, J. S. Shyu, S. A. D'Anna, J. D. Weiland, R. R. Grebe, L. Grebe, G. Fujii, S. Y. Kim, R. J. Greenberg, E. de Juan Jr., M. S. Humayun, "Heat effects on the retina," *Ophthalmic Surgery and Lasers Imaging*, 34(2):114-120, March-April, 2003.